DEVELOPMENT OF DESIGN CRITERIA, COST ESTIMATES, AND SCHEDULES FOR AN MHD HIGH PERFORMANCE DEMONSTRATION EXPERIMENT

G. W. Garrison, T. R. Brogan, J. J. Nolan, et al.

ARO, Inc.

August 1973

PROPULSION WIND TUNNEL FACILITY

ARNOLD ENGINEERING DEVELOPMENT CENTER

AIR FORCE SYSTEMS COMMAND

ARNOLD AIR FORCE STATION, TENNESSEE

NOTICES

DEVELOPMENT OF DESIGN CRITERIA, COST ESTIMATES, AND SCHEDULES FOR AN MHD HIGH PERFORMANCE DEMONSTRATION EXPERIMENT

G. W. Garrison, T. R. Brogan, J. J. Nolan, et al.

ARO, Inc.

ı

FOREWORD

This technical report has been reviewed and is approved.

ELTON R. THOMPSON
Research and Development
   Division
Directorate of Technology

ROBERT O. DIETZ
Director of Technology

ABSTRACT

The successful application of magnetohydrodynamics (MHD) for commercial, coal-fired, base-load power generation requires that the generator have an energy extraction ratio of approximately 0.20 with a turbine efficiency of 70 percent. There is a significant gap between this required performance and the generator performance which has been achieved to date. The commercial MHD concept is critically dependent upon the generator achieving this required performance, and it is therefore essential that a demonstration of this generator performance have the highest priority. Of equal importance, the generator channel configuration and operating conditions which are necessary in order to achieve the required performance will be determined while accomplishing the performance demonstration. Thus other Office of Coal Research (OCR)-sponsored MHD research efforts can be directed toward the real problems and configurations as determined by solid experiments. Several possible options for carrying out an experiment meeting the objectives of the performance demonstration recommended by OCR Report No. 71 were considered. It is concluded that a definitive and favorable demonstration is feasible using the existing LORHO MHD facility at AEDC with a modified magnet and a new high performance generator channel. The experiment will not only demonstrate performance but also will be of a size which will allow scaling of the experimental results to the full-scale generator with reasonable confidence.

CONTENTS

APPENDIXES

I. ILLUSTRATIONS AND TABLES

Figure

NOMENCLATURE

A — Channel area, m^2

AR — Aspect ratio, ratio of channel dimension in y-direction (E-field plane) to dimension in z-direction (B-field plane)

a — Constant defined in Eq. (15)

B — Magnetic induction, tesla (T)

b — Constant defined in Eq. (15)

b_1, b_2 — Defined in Fig. 38

c — Constant in Eq. (26) defined in Table V

c_p — Specific heat capacity of coil material, joules/kg

D — Channel diameter, m

E — Electric field, v/m

e — Electron charge, 1.6×10^{-19} coulombs

H — Enthalpy, joules/kg

h_3, h_c — Defined in Fig. 38

h_g — Height of magnet bore, Fig. 38

I — Total current, amp

J — Average current density, amp/m^2

j — Local current density, amp/m^2

K — Load coefficient = E/uB

k — Boltzmann's constant = 1.38×10^{-23} joules/°K

L — Coil inductance, henries or volts sec/amp or channel length, m

ℓ_p — Half of the length of magnet pole piece in Fig. 38

M	Mach number
$\dot{m}$	Mass flow rate, kg/sec
N	Number of turns of the magnet coil
N_2	Nitrogen
O_2	Oxygen
P	Electrical power output, w
P_{elec}	Local power dissipation at the electrodes, w
$\overline{P}_{elec}$	Average power dissipation at the electrodes, w
p	Pressure, atm = 1.01325×10^5 nt/m^2
R	Coil resistance, ohms, or gas constant, joules/kg°K
R_c	Resistance of external bus, ohms
Re	Reynolds number
R_{ext}	Total circuit resistance in Eq. (33)
S	Magnetic interaction parameter
T	Temperature, °K
u	Gas velocity, m/sec
V	Power supply voltage, Eq. (29), v
V_c	Coil volume, m^3
V_e	Electrode voltage drop, v
V_i	Ionization potential, ev
V_{oc}	Power supply open circuit voltage, v
w_p	Width of magnet pole in Fig. 38
x,y,z	Orthogonal coordinates

γ	Isentropic exponent
Δ	Represents a difference or change
δ^*	Boundary-layer displacement thickness, m
θ	Wall slant angle
λ	Magnet space factor (ratio of conductor volume to the total volume)
μ	Dynamic viscosity, nt sec/m^2
μ_o .	Permeability = $4\pi \times 10^{-7}$ webers/amp-m
ρ	Gas density, kg/m^3
ρ_c	Conductor density, kg/m^3
σ	Electrical conductivity, mho/m
ϕ	Tangent of the wall slant angle or equipotential surface
Ω	Hall parameter
ω_i	Wave growth rate, 1/sec

SUBSCRIPTS

e	Refers to experiment
f	Refers to full scale
s	Value at the iron saturation point
x	Refers to channel axial dimension
y	Refers to channel dimension in electric field plane
z	Refers to channel dimension in magnetic field plane

SECTION I
INTRODUCTION

Cycle analyses of MHD coal-fired base-load electrical power plants have indicated that such plants can become economic realities only if performance of the MHD generator itself can be increased substantially beyond the levels so far attained in practice. Existing MHD generators, which have not been designed for high efficiency, have attained energy extraction ratios of only 0.05 to 0.07 at turbine efficiencies no greater than 46 percent. As part of a base-load plant, the MHD generator must attain an energy extraction ratio of at least 0.20 with a turbine efficiency of 70 percent. This large gap in performance is especially significant since the existing generators have all been operated with working fluids of much higher conductivity than would be used in a commercial plant. Generator design studies have suggested that the required performance is possible, mainly by use of a subsonic channel flow and an increased magnetic interaction. However, an actual demonstration of the performance goals in a large-scale channel designed for high performance appears to be essential, since the credibility of the commercial MHD concept is so critically dependent on the performance of the generator channel.

A performance demonstration experiment also is an ideal complement to the ongoing coal-burning MHD research program currently sponsored by the OCR:

Basic Materials Studies

Coal Combustion System Development

Electrical Properties of Coal Combustion Products

Chemical Regeneration

Preheater Development

System Analyses

Extended-Duration MHD Channel Operation

Analytical Techniques for MHD Flow

Basic MHD Flow Studies at High B-Fields

These efforts are all obviously necessary for development of MHD for commercial power plants, but a specific program to verify that an MHD generator can achieve the required performance has not yet been activated. Such a program would demonstrate that the required performance can be achieved and, of equal importance, would determine the generator configuration and operating conditions necessary to achieve the performance so that the research programs noted above can be directed toward problems which are firmly related to real experimental conditions.

Under OCR Contract No. 14-32-0001-1228, the AEDC has performed a study of the possible use of the existing LORHO Facility at AEDC to carry out such a performance demonstration. Important portions of this study were made in conjunction with two

subcontractors, the Magnetic Engineering Associates, Inc. (MEA) and MEPPSCO, Inc. The results which are described in this report are convincing in their conclusion that a definitive and favorable demonstration is feasible using the LORHO Facility equipped with a modified magnet and a new MHD generator channel. By designing the demonstration experiment mainly as an investigation of the magnetogasdynamic performance of the generator channel, as opposed to endurance capability, a pulsed mode of operation on a clean fuel is permissible. This, plus the use of existing LORHO equipment valued at $4,586,000, will allow the experiment to be performed on a reasonably large scale with a minimal expenditure of new funds. This experiment would meet the objectives recommended in OCR Report No. 71 (Ref. 1) by demonstrating that it is possible for an MHD power generator to operate with a turbine efficiency of at least 60 percent and convert 20 percent of the available thermal energy into electrical power. This performance demonstration would appear to be a logical preliminary to the investment of much larger sums for large long-duration generators (see Section 7.3).

SECTION II
LORHO FACILITY

The LORHO Facility (Fig. 1, Appendix I), was built under the FY 64 Military Construction Program as a pilot tunnel in the development of a large-scale, low-density hypersonic wind tunnel. This pilot facility, which was designed by AVCO, Inc., was an MHD generator/accelerator combination. The accelerator was never operated because of changing Air Force program requirements; however, the generator was evaluated in a lengthy test program in which an output power of 18 MW was attained.

The facility is housed in a 90-ft by 120-ft building and consists primarily of a 20-MW MHD generator and its associated electrical, mechanical, and instrumentation auxiliaries. Arrangement of components of the facility within the building is shown on Fig. 2. A major portion of the equipment presently installed in the LORHO building is required for the high performance demonstration experiment and obviously represents a substantial savings in the cost of performing such an experiment. A breakdown of the current value of the equipment directly applicable to the demonstration experiment is given in Table I (Appendix I). An estimate of the value represented by availability of 30 MW of demand power is included. As will be seen subsequently, the sum of $4,586,000 is greater than the estimated cost for the remainder of the experiment; thus, more than 50 percent of the total cost of the experiment could be saved by use of existing facilities.

The most expensive single item in Table I is the LORHO building, designed to handle the special problems which might arise in operating large MHD devices. For example, the LORHO magnet weights 1,000,000 lb and this requires a specially reinforced foundation isolated from the building structure. Care was taken in the building design to keep magnetic construction materials out of the magnet fringe fields. The high temperature generator exhaust gases are expelled through a 10-ft-diam horizontal breech, Figs. 1 and 2, equipped with water spray nozzles and electrically isolated from ground and from the vertical exhaust stack. Since the generator exit and diffuser are at 10,000 v, particular attention must

be given to insulation on the downstream section of the device. The horizontal breech, exhaust spray system, and exhaust stack will be used for the performance demonstration experiment.

The hot gas source for the generator, Fig. 3, is a water-cooled, rocket-type combustion chamber operating on toluene with oxygen-enriched air as an oxidizer (normally N_2/O_2 = 1.0). A small pilot burner operates continuously on methane to ensure proper starting of the main burner and to prevent accumulation of combustibles. The LORHO combustor was proven during the LORHO generator program, with a minimum amount of adjustment, to provide a steady uniform seeded plasma of sufficient conductivity to operate an MHD generator. During the final operating period the combustor backplate failed under an unusual operating situation because of the blockage of a water passage near the pilot burner. This component has been redesigned to improve the water circulation and, hence, the cooling capacity. The new backplate has not yet been refabricated, but the material has been procured. The oxidizer storage consists of fifteen 8.5-m³ (300-ft³) storage vessels which hold approximately 27,300 kg (60,000 lb) of gas when fully charged to 160 atm (2400 psi). This allows operating times of up to five minutes at burner conditions of 10 atm and 3100°K before the tank pressure drops to 80 atm (1200 psi). The storage tanks can be recharged overnight by means of valved tie lines to the existing AEDC liquid-oxygen (LOX) and liquid-nitrogen (LN$_2$) storage facilities. There is also a 4000-gal toluene storage tank, a 40-atm (600-psi) fuel feed system, and a 26.7-atm (400-psi), 15,000-gpm cooling water distribution system in the LORHO Facility. Flow schematics of the LORHO fluid systems are shown in Figs. 4 and 5. Oxidizer flow to the generator is measured with a venturi flow nozzle and is controlled automatically by an analog computer utilizing the measured pressure, temperature, and differential pressure and transmitting an electrical-pneumatic signal to a regulating valve. The control system will hold the mass flow constant to within one percent as the storage pressure and temperature decrease during a firing. Elaborate provisions are made for purging of all fuel and oxidizer lines with gaseous nitrogen subsequent to operation of the facility.

The LORHO magnet, Fig. 3, consists of massive steel pole pieces and a 170-turn saddle coil formed from 0.635-cm(1/4-in.)-thick aluminum plates insulated between turns by polyester glass insulation. The coil is powered by a 3-MW, 10,000-amp d-c power supply. A field of 2 tesla (T) is produced which is nearly uniform over the length of the channel. As will be noted later, this magnet installation must be modified to provide the field required by the high performance demonstration experiment.

The LORHO generator channel, Fig. 6, is a Hall configuration composed of 421 insulated, water-cooled electrode rings, 4.7-m (15.5-ft) long, with an exit diameter of 1 m (40 in.). Power is extracted using two terminals located at the ends of the channel with the burner end grounded and the downstream end at 10,000 v. When the generator was designed in 1964, the Hall configuration was selected because of construction simplicity and mechanical integrity. The test program verified that the choice of the Hall configuration was sound. However, this channel is completely inadequate for the demonstration experiment.

3

The generator output power is dissipated in water-cooled resistance tubes manifolded to supply and return headers by electrically insulating hose connectors. The load bank (Fig. 7) is composed of 276 tubes of different diameters, 6.1 m (20 ft) long. The resistance is adjustable by utilizing various combinations of tubes to provide from 0.35 Ω/tube up to 170 Ω for the entire bank. The load can dissipate more than 100 MW and uses 100 gpm of water at 20 atm (300 psi) for each MW dissipated. This bank is suitable for loading of the channel operating in the diagonal mode, but operation in the Faraday mode will require a new load bank.

An explosion-proof control room (Figs. 8 and 9) contains all of the necessary controls and instrumentation for remote operation. The equipment includes X-Y plotters, oscillographs, a Metrascope®, and four closed-circuit television (TV) systems. Conventional instrumentation is available for measuring current, voltage, temperature, and pressure. A Beckman 210® digital data acquisition system having 100 channels provides continuous on-line data acquisition. Data samples are taken at time intervals which can be as short as 25 msec. The data are recorded on magnetic tape and reduced using a Raytheon 520 computer.

The installed a-c electrical power capacity in the LORHO facility is 40 MW, obtained mainly from the Propulsion Wind Tunnel (PWT) Plenum Evacuation System substation. About 3 MW of this a-c power is consumed by various auxiliaries: main cooling water and fuel pumps, seeder pump, bearing pumps, unit heaters, hoists, fans, welders, control circuits, building lights, etc. Four separate rectifier units provide up to 25 MW of d-c power:

No. 1   1 MW - 500 v
No. 2   0.9 MW - 125/250 v
No. 3   3.1 MW - 300 v
No. 4   20 MW - 3000 v

Rectifier No. 3 is the source of power for the existing LORHO magnet coil, but it will not be adequate for the upgraded magnet proposed for the performance demonstration. Rectifier No. 4 is fed from an 11-MVA tap-changing under load transformer, Fig. 10. Since this transformer is rated at 31.6 MVA for five minutes of operation, this power supply can be expanded to operate the new magnet at the 27-MV level by addition of another diode bank in parallel with the existing 20-MW bank.

SECTION III
EXPERIMENT SIMULATION REQUIREMENTS

3.1 BASE-LOAD PLANT PERFORMANCE

The purpose of the proposed demonstration experiment is to provide conclusive evidence that an MHD generator can provide the performance required to make a commercial base-load plant an economic possibility. The performance of an MHD generator

is characterized by: energy extraction ratio, the fraction of available thermal energy which is extracted as electrical power; turbine efficiency, the ratio of actual power output to the work output in an isentropic process operating through the same pressure ratio; and the pressure ratio itself, combustion pressure divided by ambient exhaust pressure. It is necessary first of all to establish the MHD base-load plant performance requirements, and these can be obtained from existing analyses such as the four given in Table II (Refs. 2-5). Many other analyses could have been cited, but these four are thought to be typical. No USSR analyses have been presented since the Soviets are primarily interested in natural gas with higher preheat temperature and oxygen enrichment. Data from the British program (Ref. 6) are not presented since it is generally accepted that their analyses drastically overestimated the burner and channel heat transfer.

A few comments should be made concerning the designs presented in Table II:

Reference 2: The values of conductivity are probably realistic, but the generator design appears optimistic for an early plant. The peak Hall parameter and axial electric field are too high, and magnetic field variation would be required to achieve a realistic design, particularly if a diagonal generator is to be considered. When the magnetic field at the generator exit is decreased to a reasonable value (4 to 5 T), the generator length will increase to 20 m or more. The generator loading coefficient and turbine efficiency appear very high for an early design; other losses not considered in the design calculations will probably decrease these. The flow deceleration through the generator is high and might lead to boundary-layer separation.

Reference 3: As with Ref. 2, the magnetic field will have to be tailored to achieve acceptable values of the Hall parameter and electric field near the generator exit. The values for the conductivity appear optimistic.

Reference 4: This design appears to be realistic with acceptable values for the Hall parameter and electric field. The conductivity at the generator exit appears high and the length would increase to 20 m or more if lower values were utilized.

Reference 5: This design demonstrates the beneficial influence of increasing the preheat temperature to decrease the magnetic field strength requirement. However, this constant Mach number design at 1.1 is dangerous and could choke (go to M = 1 in the channel) with the slightest departure from the design conditions. Also the Hall parameter and electric field are too high at the generator exit.

Based on the existing studies, it can be concluded that, in order to achieve a 50-percent-overall base-load plant efficiency, the MHD generator must extract 20 percent of the available energy with a 70-percent turbine efficiency when operating at a 5-atm burner pressure. In addition, diffuser losses and the strong temperature dependence of the conductivity at the conditions appropriate to operation with coal and preheated air indicate that a subsonic channel is preferable to a supersonic design. A 6-T magnetic field at the channel entrance decreasing to about 4 T at the exit is required. A channel

length-to-diameter ratio of slightly under ten is necessary to achieve acceptable viscous losses. A composite of the existing designs can be made which eliminates some of the problems pointed out above and meets the performance requirements. The data for such a composite is given in Table III.

The MIT study, OCR Report No. 71 (Ref. 1), has suggested that the turbine efficiency specification for the demonstration experiment be decreased to 60 percent and the energy extraction maintained at 20 percent. This is a reasonable compromise since the demonstration represents a significant advance in the state-of-the-art and also will be more susceptible to electrode losses than the base-load plant. The approximate operating parameters for a base-load plant having a 60-percent turbine efficiency are also given in Table III. At the lower turbine efficiency the burner pressure must be increased from 5 to 6.75 atm and the channel length increased slightly in order to maintain the 20-percent energy extraction. These specifications for a base-load plant operating at 60-percent turbine efficiency are taken as the simulation requirements for the demonstration experiment. The objective, therefore, will be to duplicate in the demonstration the generator characteristic performance parameters: 60-percent turbine efficiency, 20-percent energy extraction, and 6.75-atm combustor pressure with atmospheric exhaust.

3.2 EXPERIMENT SCALING CONSIDERATIONS

Since it is impractical and expensive to perform the experiment at full scale, the performance demonstration will be conducted with a smaller sized device which simulates as nearly as possible the operating conditions of the commercial base-load unit. Proper simulation is necessary so that the experiment results are indicative of the performance of a full-scale generator. A proper balance between the cost of the experiment and uncertainties resulting from scaling must be sought. The uncertainties attributable to scaling must be fully recognized and should be minimized within cost constraints. A rational extrapolation of results to a full-scale design must be made, and design margins should be established to allow for uncertainties in the scaling process. Good simulation can be assured by duplicating between the experiment and full-scale certain nondimensional parameters which characterize the magnetogasdynamic process in the channel, as well as viscous and electrode losses. These nondimensional groupings which should be duplicated as near as practical are:

1. Magnetic interaction parameter, $S = (\sigma uB^2 L)/p$: ratio of the magnetic force per unit area to the gas pressure.

2. Mach number, M: ratio of local flow velocity to the speed of sound.

3. Load coefficient, $K = E/uB$: ratio of operating voltage to the open circuit voltage.

4. Hall parameter, Ω: product of the electron cyclotron frequency and average time between collisions; indicative of ratio of Hall field to the induced field.

5. Length-diameter ratio, L/D: to first approximation, viscous effects are proportional to L/D.

6. Reynolds number, Re = $(\rho u L)/\mu$: ratio of the inertia forces to viscous forces. Re is the basic parameter for determining the boundary-layer behavior, and a large value is required in order to achieve realistic simulation. Past experience in aerodynamics suggests that when viscous effects become important, as they are at the generator exit and in the diffuser, scaling is not accurate beyond a factor of three or four in Reynolds number.

7. Ratio of the electrode voltage drop to the open circuit voltage, V_e/uBD: this ratio determines the relative magnitude of the electrode losses and realistic simulation requires a large model.

The scaling laws relating the electrical and thermodynamic properties of an experiment with the base-load plant can be determined by fixing the first five of the above parameters. It is assumed that the gas composition is not changed significantly between experiment and full scale, that is, γ and R are the same. Then for an electron-neutral collision dominated plasma, the Hall parameter can be written approximately as $\Omega \sim (B\sqrt{T})/p$ ($\sim$ proportional to). With the Mach number written as $M \sim u/\sqrt{T}$, the interaction parameter can be expressed as

$$S = \frac{\sigma u B^2 L}{p} = \sigma BL \left(\frac{u}{\sqrt{T}}\right)\left(\frac{B\sqrt{T}}{p}\right) \sim \sigma BL(M)(\Omega) \tag{1}$$

Hence, if Ω, M, and S are the same in the experiment as in the base-load plant, then the conductivity must vary inversely with the product of the magnetic field and length and reduced scale may be compensated by an increase in σ and/or B. The scaling laws relating experiment and full scale, keeping the first five nondimensional parameters invariant, are

$$\frac{\sigma_e}{\sigma_f} = \frac{B_f L_f}{B_e L_e} = \frac{B_f D_f}{B_e D_e} \quad \text{Conductivity} \tag{2}$$

$$\frac{\dot{m}_e}{\dot{m}_f} = \frac{B_e L_e^2}{B_f L_f^2} = \frac{B_e D_e^2}{B_f D_f^2} \quad \text{Mass flow} \tag{3}$$

$$\frac{P_e}{P_f} = \frac{B_e L_e^2 T_e}{B_f L_f^2 T_f} = \frac{\dot{m}_e T_e}{\dot{m}_f T_f} \quad \begin{array}{l}\text{Electrical power produced} \\ \text{for fixed extraction ratio}\end{array} \tag{4}$$

$$\frac{Re_e}{Re_f} = \frac{B_e L_e}{B_f L_f} = \frac{B_e D_e}{B_f D_f} \quad \text{Reynolds number} \tag{5}$$

7

$$\frac{P_e}{P_f} = \frac{B_e \sqrt{T_e}}{B_f \sqrt{T_f}} \quad \text{Pressure} \tag{6}$$

$$\frac{J_e}{J_f} = \sqrt{\frac{T_e}{T_f}} \frac{L_f}{L_e} = \sqrt{\frac{T_e}{T_f}} \frac{D_f}{D_e} \quad \text{Current density} \tag{7}$$

where the subscript e refers to the experiment, f refers to a full-scale plant, and all quantities are appropriate average values.

These scaling laws provide a means to scale between various sized generators and assure that the magnetogasdynamic processes are simulated, including the growth of any instabilities. This can be seen by noting that the growth factor ($\omega_i t$) for magneto-acoustic waves in a Faraday generator can be written as

$$\omega_i t \approx \frac{\sigma B^2 L}{2\rho u} \left\{ -1 \mp \frac{\Omega M J_x}{\sigma u B} \left[\frac{eV_i}{2kT} (\gamma - 1) + \frac{3\gamma - 1}{4} \right] \right\} \tag{8}$$

where V_i is the seed ionization potential. The expression can be written as

$$\omega_i t \approx \frac{S}{2\gamma M^2} \left\{ -1 \mp \frac{(\Omega)^2 M(1 - K)}{1 + (\Omega)^2} \left[\frac{eV_i}{2kT} (\gamma - 1) + \frac{3\gamma - 1}{4} \right] \right\} \tag{9}$$

The scaling laws thus ensure that the growth factor will be duplicated provided the temperature is not significantly different. The growth factor of ionization waves will also be duplicated.

If viscous and electrode losses are neglected, the performance of an MHD generator channel is determined by S, M, and K, and these should be duplicated in any demonstration experiment. Duplication of the Hall parameter is not an absolute requirement for performance simulation, but duplication is considered necessary in a scaled device because of the dominating influence of the Hall effect on MHD generator design. It is seen that with thermodynamic parameters, flow velocity, and magnetic field strength duplicated, the interaction parameter is duplicated for constant σL product. That is, with losses neglected. the length itself is not important in the simulation but the product σL is. Reduced length can be compensated by a corresponding increase in conductivity of the working fluid.

3.3 SCALING LIMITATIONS

It is shown below that for a small range in geometric scaling. the relative viscous losses are not strongly dependent on scale. The turbulent boundary-layer displacement thickness is given by

$$\frac{\delta^*}{x} Re_x^{1/n} = Constant \qquad (10)$$

for a given Mach number and wall temperature. The ratio of δ^* to the channel (hydraulic) diameter, which determines the relative viscous losses attributable to skin friction and heat transfer, can be shown to be

$$\frac{\delta^*}{D} = Constant \cdot \frac{L}{D} \cdot Re_x^{-1/n} = Constant \frac{L}{D} \cdot L^{-1/n} \qquad (11)$$

For turbulent boundary layers, $n = 5$ to 7, and the dependence on L is seen to be quite weak. Thus, duplication of channel L/D ratio in addition to S, M, and K will ensure simulation of channel performance, including viscous losses to a first approximation. That is, (σL) scaling will account for viscous losses if the difference in scale is not too large. Therefore,

$$(\sigma L) \sim (\sigma D) \sim (\sigma \dot{m}^{\frac{1}{2}}) \qquad (12)$$

and (σL) scaling is thus equivalent to $(\sigma \dot{m}^{1/2})$ scaling.

By using cesium seeding and special fuels the mean experimental conductivity could be raised a factor of 30 above full scale, and, hence, the mass flow could be reduced to less than 1 kg/sec and still achieve apparent simulation. Unfortunately, such approximate considerations fail completely to include the real effects of boundary layer and electrode losses, since the L dependence in Eq. (11) becomes significant for such large changes in scale.

Figure 11 provides a comparison of calculated boundary-layer growth for generators having identical values of S, M, K, and L/D appropriate to the base-load generator, but with mass flows of 600 kg/sec (full scale), 60 kg/sec (high performance demonstration experiment), and 1 kg/sec. A comparison of the 60-kg/sec case and the base-load case shows a small difference, and, hence, the δ^*/D is only slightly dependent on scale. At 1 kg/sec, however, $2\delta^*$ is almost 25 percent of the diameter and relative viscous losses are high. In terms of the total velocity thickness, the boundary layers would be essentially merged at the channel exit. Extrapolation of channel performance from the 1-kg/sec case to full scale would be much less certain than extrapolation from the 60-kg/sec case.

In addition to the disproportionate performance penalty paid for large viscous losses, reduced model scale also introduces uncertainties in the channel loft which become more and more important as the absolute size is reduced. Figure 12, giving channel area ratio distributions for the three cases covered in Fig. 11, shows that the calculated displacement thickness corrections to the channel loft are very nearly the same at 60 and 600 kg/sec, but are much greater at 1 kg/sec.

9

It is apparent that while the scaling laws are useful for sizing the experiment, the relations cannot be applied indiscriminately over a large size range. The Reynolds number is the basic parameter for determining boundary-layer behavior and can also be the basis for establishing the range over which the scaling laws can be confidently applied. It has been the experience of the AEDC in over 20 years practice in simulation of full-scale aerodynamic devices by experiments that extrapolation beyond a factor of 3 or 4 in Reynolds number is hazardous in situations where viscous effects are important. Instances of expensive modifications to aircraft hardware and/or performance limitations can be cited as resulting from scaling over too wide a range in Reynolds number. One example is that of the C-141 transport, which was designed on the basis of model tests conducted at Reynolds numbers which were lower than full scale by a factor of approximately ten. In actual flight at high subsonic airspeeds the shock wave/boundary layer interaction on the upper surface of the wing was appreciably different in location and character than in the model tests. The resulting change in aerodynamic load distributions on the wing necessitated restrictions on the performance of the aircraft and a reduced load carrying capacity. In the past, MHD generator channel performance has been found sensitive to the same type of Reynolds number dependent effects which affect flows over aircraft wings, such as boundary-layer growth and separation.

Assuming that the magnetic field is invariant and utilizing Eqs. (3) and (5), the Reynolds number ratio can be expressed as

$$\frac{Re_e}{Re_f} = \sqrt{\frac{\dot{m}_e}{\dot{m}_f}} \tag{13}$$

Then at 1 kg/sec the Reynolds number is down a factor of 25 below a full-scale plant operating at 625 kg/sec. This is well beyond the limit for confident scaling. However, at 60 kg/sec the Reynolds number is down only a little over a factor of three from full scale, and results from an experiment of this size could be extrapolated confidently to the base-load plant.

In addition to the viscous effects, the relative electrode losses are also dependent on the absolute channel size. For square generator channels, the ratio of electrode losses to the channel power output can be written approximately as

$$\frac{P_{elec}}{P} = \frac{2j_y V_e L D}{\rho u D^2 \Delta H} \tag{14}$$

Data (Refs. 7 and 8) taken in peg-wall channels indicate that the electrode voltage drop can be approximated by

$$V_e = a + b(x j_y) \tag{15}$$

10

Since the thermodynamic parameters and velocity are invariant in the scaling at constant magnetic fields, the average loss can be expressed as

$$\overline{P}_{elec}/P = \text{Constant} \cdot J_y(a_o + bI.J_y) \ L/D \tag{16}$$

Then, since a and b are relatively independent of scale and $J_y \sim 1/D$

$$\overline{P}_{elec}/P \sim 1/D \sim 1/\sqrt{\dot{m}} \tag{17}$$

for generator channels of different size, but having equal values of S, M, K, and L/D. Since $\dot{m}$ can potentially vary through a factor of nearly 10^3 below full scale, small experiments are severely penalized, and indeed, values of $\overline{P}_{elec}/P = 0.5$ are not uncommon in small generators.

The electrode loss in the high performance demonstration at 60 kg/sec using the LORHO Facility has been calculated to be approximately eight percent of the power generated. Although such a loss is objectionable, it is tolerable, and should be reduced with the graphite-carbon electrode which will be used. On the other hand, an experiment at 1 kg/sec would have much higher electrode losses and, hence, little chance of achieving the performance demonstration specifications.

Another factor, in addition to viscous effects and electrode losses, which limits the scaling from full size is the variation of the electrical conductivity through the generator. For a base-load plant operating on coal with preheated air, the conductivity at the generator exit is one-fourth of the entrance value. As the generator size is decreased below full scale, the conductivity and, hence, temperature must be increased in order to preserve the interaction parameter, S. At the higher temperature, the slope of the conductivity-temperature curve is less steep and the conductivity does not drop off as fast as the temperature decreases through the generator. A typical conductivity-temperature curve is shown in Fig. 13, and the conductivity variations through a full-scale generator, a 60-kg/sec scaled experiment, and a 1-kg/sec experiment are superimposed. The conductivity is almost constant in the 1-kg/sec experiment and decreases a factor of about 1.7 in the 60-kg/sec experiment. It is obvious, then, that simulation of the variation of the electrical parameters through the generator requires a relatively large experiment. It is concluded that although superficial simulation can be achieved on a small scale, the high performance demonstration experiment should be conducted on as large a scale as practical to provide results which can confidently be extrapolated to the full-scale plant.

3.4 FOUR EXPERIMENT OPTIONS

The scaling laws outlined in the previous section can now be used to determine the feasibility of several different sized experiments. Four different sized experiments, each involving a more extensive modification to the LORHO Facility as the size increases, were considered for the high performance demonstration experiment. Approximate cost estimates for system renovation, magnet, magnet power supply, and generator channels were made for each of the experiments in order to judge the relative costs. These estimates

11

do not include operating costs, instrumentation, cost of consumables, or any other items which would be the same for all the experiments, and, hence, the estimates are not the total cost of any single experiment. The specifications, relative merits, and costs of the four experiments are as follows:

3.4.1 Existing LORHO (Option A)

This experiment would utilize the existing 2-T magnet (4 m of useful field) and fuel-oxidizer system. According to the scaling laws, a demonstration on this scale would produce 10 MW, the conductivity would be a factor of 13 higher than full-scale plant, and the Reynolds number lower by the same amount. Even with pure O_2 (using toluene) and cesium seed, the σu and Ω required for simulation could not be achieved and, also, the Reynolds number would be well below the range for confident scaling. Although its relative cost would be only $600,000, this option would not meet the requirements for the demonstration experiment.

3.4.2 LORHO Upgrade I (Option B)

This experiment would utilize the existing fuel-oxidizer system and burner. The existing magnet coil would be precooled to $77°K$ (LN_2 temperature) and steel added to decrease the bore and to fit snugly against the channel. The magnet would provide 5.5 T over 4 m when driven at the 20-MW level using a modified existing power supply. The relative cost of this experiment would be $1.2 million, but it would not be feasible for two reasons. First, the high temperature (high σu) required for simulation would make operation of the existing burner and a heat sink channel marginal. Second, and of critical importance, the magnetic field would be constant over the entire generator length and intolerable Hall fields would occur near the generator exit.

3.4.3 LORHO Upgrade II (Option C)

This experiment would utilize the existing fuel-oxidizer system operating at a flow rate of 60 kg/sec. The magnet length would be increased to 7 m to provide 5.5 m of field and 6 T near the entrance (decreasing through the generator), thus allowing for a reasonable Hall field. The magnet would be LN_2 cooled, steel would be added to the yoke, the bore would be tapered to fit the channel, and an existing power supply would be modified to provide 27 MW of power to drive the magnet. The temperature (σu or N_2/O_2 ratio) required for simulation would be reasonable and the heat-transfer rates to the burner and heat sink channel would be acceptable. The relative cost of this experiment would be $1.5 million and would provide a good demonstration experiment.

3.4.4 100-MW Electrical (Option D)

This experiment would produce 100 MW_e using a 6-T (decreasing to 3.8 T at the generator exit) LN_2-cooled magnet about 10 m long with a 0.9-m square inlet and 1.5-m square exit. The experiment would require a new burner, modifications to the N_2/O_2

system, and additions to the existing power supply. The experiments would be a good simulation of the full-scale commercial generator and would have a relative cost of $3.1 million.

Based on the feasibility and expected performance, options C and D are considered to be the only logical choices for the demonstration. There is a considerable cost differential between C and D, but the simulation of the base-load plant for purposes of demonstrating efficiency is not significantly different. It is concluded that an experiment conducted in the LORHO Facility at 60 kg/sec (Option C) is the most cost effective means of providing a definitive and favorable demonstration that the requisite generator performance can be achieved. The experiment will provide good simulation of all the nondimensional groupings listed previously which characterize the generator performance. This will also assure that electro-thermal and magneto-acoustic instabilities as well as the overall transient behavior of the generator will be simulated.

The mass flow of the proposed high performance demonstration experiment is about one-tenth that of the base-load plant, but an order of magnitude greater than is available in other existing facilities. Thus, its scale will be approximately $1/\sqrt{10}$ of the base-load plant. The relative scale of the proposed demonstration experiment as compared to the base-load plant and several other MHD generators is shown in Fig. 14. Here the relative Reynolds number is shown based on having the Hall coefficient, magnetic interaction length, and flow Mach number the same for all experiments (Eq. (5)). This requires the electrical conductivity to be increased as the scale of the experiment is reduced (which physically cannot be realized for the very small-scale experiments). In simplest terms, Fig. 14 shows what can be done on a relative scale in the various MHD generators when the N_2/O_2 ratio and gas temperature and conductivity are allowed to vary. It shows, that no other on-going or proposed experiment will yield information on overall performance, on effects of instabilities, or on end-effect losses that was not or could not have been shown in the Mark V and LORHO programs.

The high performance demonstration generator is the only generator, existing or proposed, of sufficient size (Reynolds number within a factor of three of full scale) to allow confident scaling of viscous effects on the base-load plant. At this $1/\sqrt{10}$ scale, the experiment will achieve a reasonable simulation of boundary layer and electrode loading of the full-scale generator, whereas an experiment performed at any significantly smaller scale would be dominated by viscous and electrode losses. This experiment will permit the comparison of sophisticated analytical techniques now being developed with data from a generator not dominated by losses. Lastly, it is important to note that the experience and performance data gained from this demonstration experiment will be directly applicable without any scaling to the 300-MW (thermal) MHD pilot plant proposed in OCR Report No. 71.

SECTION IV
GENERATOR CHANNEL DESIGN

4.1 AERODYNAMIC DESIGN

A linear MHD generator channel in its simplest form is a duct performing two functions: (1) confinement of a flowing plasma through a controlled expansion process, and (2) providing electrical connection with the plasma in order to extract electrical energy. Such a linear generator channel can have any of four basic configurations illustrated in Fig. 15. The basic configurations differ only in external electrical connections and, in principle, by use of a "patchcord" system, a given segmented channel equipped with "peg" walls could be used for experimentation in any desired configuration. In the base-load case, neither the Hall nor continuous-electrode Faraday configuration can approach the specified performance. Therefore, to achieve the performance goals, the configuration options are restricted to a channel capable of operation in either the segmented Faraday or diagonally connected modes.

For the proposed high performance demonstration generator, a supersonic flow is deemed unacceptable because of the large and probably intolerable reductions in conductivity which would result from the supersonic expansion of the combustion products which will be used. In addition, recovery pressure losses associated with diffusion of a supersonic flow would be a significant factor in limiting the overall efficiency of such a device. Consideration of inviscid flow stability, prevention of excessive boundary-layer growth, and boundary-layer separation requires an accelerating flow through the generator. As indicated in Refs. 7, 8, and 9, the most stable configuration for an MHD channel which has an accelerating subsonic flow is one in which the exit is sonic. The operation of such a channel is indicated in Fig. 16. It is assumed that under zero (or light) loading, sufficient chamber pressure is available to result in a fully supersonic flow as indicated by line "A" in Fig. 16. With increasing loading, the accompanying loss in recovery pressure would result in an upstream-propagating shock wave, one position of which is indicated by line "B". In fact, as shown in Ref. 8, such a flow situation can be stabilized. With increased loading the shock will disappear through the upstream throat, leaving a situation as indicated by line "C". This is the selected operating point for the present design. Further load increase leads to the condition with an accelerating subsonic flow and subsonic exit. It seems likely that a final refined design will incorporate an accelerating flow with an exit Mach number slightly less than unity in order to provide stability to both increases and decreases of load.

The plasma flow within the generator also is influenced by the magnetic field distribution. Of particular concern are the fringe fields which can introduce eddy current flows with associated joule heating. On the other hand, fringe fields can be used to advantage in power takeoff as in the original LORHO (Ref. 10) generator. For the present design, these effects are to be included by allowing the generator to extend into the fringe fields for a sufficient length such that the magnitude of the induced fields at the ends is small in comparison with the values within the channel. The magnetic field distribution and relative channel location are shown in Fig. 17. In this fashion the end losses introduced

14

by magnetic field fringing are largely incorporated in the design calculations and additional losses should be minor. This probably results in less than optimum operation but minimizes risk, particularly with the diagonal configuration.

The specifications for the design of the high performance demonstration generator can be summarized as follows:

Mass flow	= 60 kg/sec
Combustion pressure	= 6.75 atm
Fuel	- toluene (C_7H_8)
Oxidizer	- N_2/O_2 = 1.25
Seed	- KOH dissolved in methanol
Flow	- subsonic
Magnetic field	= 6T maximum
Diffuser exhaust pressure	= 1 atm
Turbine efficiency	= 60 percent
Enthalpy extraction ratio	= 0.20

The design makes full use of the experience gained from the operation of previous MHD generators and concentrates on providing the improvements required to achieve high energy extraction and high turbine efficiency. Computer programs utilizing conventional analytical and empirical techniques have been adapted for prediction of the behavior of MHD channels under the operating conditions of the demonstration unit. A description of the programs is given in Appendix II. The calculations preserve an inviscid core with a boundary layer and incorporate electrode voltage drops and other phenomena as appropriate. The boundary-layer calculations are used to provide virtual wall displacement and an estimation of diffuser recovery capability. The flow is subsonic throughout the channel. An accelerating flow with choked exit assures stability of both inviscid core and boundary layer. An N_2/O_2 ratio of 1.25 has been used to obtain the electrical conductivity required by the $\sigma\sqrt{\dot{m}}$ scaling to maintain an L/D appropriate to a base-load generator.

The channel is designed for operation in either the segmented-electrode, individually loaded Faraday or externally connected diagonal mode. In the diagonal mode, the channel can operate either with a single output, multiple current tapping, or with grading resistors. In order to have this flexibility, it is necessary to provide the channel loft (area distribution) for the diagonal configuration and then develop an appropriate loading distribution for operation in the segmented-electrode mode. The transverse current distribution (with x) is insensitive to the operating configuration for a given channel loft and similar velocity distributions. Thus it is only necessary to investigate one diagonal configuration. The single output operating mode is selected since it will probably display the highest losses relative to the Faraday configuration with individually loaded electrode pairs. The Faraday and single output diagonal configurations should provide the upper and lower bounds for generator performance.

Diagonal Design: For the single output diagonal operating condition, the total current is specified. Inlet conditions and degree of impulse (negative) are selected to give a choked

15

exit with accelerating flow and sufficient recovery pressure for exhaust to the atmosphere. Figure 17 shows the channel contour and dimensions along with the magnetic field distribution. Power takeoff occurs in the fringe fields at either end where the electric fields have been reduced to a very low value, and some axial current flow with consequent losses has been accepted. For a single output the wall angle has been pitched up almost normal to the flow at the downstream end in order to minimize the volume involved in power takeoff at a high value of the Hall coefficient. The technique resembles that utilized for power takeoff with the original LORHO channel. The predictable internal losses attributable to this method of power takeoff have been accepted in order to minimize uncertain end-effect losses. This can be seen by examination of Figs. 18, 19, and 20, which show voltage distribution, electric field distribution, graphite electrode voltage drop, and current distribution as a function of distance along the channel. (Note that the electric fields are almost zero at the channel ends.) A detailed discussion of the considerations required to properly diagonalize a generator is presented in Section 4.3.

Faraday Configuration: For analysis of the Faraday configuration, the channel area and velocity distribution for the diagonal configuration is imposed, the axial current is set equal to zero, and the transverse current and loading schedule for the segmented electrode is computed as given in Figs. 20 and 21. The load to be connected to each electrode is equal to RL divided by the distance between the segmented electrodes. Figures 22 and 23 show the voltage and field distributions for the segmented-electrode configuration. It should be noted that the total channel voltage in either configuration is about 12,000 v which can be handled in the existing LORHO Facility. Also, the axial electric field (E_x) does not exceed 2500 v/m and should not present any electrical breakdown problems. The excellent Faraday performance is due to the more uniform E_y distribution over a greater length of the channel and to the zero Hall current which reduces the internal dissipation. The transverse current density in the two configurations is nearly equal, as shown in Fig. 20.

Figure 24 shows the variation of certain flow parameters as a function of distance along the channel. With the exception of conductivity, variation of the parameters is almost identical for the two configurations. A higher seed concentration can be utilized for the Faraday because of reduced internal dissipation. It should be noted that if potassium seed is inadequate to provide the required conductivity, cesium seeding is available as a safety factor. Figure 25 shows the variation of output power along the channel.

A comparison between one- and two-dimensional calculations for the slant-wall configuration is made in Appendix III. The predicted electric field and current distributions obtained from one- and two-dimensional analyses (without electrode voltage drops) are almost identical, but the two-dimensional analysis predicts choking (M = 1) a significant distance upstream from the channel exit choke point predicted by the one-dimensional calculations. When the electrode voltage drop is included within the analyses, the one- and two-dimensional calculations predict essentially the same choke point. The difference between the predicted total generator power output obtained from the two analyses is only a few percent.

The influence of boundary-layer characteristics on the design is indicated in Figs. 26 and 27. Boundary-layer separation should not be a factor because of the accelerating flow; however, boundary-layer displacement thickness exerts a decisive influence on the channel loft. Figure 27 shows the inviscid loft compared with the loft including the boundary layer and indicates that the displacement thickness is approximately 10 percent of the channel diameter. The channel exit conditions are sufficient to allow recovery to atmosphere using an 85-percent-efficient subsonic diffuser.

The design operating conditions calculated for the channel in the two flow configurations are summarized in Table IV. The achievement of this generator performance will provide confidence in the ability of an MHD generator to achieve the required performance for a base-load plant and, together with the results of other OCR programs, provide the basis for design of a pilot plant and the full-scale unit.

4.2 MECHANICAL DESIGN

In an MHD generator, aerodynamic steady state is achieved approximately one second after full burner flow has been established (Ref. 7). Since this is the case, and in order to minimize cost and thermal expansion effects and maximize flexibility, a heat-sink, peg-wall channel will be provided for initial examination of generator efficiency. Only the inlet and exit flanges will be water cooled to minimize thermal distortion. The basic features of the design are as follows:

1. Insulating Walls: Solid copper pegs separated by thin sections of refractory insulation and set into laid-up fiber-glass retaining walls supported by external stiffeners and tie rods.

2. Electrode Walls: Graphite and/or carbon segments with a pitch of 0.8 to 1.0 cm separated by insulation, and set into copper/stainless steel retainers which in turn are set into fiber-glass retaining walls. Grade and/or thickness of carbon or graphite can be varied along the channel to achieve proper electrode surface temperature.

3. Power Takeoff: Output leads for each pair of segmented electrodes to be integral with channel so as to tie to patch panels at upstream and downstream ends of the magnet. Patch panels can be used to connect to individual loads for segmented electrodes, or to diagonalize the test externally.

Figure 17 shows the relative location of magnet poles and coils, the magnetic field distribution, the channel loft, and the location of metal inlet and outlet flanges which couple the channel to the nozzle and diffuser, respectively. The flanges are located at the approximate point of magnetic field reversal and low electric field in order to avoid the possibility of a cascading short circuit through the flange as was once experienced at the exit of the Mark V (Ref. 11). Peg walls and electrode segmentation are extended

17

all the way to the flanges. The overall length of the complete channel including the flanges is 8.98 m, (29.4 ft). The length between points where the field begins to fringe is 5.5 m (17.9 ft), whereas the full length utilized for power takeoff is 7 m (21.8 ft) between points where the field is 2.5 T and 3.1 T, respectively, at inlet and outlet.

With the magnetic field in the vertical direction, the peg walls are at the top and bottom and the electrode walls are on the sides. Unsupported peg walls exhibit negligible rigidity in both longitudinal and transverse directions, whereas segmented-electrode walls are fairly stiff transversely but weak longitudinally. Mechanical design of a channel of this scale involves careful attention to the support of the relatively flimsy electrode and insulating walls during fabrication, mating and assembly with the other walls, pressure checking, transport, insertion and extraction from the magnet, and operation. Channel design, construction, and handling will resemble that of the ·Mark V. Absence of water cooling in peg and insulating walls will simplify the design, but the channel is substantially longer than that of the Mark V (29 ft versus 16 ft).

Since it is vital to prevent hot gas leaks during operation, an extremely important feature of the design will be the requirement for a pressure check of the channel at the maximum expected inlet pressure of 5 atm. This requirement should not be difficult to meet since deflection sensitivity of the heat-sink channel should be much less than for a water-cooled channel. An in-place pressure check with the channel installed in the magnet and hooked up to the nozzle and diffuser will be specified as a standard operating procedure.

The channel will be built on a tracked dolly which is utilized as a transporter when the channel is out of the magnet. The lower peg wall is assembled first on the fiber-glass retaining wall. The electrode walls which are assembled separately are then added. Finally the top peg wall is put on. The wall joints are extremely critical for leak prevention, and it is expected that an external lap member will be added to improve the sealing capability. Pressure integrity should be improved over the Mark V channel since fiber-glass retaining walls will be utilized. The side and top walls will be built and then clamped in a retaining jig so that they can be moved and oriented for assembly. The dolly and all special construction bases, jigs, and moving fixtures for the individual parts will be supplied with the channel.

Figure 28 shows the overall channel longitudinal dimensions as well as important internal dimensions, and the expected voltages during operation are indicated. From the active region, the channel will be continued to the flange with a rate of change of area equal to that at the ends of the active region. This will provide a minimum area at the inlet to assist in isolating the burner from the channel. The exit section of the channel will serve as the entrance section of the diffuser.

Calculation procedures can be used to predict the channel heat loading as a function of axial station. However, since experimental heat-transfer data are available from both Mark V and LORHO, in which the channel inlet and nozzle throat conditions and

burner-induced turbulence closely resemble the present case, scaling of these data to the present case should give the best results. Using the scaled data, the estimated heat-transfer rate to the channel was obtained as a function of axial station and is shown in Fig. 29. The peg wall must absorb this heat load for the test duration without overheating of the peg surface. Figure 30 shows peg surface temperature versus axial station after 10 and 15 sec based on the assumption that the pegs cover 70 percent of the wall surface but absorb all of the heat load. The 70-percent figure should be conservative. It is seen that 15-sec runs should be achievable. Peg depth must be controlled to limit the average peg temperature after thermal sink to 320°C or less so that the fiber-glass retaining walls are not damaged.

A simplified sketch of the electrode wall configuration is shown in Fig. 31. It is indicated schematically that in regions of low heat transfer at the downstream end of the channel, holes are drilled through the electrode to decrease the thermal capacity and increase surface temperature. The electrodes are capped with graphite or carbon with the grade depending on axial location in order to give approximately the same electrode surface temperature at all stations. Experience indicates that graphite-carbon is the optimum electrode material for short-duration experiments (Refs. 7 and 8). It is inexpensive, easy to fabricate and replace, provides a relatively smooth surface with good plasma contact, and is immune to thermal shock. Ablation by reaction with the gas eventually necessitates replacement, but life can be extended by running slightly rich with the electrode temperature slightly under the value where corrosion by CO_2 and H_2O becomes diffusion limited. The electrodes are set into copper retainers for heat sinking and then into stainless steel holders which provide lateral stiffness. The electrodes are bolted to the fiber-glass retaining wall with one through conductor to the output circuit. The output conductors are staggered on successive electrodes to provide room to attach the integral power takeoff leads to the patch panels.

4.3 CHANNEL DIAGONALIZATION

As pointed out previously the demonstration generator will be constructed with segmented electrodes and insulated B-field walls for operation in both the Faraday and the externally connected slant-wall configuration. The diagonally connected MHD generator offers single-circuit output with an efficiency close to that of the Faraday configuration. However, proper diagonalization of a heavily loaded MHD generator operating through a substantial pressure ratio with high energy extraction is a difficult task requiring close attention to detail and compromises which necessarily limit the efficiency below the ideal Faraday performance. The important factors which must be taken into consideration for a properly diagonalized channel are:

(a) Conductivity variation through the channel

(b) Potential, electric field, and current continuity

(c) Two-dimensional effects and pitch variation

(d) End effects and power takeoff

19

4.3.1 Effects of Variable Conductivity

The variation of the working fluid electrical conductivity through the generator is of fundamental importance for proper diagonalization, that is, specification of the slant angle. This can be seen by noting that the relationship between the tangent of the slant angle, ϕ, and the loading coefficient, $K = E_y/uB$, for an ideal diagonalization ($j_x \equiv 0$), can be written as

$$\phi = \frac{E_y}{E_x} = -\frac{K}{\Omega(1-K)} \tag{18}$$

and

$$K = \frac{\phi\Omega}{\phi\Omega - 1} = \left(\frac{\rho\Omega}{B}\right)\left(\frac{1}{m}\right)\frac{1}{\sigma} \tag{19}$$

The quantities in parentheses are approximately constant for a given generator operating point; hence, the loading coefficient varies as σ^{-1}. The maximum value of K is unity for which $\phi \rightarrow -\infty$.

The conclusion that can be drawn from the above is that an "ideal" diagonalization ($j_x \equiv 0$) of a generator in which the conductivity varies substantially cannot be accomplished without an unacceptable sacrifice of efficiency in the upstream portion of the generator where the conductivity is the highest. In a small generator where the conductivity is almost constant (see Fig. 13) the problem is not so severe. With significant conductivity variation, however, some axial current flow must be accepted in the downstream portion of the generator.

In the present design, a finite axial current is allowed at the channel station where the slant angle would begin to increase because of decreasing conductivity (Fig. 20). This is achieved by a forced reduction of the wall angle beginning at this axial station and decreasing to a low value at the exit (Fig. 17). The small wall angle at the exit greatly alleviates the problems with end effect and power takeoff.

4.3.2 Potential, Electric Field, and Current Continuity with an External Diagonalization

The basic principle of an external diagonalization is to connect together a point on the anode (positive electrode) with a potential V^+ to a point on the cathode with a potential V^- equal to V^+ using an external wire. Since the current in this wire is continuous, $j_y D_z s$ on anode and cathode should be the same, where D_z is the channel dimension along B-field lines and s is the electrode pitch. Further, since the potential difference between this wire and its neighbors is the same at both ends, $E_x s$ should be the same. Thus, the three elementary conditions for diagonalizing a given generator for which the current and potential distribution has been computed are

$$V^+ = V^- \qquad \text{(a)}$$

$$j_y D_y s|^+ = j_y D_z s|^- \qquad \text{(b)} \qquad\qquad (20)$$

$$E_x s|^+ = E_x s|^- \qquad \text{(c)}$$

Unless special measures are taken to ensure that Eq. (20a), b, and c are satisfied simultaneously, they will be satisfied only if the equipotentials are normal to the direction of flow everywhere. As ϕ decreases from zero, careful attention must be given to satisfying Eq. (20) in detail. Assuming that (20a) is satisfied, then (20c) implies that

$$s = \left(\frac{E_{x,max}}{E_x}\right) s_{min} \qquad\qquad (21)$$

where $E_{x,max}$ is the maximum value of E_x encountered along the channel, s_{min} is the value of s where $E_x = E_{x,max}$ and is usually the minimum value of s which can be fabricated and assembled. Note that by satisfying (20c) the voltage between adjacent electrodes has been made uniform along the length of the channel, that is, $E_x s$ is a constant at the maximum value. Since j_y and s are known, D_z is given by (20b). Since the area is determined by the gasdynamics, the channel in general will be nonsquare in order to satisfy (20b). The aspect ratio $AR = D_y/D_z$ is

$$\sqrt{AR} = \frac{j_y \sqrt{A}}{(j_y \sqrt{A})_i} \qquad\qquad (22)$$

where station i is the location where the AR is unity. Usually station i is close to the point where the magnetic field begins to fringe at the exit, where a square cross-section channel can most efficiently utilize the aperture of a magnet which "hugs" the channel contour. Note that station i and the station where $E_x = E_{x,max}$ need not be the same, but $E_{x,max}$ should occur close to the channel exit to achieve maximum field utilization as the present design does.

Figure 32 shows the calculated values of s/s_{min} and AR as a function of distance along the channel for the present design. Although other designs will display differences in detail, the data appear to be typical. The pitch and AR increase in the fringe field near the channel ends because the electric fields decrease far more rapidly than the current density in this region. Heat-transfer losses and magnet utilization limit AR, and values greater than about 2 to 2.5 are probably undesirable.

It seems convenient to divide a channel into three types of regions as illustrated in Fig. 33. The first is the distance along the channel axis between x_3 and x_4 over which a proper diagonalization can be effected, and second is the transition regions between x_2 and x_3, and x_4 and x_5 at the inlet and exit. The third is the inlet (x_1 to x_2) and exit (x_5 to x_6) fringe regions where end effects are dominant.

21

Approximately

$$x_3 - x_2 \cong \tfrac{1}{2}\phi_3 D_{y3}$$
$$x_5 - x_4 \cong \tfrac{1}{2}\phi_5 D_{y5} \tag{23}$$

It is observed that low values of ϕ and AR near unity will minimize the transition regions and maximize the length over which the diagonalization can be effected. For other things equal, the lowest values of ϕ are obtained when Ω/B is high. In this respect, as well as for increased conductivity, dry coal and charcoal are desirable fuels because of the low water content of their combustion products.

In the design here, the overall active generator length of 7 m is divided as follows:

$x_2 - x_1$	1.0 m	Inlet fringe (AR = 2)
$x_3 - x_2$	0.55 m	Inlet transition
$x_4 - x_3$	4.6 m	Generator proper
$x_5 - x_4$	0.25 m	Exit transition
$x_6 - x_5$	0.60 m	Exit fringe

The effect of decreasing ϕ in reducing the exit transition and fringe regions is clearly evident. Conversely, the high values of AR and ϕ near the inlet lead to increased transition and fringe regions. This, in effect, provides a further limitation on usable maximum values of AR. As AR increases moving toward the inlet, a point is reached where the increase in the extent of inlet fringe and transition regions is so rapid that no increase in the generator proper is achieved.

4.3.3 Two-Dimensional Effects and Pitch Variation

Although the previous considerations are necessary, they are not sufficient to define the diagonalization. The distribution of ş as defined previously leads to equal walls. Certainly, this can never lead to the diagonalization depicted in Fig. 17, since the number of electrode segments on the negative wall is obviously smaller than on the positive wall if there is equal pitch on both walls at a given station. The reason for this is that the electric field distribution is two-dimensional in regions where the mean j_x is changing with x.

The one-dimensional analytical results can be used to arrive at an estimate of the magnitude of the two-dimensional effect. Using the mean value of j_x, $\Delta \cdot j = 0$ can be written

$$-(j_y^- - j_y^+) = -2\Delta j_y = AR\, D_z \frac{dj_x}{dx} + j_x \frac{1}{D_z} \frac{dA}{dx} \tag{24}$$

where j_y^- and j_y^+ are the values of j_y on negative and positive walls, respectively, and are different because the axial current changes with x. The quantity Δj_y is an estimate of the deviation from the mean j_y at the negative wall. It is only an estimate since the quantities involving j_x will actually be variables in the cross section.

The ratio $(\Delta j_y / j_y)$ is not small in situations of practical interest. For instance, for $\phi = -0.45$ at 6.5 m in the AEDC design, $\Delta j_y / j_y = 0.23$ from Eq. (25), corresponding to a 50-percent difference in body force between the two walls. Although the axial current does not extend over the entire channel, a body force difference of this magnitude at a Hall coefficient of three could cause serious loss of output because of nonuniformities. Additionally, the highest body force is on the negative wall where the pressure and momentum are lowest due to the transverse body force arising from the axial current. As this is the case, the two sources of nonuniformity reinforce each other. The extent to which these compounded effects can be tolerated without unacceptable losses is not known, but can be studied in the demonstration generator. Such studies would help to define limits to single load diagonalization, and the extent of current tapping required to reduce two-dimensional effects.

The electrode pitch distribution can be achieved in one of two ways. The first way is to provide the calculated pitch at every station. The second way is to build the channel with uniform minimum electrode pitch, and pitch variation would then be achieved on the average by scheduled shorting of a pair of adjacent electrodes on an appropriate wall. This may be acceptable, but could be difficult and lead to an effective increase in the s/D_y ratio. On the other hand, this method is flexible.

4.3.4 End Effects and Power Extraction

End effects and power takeoff are of great importance for the design of a diagonal MHD generator. A possible approach to alleviate these problems is the use of multiple grading loads to tailor the current and field distributions in the channel ends. However, there is considerable question as to whether the power in these grading loads can be recovered economically in a practical inverter system. If 80 to 90 percent of the power is delivered on a single load, then, as would typically be the case in a base-load unit, the remaining 10 to 20 percent is distributed among about 200 highly different grading loads. It might be better to deal with 1000 to 2000 more or less similar and somewhat independent individual segmented-electrode pair loads, or take the power on a single load with the probable consequence that a substantial portion of the power which would have been developed in the grading resistors will be dissipated as joule losses in the gas. In a base-load unit, a large portion of this heat loss will be recovered as work in the steam plant, and the advantage of a single inverter circuit with the resulting economy and reliability would result. It seems that a realistic analysis of the generator-inverter combination in a power system using truly representative values for the number of loads, for the three configurations (individually loaded segmented pairs, diagonal with grading, and/or tapping, and single circuit diagonal) would be of definite value in pointing the way to the most useful configuration for the base-load plant. As pointed out previously, the AEDC design has the flexibility to be operated in all three configurations.

The high performance generator design data presented here has concentrated on a single circuit power takeoff so that performance can be bracketed between the single circuit diagonal and the individually loaded segmented-electrode configurations. As seen in Fig. 20 for the two cases, the addition of grading resistors and/or multiple loading which preserves the j_y current distribution will result in nearly identical aerodynamic performance for the two modes of operation. The design is directed toward, first, minimization of the losses and, second, minimization of current and electric field concentrations which can damage the generator. As demonstrated by experience with the LORHO generator, both are facilitated in the design by:

1. Locating the power takeoff in a region of minimum electric field so that breakdown possibilities are minimized and current concentrations are reduced in magnitude.

2. Providing means for the power takeoff to occur along magnetic field lines, that is, to the "B" walls in addition to electrode walls and nozzle.

3. Minimizing the extent of the fringe regions.

<div align="center">

SECTION V
MAGNET SYSTEM DESIGN

</div>

5.1 MAGNET/POWER SUPPLY OPTIMIZATION

The high performance demonstration requires a 6-T saddle magnet in order to simulate the commercial plant operating conditions, and generator channel design calculations indicate the field distribution should be approximately as shown in Fig. 17. One means of obtaining this field is to extend the existing LORHO magnet coil and steel and to add steel (poles) to form a tapered aperature. This coil would be precooled to 77°K (LN$_2$) but would not be tapered to follow the bore and, hence, would not have an optimum configuration. This magnet configuration would require better than 40 MW to produce the required 6-T field, and would require a completely new power supply costing on the order of $860,000.

A more cost effective means of producing the required magnetic field is to design a new magnet coil (utilizing the existing steel) matched to a modified version of the existing 20-MW power supply. Preliminary calculations indicated that 27 MW at 1600 v would be sufficient to produce the required field and this could be provided by adding an identical rectifier bank to the existing power supply. An optimum magnet configuration could then be matched to the modified power supply and the total cost of the system would be less than modifying the existing coils and building a new power supply.

The existing 20-MW rectifier substation (Fig. 10) is matched to the secondary side of a 31-MVA load tap changing transformer (33 steps). The d-c operating characteristics of the transformer operating with solid-state diode rectifiers is shown in Fig. 34. Operating

<div align="center">

24

</div>

on the Tap No. 33 characteristic the open circuit voltage is 2800 v, and 27 MW is possible at 16,000 amp. The existing rectifier is designed for a maximum current of 8000 amp at 2500 v, and by adding an identical rectifier in parallel (Fig. 35) a maximum d-c output of 27 MW at 16,000 amp can be obtained.

A photograph and as-built drawing of the existing rectifier bank are shown in Figs. 36 and 37. Six rectifier stacks mounted between the incoming a-c and outgoing d-c bus bars are all enclosed within a steel cabinet. Each stack consists of four parallel sets of four silicon hockey-puck rectifier cells in series, each mounted betwen water-cooled heat sinks. Each cell (approximately 5.4 cm in diameter and 2.54 cm thick) is rated at 2000 v (peak inverse, repetitive) and 720 amp, providing a stack rating of 2700 amp and 2500 v at 125°C maximum case temperature. Demineralized water at 6.65 atm (100 psi) is used for cooling the stacks which are maintained well within the specified temperature operating range. Heat generated within the enclosure is removed by a fan-driven filtered air system. Resistor voltage dividers and resistor-capacitor surge networks provide protection for the rectifier cells. The a-c input line is monitored by three current transformers and the d-c output by a current transductor and voltage divider network.

The addition of a rectifier to the power supply will cost $67,600 (the value of the power supply is about $540,000) which is considerably below the estimated cost for a new power supply. This provides a cost advantage to building new coils matched to the modified power supply, and the magnet design study is directed toward providing an optimum magnet configuration.

5.2   MAGNET ANALYSIS AND DESIGN

In order to provide the highest magnetic field with the available power the magnet coil and poles should be as close as possible to the channel. This makes maximum use of the magneto-motive force (ampere-turns, NI) and minimizes the aperture volume over which the field is produced. The minimum volume assures a minimum inductance which, in turn, minimizes the rise time to a given current and the energy and heating of the magnet. These conditions maximize the magnetic field that can be produced with a given power supply.

A simplified schematic of the magnet cross section is shown in Fig. 38. The aperture is square ($h_g = w_p$) and is a function of x. The magnet pole extends from $x = \ell_p/2$ to $x = +\ell_p/2$. The value of w_p at $x = -\ell_p/2$ is referred to as w_{inlet} and the value at $x = +\ell_p/2$ is w_{outlet}. The winding cross section is $b_1 \times 2h_c$ independent of x and 2.54 cm (1 in.) is provided around the winding for insulation. Then $b_2 = b_1 - 5.08$ cm and $h_3 = 2h_c + 5.08$ cm are also independent of x. For the performance demonstration the magnet poles will be 7.1 m long with an inlet aperture of 0.71 m x 0.71 m and an exit aperture of 1.17 m x 1.17 m.

A complete magnetization curve (relating magnetic field strength to magnet current) from zero current up to the highest current is required in order to solve the transient response of a pulsed magnet. Since the major interest for the performance demonstration

25

magnet is in the high field region of the magnetization curve, it is possible to make simplifying approximations to the curve shape. In particular it is assumed that the curve has a break at the iron "saturation" value of magnetic field, B_s, and corresponding current, I_s. At a given point in the magnet bore the magnetization curve is taken to be

$$B = \mu_o NIh_g \quad \text{for } B \leq B_s \tag{25}$$

and

$$B = B_o + cNI = B_s + cN(I - I_s) \quad \text{for } B \geq B_s \tag{26}$$

From Eqs. (25) and (26), it is easily seen that the saturation current is given by

$$I_s = h_g B_s / \mu_o N \tag{27}$$

and

$$B_o = B_s - cNI_s \tag{28}$$

The term cNI is the direct coil contribution and for a given winding geometry c is independent of N and I.

The term B_o is the iron dipole contribution and its value depends on the design of the steel return frame. With the proposed steel return frame design, nearly all the steel saturates within a rather small range of current, but it is possible to add larger amounts of steel and obtain higher values of B_o at higher currents. The optimum amount of steel (minimum system cost) can only be determined by detailed calculations which are beyond the scope of the present effort. However, previous experience has shown that the cost curve has a broad minimum and that the approximations utilized within this analysis result in a design near the minimum and only slightly conservative. For the present analysis the steel is assumed to saturate at 1.98 T, and the saturation current is determined from Eq. (27).

The magnetization curves for several coils with different values of b_1 are shown in Fig. 39. The values of B obtained from Eqs. (25) and (26) have been multiplied by suitable correction factors to allow for fringing near the ends of the magnet. Based on previous experience with magnets of this type, correction factors of 0.50 at $x = \pm \ell_p/2$ and 0.95 at $x = -\ell_p/2 + w_{inlet}$ and at $x = \ell_p/2 - w_{outlet}$ are used to determine the magnetization curve.

The basic geometry and magnetization curves are thus established for the high performance demonstration magnet. It is now possible to optimize the coil-power supply system to provide the maximum magnetic field. The best system is determined by investigating the thermal-electrical response of many different configurations (i.e., different b_1, N, λ, and material) to determine the configuration which matches the power supply and produces the necessary ampere-turns at the lowest cost.

Precooling the magnet to 77°K (LN$_2$) decreases the electrical resistance, but the specific heat capacity is also reduced. The temperature and resistance can therefore increase markedly during a pulse and limit the advantage of precooling since the maximum field is determined by the coil resistance at the time of peak current. The current-temperature response of a pulsed coil can be determined by solving the following set of differential equations (Ref. 12):

$$V = L \frac{dI}{dt} + I[R_c + R] \tag{29}$$

$$\frac{dT}{dt} = \frac{I^2 R}{\rho_c V_c c_p} \tag{30}$$

where V is the voltage of the power supply, L is the inductance of the circuit, R_c is the resistance of the external bus work, R is the coil resistance, ρ_c is the density of the conductor, and V_c is the coil volume. The resistance of the coil, R, and $R/\rho_c V_c c_p$ are related to the temperature by

$$R = R_0[1 + \alpha_0(T - 77°K)] \tag{31}$$

$$\frac{R}{\rho_c V_c c_p} = c_0[1 - \beta_0(T - 77°K)] \tag{32}$$

where (in per °K) $\alpha_0 = 0.028$ and $\beta_0 = 0.0083$ for aluminum, and $\alpha_0 = 0.030$ and $\beta_0 = 0.012$ for copper. The quantities R_0 and c_0 depend on the geometry, material, and space factor.

The two variables which remain to be defined are the coil inductance L and the power supply voltage characteristic. The power supply characteristics for several different transformer tap settings are shown in Fig. 34. A continuous duty magnet system would probably optimize about the lower impedance level, 25-ka, 25-MW point (tap 9 or tap 13), since the magnet would have fewer turns and lower voltage and the resulting cost advantage would more than offset the slight reduction in power. However, for a pulsed magnet system, the higher power available at low currents (tap 33) allows the magnet to be charged faster, minimizing the temperature rise and producing a higher magnetic field. There is also a small savings in cost of the bus work at the lower current and less cost in upgrading the power supply. The voltage-ampere characteristic is taken to be a linear approximation to the tap 33 curve as shown in Fig. 40. It is assumed that the power supply will not be operated beyond the maximum power point at 16 ka. The resulting approximation for the voltage characteristic at the magnet (including bus resistance $R_c = 0.0052$ ohm) is

$$V = V_{oc} - IR_{ext} \tag{33}$$

where the open circuit voltage is $V_{oc} = 2800$ v and the total external resistance is $R_{ext} = 0.074$ ohm.

27

The inductance of the coil is expressed in terms of the coil geometry at $x = 0$ (Fig. 41) and the magnet pole length ℓ_p. Simplified expressions for the magnet induction (ignoring minor corrections for coil taper) are given in Table V. These simplified formulae are derived assuming that all the magnetic flux links all the turns and, hence, slightly overestimate the inductance.

A computer code was written to solve the differential Eqs. (29) and (30) utilizing Eq. (31) and the inductance equations from Table V. An extensive parametric study was conducted to determine the coils which match the power supply and provide the required magnetic field. The thermal-electrical response of an aluminum coil is shown in Fig. 42 and the response of a small ($b_1 = 14$ in.) copper coil is shown in Fig. 43. Either of these coils will meet the specifications for the experiment by providing a 6-T (or higher) field for 15 sec or more. The field characteristics are essentially identical to what would be expected from a properly designed, continuous, superconducting magnet having the same aperture. Thus MHD performance can be safely extrapolated to long-duration systems.

The magnet design analysis is directed toward providing the required magnetic field at a minimum cost by considering many coils (characterized by the dimension b_1) with different space factors (λ) using both aluminum and copper. A final analysis would also optimize the amount of steel used with each coil. However, this would involve tedious calculations, and the savings do not justify this effort at the present time. A single criterion which will yield a nearly optimized system has been used to determine the steel return frame for each coil.

Figure 44 shows the variation of cost with magnetic field as the coil build (b_1) is increased at a constant space factor. The 0.5 space factor is a conservative value which can be obtained easily. The dotted lines in Fig. 44 (and later in Figs. 45 and 46) indicate a change from aluminum to copper without changing the coil geometry or space factor. It should be noted that beyond a certain magnetic field the solid curves become very steep, and increasing the magnetic field by increasing the coil size is expensive. When the dotted curve has a smaller slope than the solid curve, it is less expensive to increase the field by going from aluminum to copper than by increasing the size of the aluminum coil.

The solid curves in Fig. 45 show the cost increases associated with increasing the magnetic field by increasing the space factor at constant coil build. Note that the slope of the solid curves is relatively low, especially for aluminum. As the space factor becomes higher, however, the coil becomes more difficult to cool and to electrically insulate. The cost estimates do not take this into account, and it is assumed that the space factor can be increased to 0.85 without a severe cost penalty. Extrapolating these curves beyond 0.85 would underestimate the cost.

Starting with a 26-in. build aluminum coil and assuming it is desired to increase the magnetic field, the obvious choice is to increase the space factor. Once the maximum practical space factor is reached, it is more economical to switch to copper (dotted line) than to increase the coil build in aluminum (dashed line).

Figure 46 presents design data for a 0.85 space factor. It is apparent that at 6 T either copper or aluminum could be used. At the same cost and performance, where the two curves intersect, the copper coil is considerably smaller than the aluminum coil. This offers certain advantages (conveniences) not taken into account by the cost equations. At higher fields copper is definitely superior to aluminum.

A pictorial representation of the windings and steel is shown in Fig. 47 for the copper coil. The total magnet weight is 560 metric tons (1,232,000 lb). It should be noted that the thickness of the existing steel is more than adequate over the length available, and new steel will have to be added only on the upstream end of the magnet. The windings will be either hollow conductors or plates. If a hollow conductor is used, a single vacuum wall nitrogen cryostat will be required, whereas if plates are used a double-wall nitrogen cryostat will be required. A schematic of a double-wall cryostat, coil, and coil supports is shown in Fig. 48.

The initial cooldown from room temperature will require 28,600 liters of LN_2 (at 3 cents per liter) and cooldown time will be approximately 20 hr. Cooldown between successive pulses will require approximately 3900 liters of LN_2 and the steady-state loss will be approximately 100 liters per hour.

The load-bearing insulation is designed such that the heat leak under the vacuum load is relatively low. The bearing pressure under magnetic load is, however, 100 times greater than the atmospheric pressure. During the magnet field pulse the load-bearing insulation will deflect a small amount, allowing the magnetic loads to be supported by higher strength members. The additional heat leak introduced by these higher strength members during the pulse will be negligible compared to the joule heating in the coil winding. Similar load-bearing members can be placed in the vacuum wall between the channel region and the coil in the event that the electromagnetic transient induced during the MHD plulse should "leak" through the MHD channel and induce currents and, hence, magnetic forces in the vacuum walls.

In summary, this preliminary analysis has shown that either an aluminum or a copper coil (LN_2 cooled) driven by a modified power supply can provide the magnetic field for the demonstration experiment. A copper coil would be slightly smaller, and an aluminum coil would have a flatter magnetic field time response curve. In addition to providing the magnetic field for the demonstration experiment, this large LN_2-cooled magnet can also be considered as a first step toward a superconducting magnet of comparable size. The LN_2-cooled magnet will have a current density on the order of 2000 amp/cm^2 with about 240 MJ of energy stored in the magnetic field, which are expected in a comparable superconducting magnet. Also, the fringe fields encountered with this LN_2-cooled magnet will provide an opportunity to study the external force interactions which will have to be handled when a superconducting magnet is operated within an MHD system.

SECTION VI
OTHER SYSTEM COMPONENTS AND INSTRUMENTATION

The existing rocket-type burner used in the LORHO generator program will be used as the hot gas source for the high perfomance demonstration experiment. The backplate was burned through during the last firing of the LORHO Facility in 1969 and this will be replaced. A redesign of the plate has been completed (Fig. 49), improving the cooling and alleviating the inherent difficulties present in the former design. The material for the plate (beryllium copper) has been purchased and machining and fabrication can start immediately. Also, the burner volume will be doubled by adding a circular spool downstream of the existing burner. This will assure sufficient residence time to have complete combustion and compensate for the slightly increased N_2/O_2 ratio over that previously used. The dummy channel available from the LORHO program will be used to check out the burner.

The burner is of circular cross section and the generator channel is square. A converging nozzle will serve as a transition piece from the circular burner to the square channel. The nozzle will be designed to provide the required entrance conditions of 2800°K, P = 5.0 atm at M = 0.7 when the burner is operating at 6.75 atm. A square subsonic diffuser which will allow for recovery to atmosphere will be installed. It will be water cooled and electrically insulated from ground. The exhaust from the diffuser will enter the existing 10-ft-diam breech where a system of spray nozzles will quench and clean the exhaust. Experience with LORHO indicates that the final exhaust products will mostly be steam and will not contain any significant amount of seed. A layout of the system together with sections of the nozzle, diffuser, and burner extension is shown in Fig. 50.

Toluene (C_7H_8) with oxygen-enriched air (N_2/O_2 = 1.25) will be used for the performance demonstration. The fuel and oxidizer storage and feed systems are described in Section II and will require no modification for the demonstration. It should be noted that toluene has a C-H ratio near that of coal and, hence, should provide good simulation of a coal-burning system. Potassium hydroxide (KOH) dissolved in methanol will be used as the seeding material; cesium can be used if necessary. The seed system is existing and will not require any major modifications.

The instrumentation, controls, and data acquisition equipment existing in the LORHO Facility are described in Section II. The equipment is designed specifically for large MHD generators and, with minor modifications, is well suited to the demonstration experiment. The distinguishing feature of the instrumentation of a large MHD channel is the requirement to isolate the recording and monitoring instruments from the high d-c potential on the channel. The existing system has 100 channels of 3000-Hz frequency response and approximately 100 additional channels with a tape system will be added to provide a sufficient number of data acquisition channels. The data will be recorded on magnetic tape and reduced off-line using the PWT Raytheon 520 computer. All the controls, interlocks, and monitoring equipment are available in the existing control room for remote operation of the performance demonstration experiment.

The demonstration experiment will be instrumented to provide adequate information for comparison with theory and to improve design techniques. Most instrumentation can be used for system protection as well as a source of data. Measurements will be made, first of all, to establish channel entrance conditions. These measurements will include flow rates of the fuel, oxidizer, and seed, burner pressure, burner cooling water flow rate and temperature rise, nozzle cooling water flow rate and temperature rise, and channel flange cooling water flow rate and temperature rise. The channel axial and transverse pressure distribution will be measured, and also the wall temperature at selected points to provide an estimate of the heat-transfer rate. Pressure rakes will be installed at channel entrance and exit during some of the runs to verify flow uniformity. The power generated will be determined by measuring the current and voltage across the load, or loads when running as a Faraday generator. The transverse potential distribution will be measured utilizing the pegs. The peg-wall design provides the opportunity for detailed local measurements which would not be possible in a Hall or window frame configuration. The pegs can conveniently be used for temperature, pressure, and voltage measurements. The peg temperature at the channel entrance will be monitored separately to prevent overheating of the heat-sink channel.

SECTION VII
PROGRAM OUTLINE AND FACILITY GROWTH POTENTIAL

7.1 PHASE I

The purpose of this effort has been to develop design criteria, cost estimates, and schedules for the high performance demonstration experiment. Performance goals for the experiment are 20-percent energy extraction at a 60- to 70-percent turbine efficiency with a 6.75-atm pressure ratio. The AEDC will conduct the experiment with the support of MEA and MEPPSCO as subcontractors. The experiment will make maximum utilization of the equipment (representing a $4.6 million investment) existing in the LORHO Facility located at AEDC. A brief outline of the system modifications and additions required for the demonstration experiment follows.

During Phase I of the program the high performance MHD generator channel design will be finalized, and the channel will be fabricated and installed in the LORHO Facility. The channel will be of peg-wall construction with segmented electrodes suitable for Faraday operation or external diagonalization. A converging nozzle which provides transition from the round burner cross section to the square channel inlet will be designed, fabricated, and installed. A square subsonic diffuser allowing recovery to atmosphere will be designed and installed at the generator exit. The exhaust gases will be quenched and cleaned by water spray and expelled to atmosphere through the existing breech system.

The LORHO magnet will be completely redesigned to provide on a pulsed basis a field of at least 6 T at the inlet end of the channel, decreasing to 5 T at the exit. Additional steel will be added to the pole pieces and a new LN_2-cooled coil will be designed, fabricated, and installed. An additional rectifier bank will be added to the existing power supply

31

to increase the power capacity to 27 MW at 1700 v and 16,000 amp. The magnet modification represents the largest single item in the cost estimate.

In addition to the major new equipment which will be added to the LORHO Facility for the demonstration experiment, all of the main systems (fuel, oxidizer, seed, and cooling water) will be renovated and reconditioned to assure reliable operation after three years of disuse. The redesigned backplate will be fabricated and installed on the burner and an extension added to double the burner volume. The existing instrumentation and controls will be reconditioned, and additional instrumentation and data acquisition equipment will be installed to assure complete and accurate documentation of the experiment results.

After the major hardware has been installed, some effort will be required for shakedown and calibration. A dummy nozzle and channel will be installed to check the timing, sequencing, and operation of support systems. A pressure rake will be installed at the nozzle exit to determine the pressure profiles and, hence, provide some indication of the flow entering the generator. Upon completion of the initial checkout operations of the system, the generator channel will be installed.

The generator will initially be electrically connected in a Faraday configuration. A new resistor load bank will be installed to dissipate the power from the 400 electrode pairs. Low power and short-duration runs will be made initially to check out system sequencing, seeding, magnet operation, and the generator channel. When the overall integrity of the channel and systems is assured, higher power runs will be made. The channel will be pushed to the limit to obtain the maximum power output. During these runs, channel pressure distributions, wall temperatures, channel exit flow pressure profiles, voltage and current for individual electrode pairs, and other measurements considered useful will be made to document accurately the results of the experiment. Comparison of the experimental results with theory will be made, followed by improvements in design calculation techniques.

When the maximum MHD performance attainable with the Faraday configuration has been demonstrated, the channel will be electrically connected in the slant-wall configuration. Operation in this mode will provide some insight into end losses and the problems associated with power takeoff in the slant-wall configuration. Detailed measurements of the performance will be made and compared with theory. The maximum power obtainable with this configuration will be demonstrated.

7.2 PHASE II

Because of the operational flexibility provided by the peg-wall construction, a maximum amount of information can be obtained with a single peg-wall channel to upgrade channel design techniques while also demonstrating generator performance. However, the peg-wall construction lacks the simplicity and ruggedness of the slant-wall window-frame construction. The base-load plant will probably use a window-frame-type channel provided the performance is not significantly less. Therefore, a channel of this type should be

investigated in the program. The performance of the externally connected diagonal channel will be similar to what can be expected from a window-frame slant-wall channel but not identical, since the electrical characteristics of the two channels are different. The electrodes of the window-frame channel contact the plasma around the entire channel perimeter rather than only on two walls, leading to different electrical characteristics (Refs. 13 and 14). In particular, a significant amount of current will be removed by the B-field walls at the ends of a window-frame channel when operating with a single circuit or with only a few grading resistors. It is proposed that, as a second phase to the demonstration experiment, a slant-wall, water-cooled, window-frame channel be designed, based on data obtained from the peg-wall channel and a test program conducted to demonstrate its performance. A preliminary cost estimate and schedule for this channel is included as a second phase to the performance demonstration. Operation of these two channels of different construction and of different electrical configurations will provide ample information on end losses, boundary-layer growth, and diffuser performance at a scale large enough to draw conclusions which are applicable to the base-load MHD generator.

7.3 FACILITY GROWTH POTENTIAL

After the performance of the window-frame channel has been established on a clean fuel, the natural extension is to investigate the effects of ash on the performance. A preliminary study has shown that ash can be injected into the existing burner and will require only a minor modification to the design of the burner backplate and the addition of an ash storage and injection system. Since these additions will cost only a few thousand dollars, ash injection capability can be obtained with only a small increase to the program cost estimate outlined in the next section.

The existing fuel-oxygen storage system has sufficient capacity to operate continuously for five minutes at the 60-kg/sec design flow rate. This would allow time for a slag layer to be deposited on the channel walls before the LN_2-cooled magnet is pulsed. A comparison of the generator characteristics operating with and without ash will provide an indication of the effects of ash on performance. The important thing to note is that the comparison would be in a large-scale generator which simulates the commercial device and is not dominated by electrode losses and boundary-layer effects as a small 1-kg/sec device would be.

It should be noted that the experience and performance data obtained from the performance demonstration experiment is directly applicable without any scaling to the 300-MW (thermal) MHD pilot plant proposed in OCR Report No. 71 (Ref. 1). In fact, it would be a logical extension to use the performance demonstration equipment as the basis for the progressive development of the MHD pilot plant. The facility developed for the demonstration experiment will have instrumentation, cooling water, and power which can be used for the MHD pilot plant. The pilot plant would require the addition of a coal combustor, superconducting magnet, exhaust treatment equipment, air preheater, and steam generator. More than adequate water is available for exhaust scrubbing, and the resulting effluent could be dumped into the existing AEDC settling pond before returning

to Woods Reservoir. The extension of the high performance demonstration facility into an MHD pilot plant would make maximum utilization of the hardware and of the design and operating experience gained during the experiment, and would provide a logical development program for the pilot plant. The extension of the high performance demonstration experiment into an MHD pilot plant is probably the most expedient way for developing such a pilot plant.

SECTION VIII
COST ESTIMATE AND TIME SCHEDULE

The cost estimate and project schedule is broken into two parts. The Phase I estimate and schedule covers the design, fabrication, and installation of the modified magnet and segmented-electrode peg-wall channel, and one year of operation. The Phase II estimate, which should be considered preliminary, covers the design, fabrication, and installation of a slant-wall, window-frame channel, and one year of operation. The Phase II window-frame design will start after the initial performance evaluation of the peg-wall channel and can proceed during Phase I operation.

Cost Estimate, Phase I

	Manhours	Manhour Costs	Material and Other	Total
System Renovation	21,000	$ 126,100	$ 74,300	$ 200,400
Burner Extension	1,300	9,300	8,500	17,800
Nozzle	2,600	19,000	20,000	39,000
Peg Wall Channel	2,000	14,000	254,300	268,300
Diffuser	12,800	90,200	8,300	98,500
Magnet			930,000	930,000
Power Supply	3,700	27,400	40,200	67,600
Resistor Bank	18,300	128,400	66,000	194,400
Instrumentation	4,600	35,500	38,500	74,000
Data Acquisition			160,000	160,000
System Shakedown	28,600	196,000	39,400	235,400
Operation	42,000	280,000	117,000	397,000
Engineering	11,900	104,600		104,600
Total Direct Cost	148,800	$1,030,500	$1,756,500	$2,787,000
Overhead		487,350	175,650	663,000
TOTAL COST	148,800	$1,517,850	$1,932,150	$3,450,000
Estimated Phase I Project Cost				$3,450,000

34

Cost Estimate, Phase II

Window-Frame Channel	2,000	16,000	292,000	308,000
System Modifications	13,200	101,000	20,000	121,000
Operation	42,000	323,000	110,000	433,000
Total Direct Cost	57,200	440,000	422,000	862,000
Overhead		206,800	42,200	249,000
TOTAL COST	57,200	$ 646,800	$ 464,200	$1,111,000
Estimated Phase II Project Cost				$1,111,000

Project Schedule, Phase I

MONTHS AFTER PROJECT APPROVAL

System Analysis
System Renovation
Dummy Nozzle and Channel
Burner Extension
Square Nozzle
Square Diffuser
Generator Channel I
Load Bank
Instrumentation & Data Acquisition
Power Supply
Magnet
System Checkout
Operation

PHASE II

MONTHS AFTER PROJECT APPROVAL

Generator Channel II
Test Cell Modification & Improvement
Operation

35
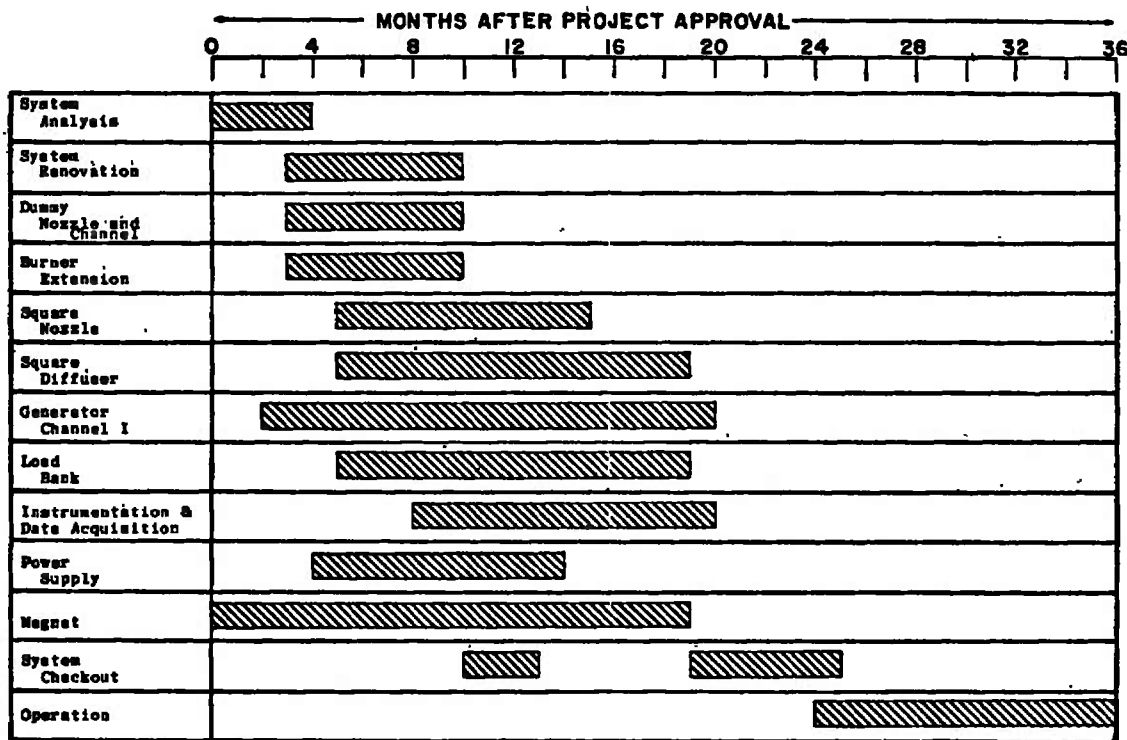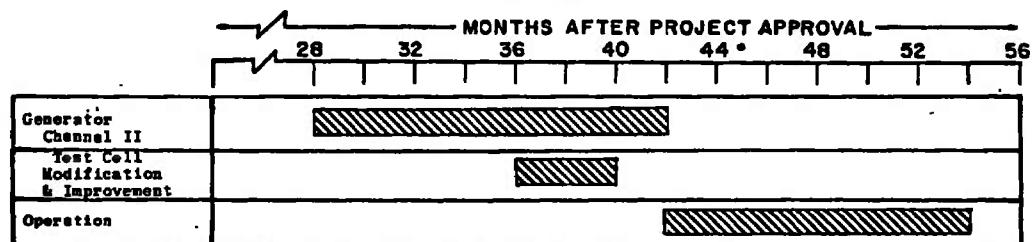
SECTION IX
SUMMARY AND CONCLUSIONS

The AEDC, in conjunction with subcontractors MEA, Inc. and MEPPSCO, Inc., has developed design criteria, cost estimates, and time schedules for the MHD performance demonstration. The study has shown that a definitive demonstration experiment can be conducted utilizing the existing LORHO Facility equipped with a modified magnet and a new MHD generator channel.

Four different sized experiments, involving various degrees of modification of the LORHO Facility, were considered in the AEDC study. One of these, based on a flow rate of 60 kg/sec, which is available with existing fuel, oxidizer, and seed systems, was selected on the basis of an optimum combination of cost effectiveness and significance of test results. This experiment will require lengthening and tapering the pole pieces of the LORHO magnet, installation of an entirely new cryogenically cooled coil, and addition of a 7-MW increment to the d-c power supply which powers the coil. A new high performance generator channel will be added having a length approximately 30 percent longer than the LORHO channel. Operational characteristics and predicted performance of the demonstration channel and a composite base-load unit are given in Table VI. As indicated, the demonstration will be performed with the channel operated as a Faraday channel and as a single-circuit, diagonally connected channel. The output of the diagonal generator is reduced because of a conservative design which minimizes unknown end losses at the expense of power output. In order to approach the 20-percent energy extraction ratio from the higher enthalpy working fluid, it is necessary to increase the combustion pressure from the base-load value of 5 atm to a value of 6.75 atm in the demonstration experiment. The energy extraction could be increased to 20 percent by using a combustion pressure of 8 atm, but the lower value was selected as a reasonable compromise for simulation of the operating parameters of the base-load plant. It should be noted that although the energy extraction ratio for the demonstration is slightly less than for the base-load plant, the specific energy extraction (electrical output per unit mass flow) is larger for the demonstration than for the base-load plant. As recommended in OCR Report No. 71 (Ref. 1) the turbine efficiency requirement has been relaxed to the range of 60 to 70 percent for the performance demonstration, recognizing the realities of simulation of the base-load generator.

A set of scaling laws were derived to relate the various size experiments to the full-scale commercial generator at 60 kg/sec. The demonstration experiment will be approximately a $1/\sqrt{10}$ scale of the base-load plant. The relative scale of several experiments in terms of Reynolds number is shown in Fig. 14. The demonstration experiment is the only generator existing or proposed, of sufficient size (Reynolds number within a factor of three of full scale) to allow confident scaling of viscous effects to the base-load plant. The experiment will achieve a reasonable simulation of the boundary layer and of the electrode loading of the full-scale generator, whereas an experiment performed at any significantly smaller scale would be dominated by viscous and electrode losses. The experience and performance data gained from this demonstration experiment will be

directly applicable without any scaling to the 300-MW (thermal) MHD pilot plant proposed in OCR Report No. 71 (Ref. 1).

REFERENCES

1. Louis, J.F., et al. MIT MHD Power Generation Study Group. "Open Cycle Coal Burning MHD Power Generation: An Assessment and a Plan for Action." Office of Coal Research R and D Report No. 71, 1972.

2. Tsu, T.C., Young, W.E. and Way, S. "Optimization Studies of MHD Steam Plants." Electricity from MHD, Vol. IV, IAEA and ENEA, Salzburg, July 1966, p. 899.

3. Dinelli, G. and Masses, J. "Influence de divers parameters sur le rendements des centralis MHD." Electricity from MHD, Vol. IV, IAEA and ENEA, Salzburg, July 1966, p. 899.

4. Hals, F., and Jackson, W. "System Analysis of Central Station MHD Power Plants." Proceedings of Fifth International Conference of MHD Electrical Power Generation, Vol. I, Munich, April 1971, p. 645.

5. More, Y. "Cycle and Efficiency of Large Scale Open Cycle MHD Power Plants." Proceedings of Fifth International Conference of MHD Electrical Power Generation, Vol. I, Munich, April 1971, p. 569.

6. Heywood, J.B., and Womach, G.J., editors. Open Cycle MHD Power Generation, Pergamon Press, 1969.

7. Louis, J.F., Lothrop, J.L., and Brogan, T.R. "Fluid Dynamic Studies with a Magnetodydrodynamic Generator." Physics of Fluids, 1, March 1964, p. 362.

8. Louis, J.F., Gal, G., and Blackburn, P.R. "Detailed Theoretical and Experimental Study of a Large MHD Generator." AIAA Journal, Vol. 3, No. 8, 1965.

9. Patrick, R.M. and Brogan, T.R. "One Dimensional Flow of an Ionized Gas in a Magnetic Field." J. Fluid Mech., Vol. 5, February 1959, p. 289.

10. Teno, J., Brogan, T.R., and Petty, S.W. "Research Studies and the Development of MHD Generators and Accelerators." AEDC-TR-70-14 (AD863990), January 1970.

11. Mattsson, A., Duchame, E., Govoni, E., Marrow, T., and Brogan, T.R. "Performance of a Self Excited Rocket Driven MHD Generator." Final Reports Contract AF33(615)-8380 (April 1964) and AF33(615)-1862 (May 1965). See also Mech. Eng., Nov. 1966.

12. Montgomery, D.B. <u>Solenoid Magnet Design.</u> Wiley-Interscience, New York, 1969.

13. Koester, J.K. and Nicholson, M.K. "Three-Dimensional Current Distribution and Electrode Configuration Effects in Diagonal Wall Generators." 12th Symposium Engineering Aspects of Magnetohydrodynamics, Argonne, Illinois, March 27-29, 1972, p. II, 6.1.

14. Eustis, R.H. and Kessler, R. "Measurement of Current Distributions and the Effect of Electrode Configuration on MHD Generator Performance." <u>Fifth International Conference on MHD Electrical Power Generation</u>, Vol. 1, Munich, April 19-23, 1971, p. 281.

15. Argyropoulos, G.S. and Casteel, M.A. "Tables of Interaction Parameters for Computation of Ohm's Law Coefficients in Various Gases." <u>Journal of Applied Physics,</u> Vol. 41, No. 10, September 1970, p. 4162.

16. Teno, J., Lin, C., and Brogan, T.R. "Boundary Layers in MHD Generators." <u>Proceedings of the 10th Symposium on the Engineering Aspects of MHD</u>, MIT, 1969.

17. Johnson, P.W. "Two-Dimensional Flow Calculations in the Magnetic Field Plane for Linear MHD Channels." AEDC-TR-71-20 (AD880611), February 1971.

APPENDIXES
I. ILLUSTRATIONS AND TABLES
II. CHANNEL DESIGN EQUATIONS
AND COMPUTER CODES
III. TWO-DIMENSIONAL FLOW-
FIELD CALCULATIONS
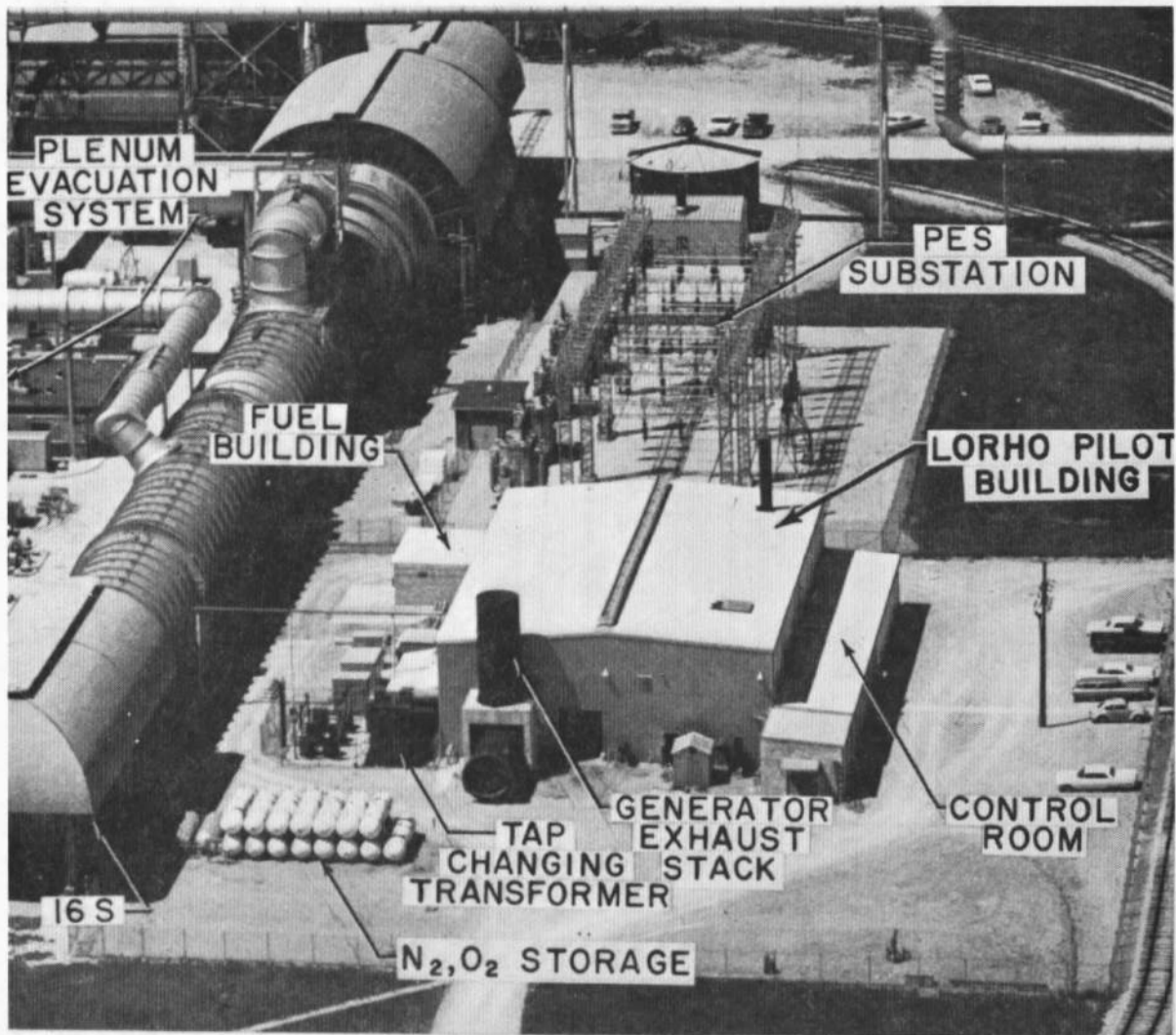
Fig. 1 Photograph of the LORHO Facility

41

O_2, N_2 STORAGE

GENERATOR EXHAUST STACK

RECTIFIER UNITS FOR MAGNETIC FIELDS

AC POWER SUBSTATION

MHD GENERATOR MAGNET

MHD GENERATOR CHANNEL

COMBUSTION CHAMBER

RESISTOR BANK

ARC HEATER

MHD ACCELERATOR CHANNEL

CONTROL ROOM

MHD ACCELERATOR MAGNET

FUEL BUILDING

REGENERATIVE HEATER TEST BED

HIGH PRESSURE ARC HEATER TEST BED

42
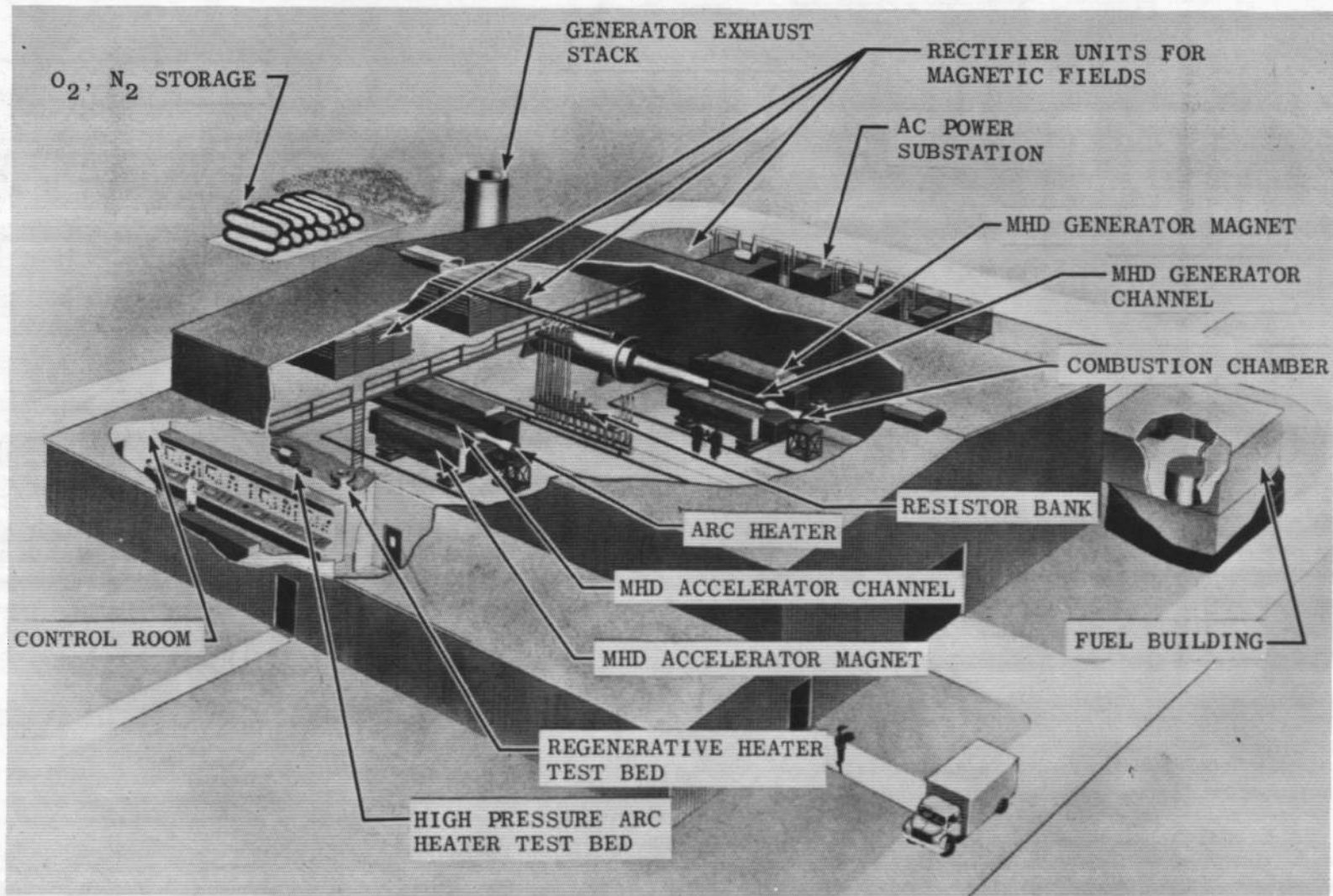
Fig. 2 Sketch of the LORHO Facility (PWT)
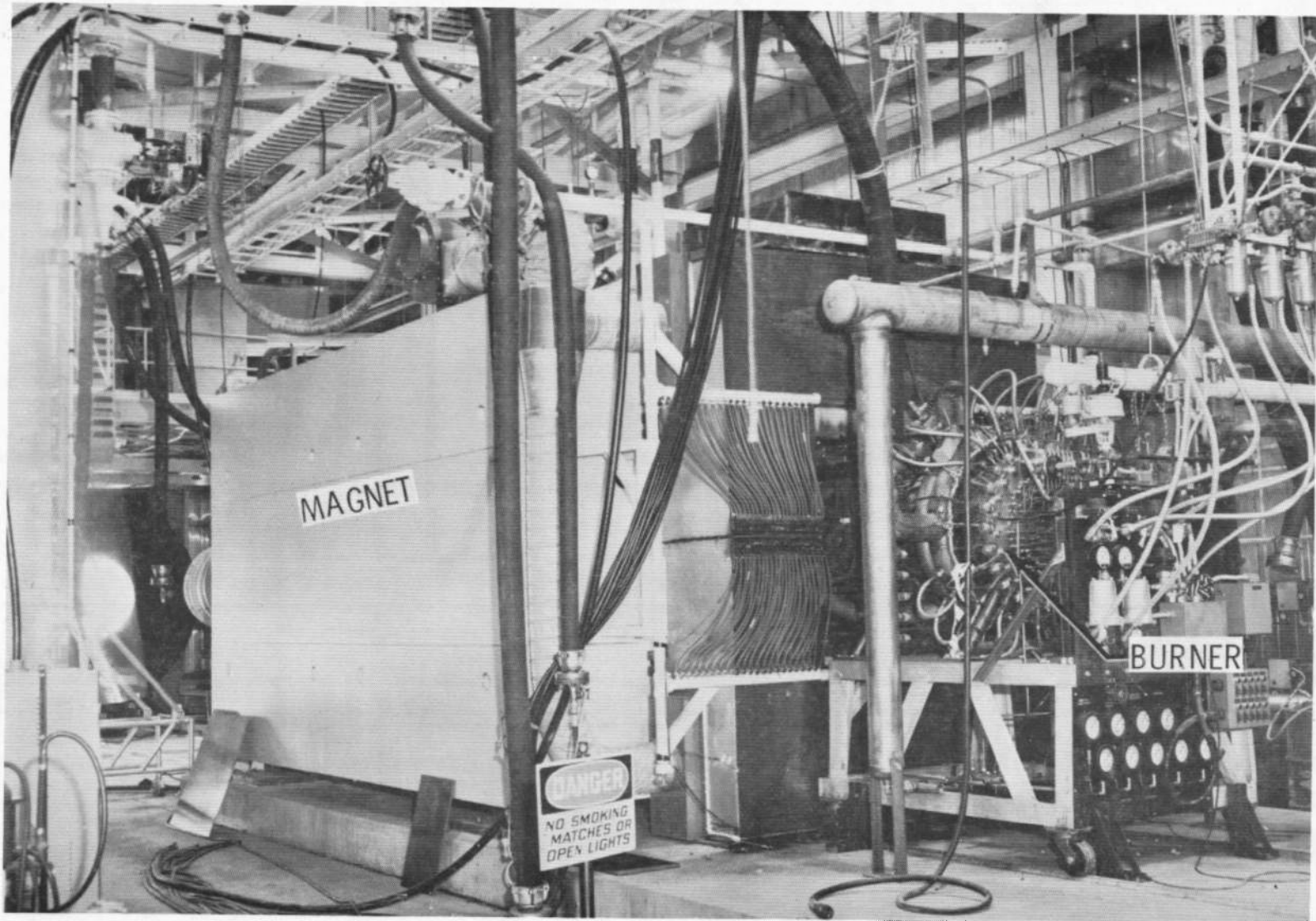
Fig. 3   LORHO Facility; Magnet and Burner

43
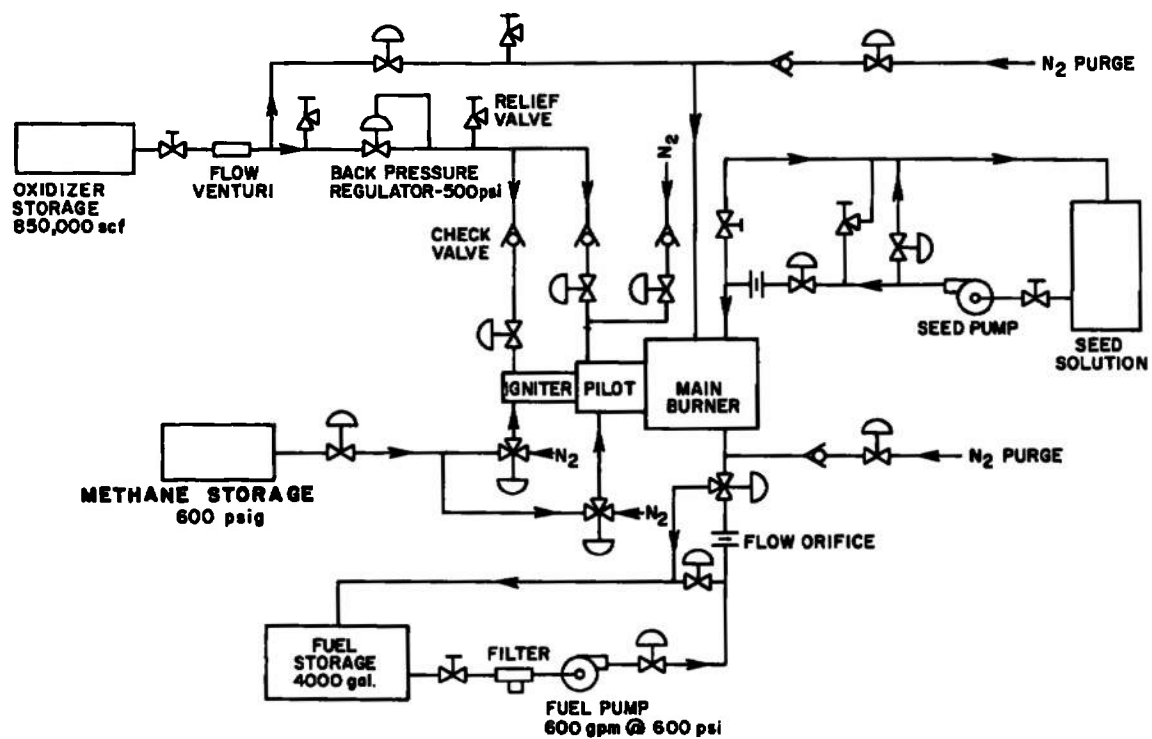
Fig. 4 Fuel, Oxidizer, and Seed Systems Schematic
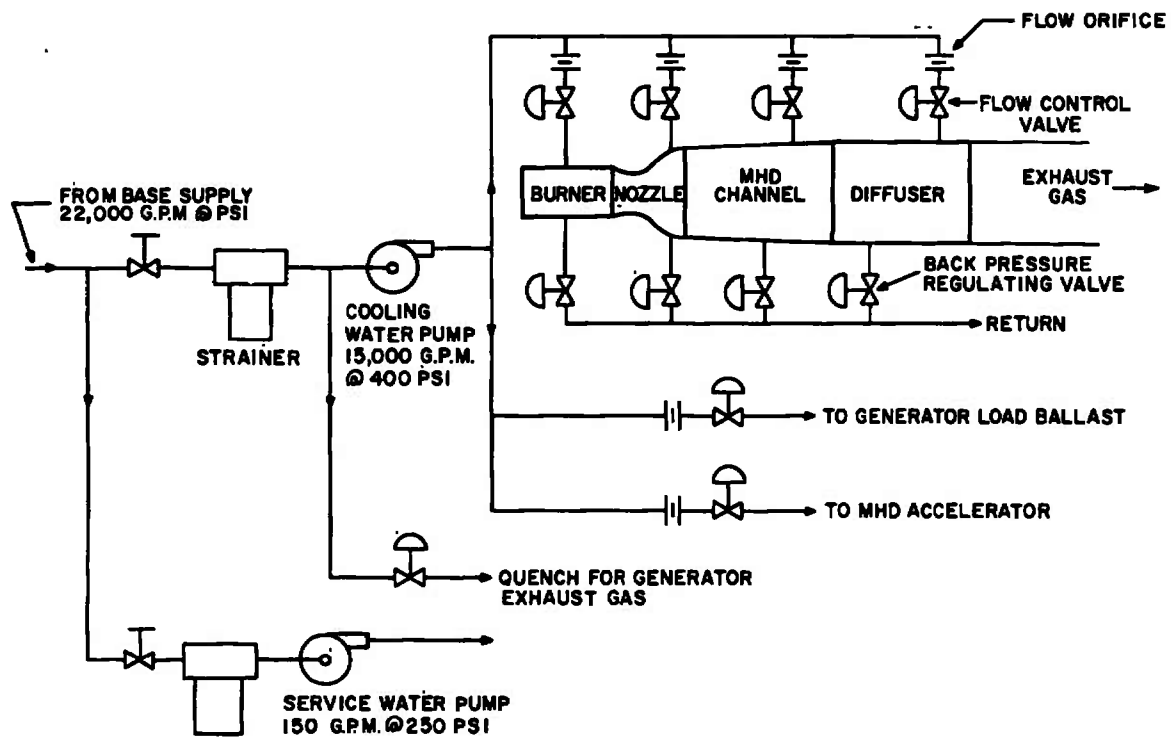
Fig. 5 Cooling Water Distribution Schematic

Labels within figure:

FLOW ORIFICE

FLOW CONTROL VALVE

EXHAUST GAS

FROM BASE SUPPLY 22,000 G.P.M @ PSI

BURNER NOZZLE

MHD CHANNEL

DIFFUSER

BACK PRESSURE REGULATING VALVE

RETURN

STRAINER

COOLING WATER PUMP 15,000 G.P.M. @ 400 PSI

TO GENERATOR LOAD BALLAST

TO MHD ACCELERATOR

QUENCH FOR GENERATOR EXHAUST GAS

SERVICE WATER PUMP 150 G.P.M. @ 250 PSI
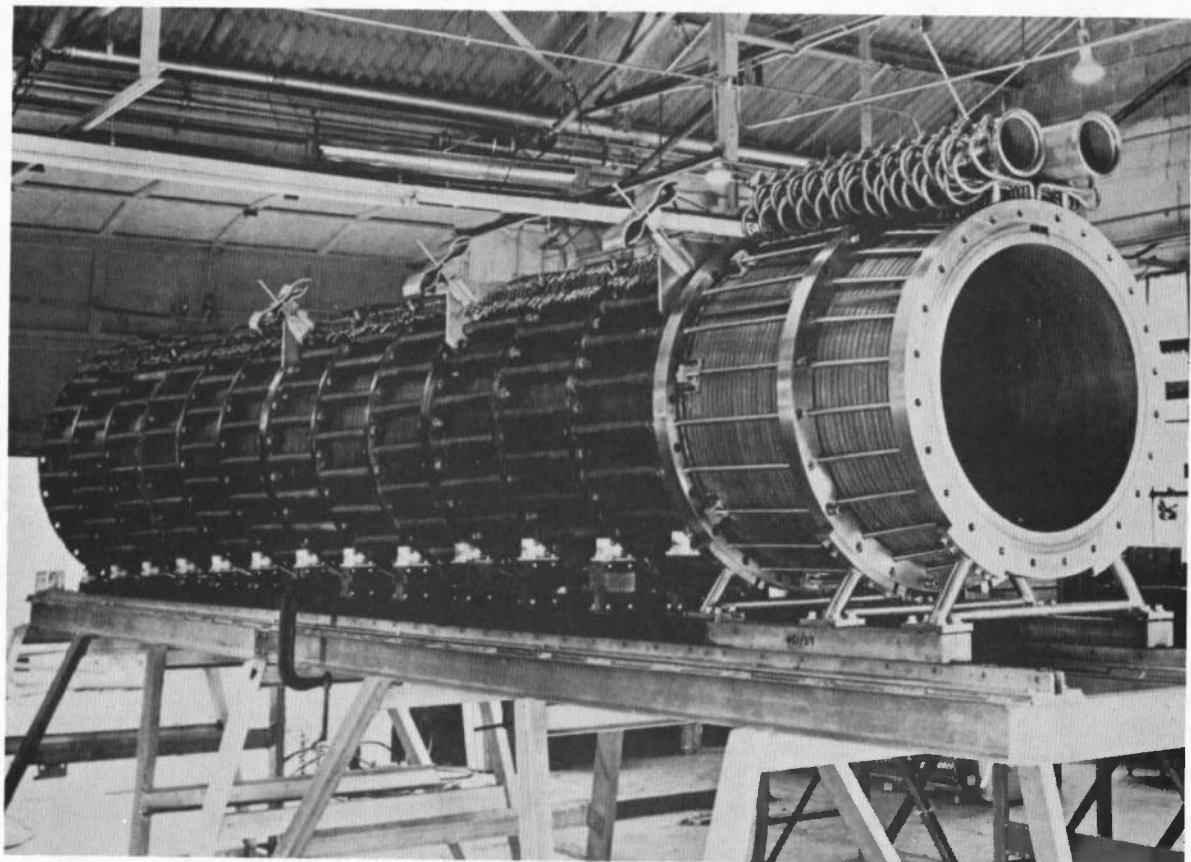
Fig. 6   LORHO Power Supply MHD Channel
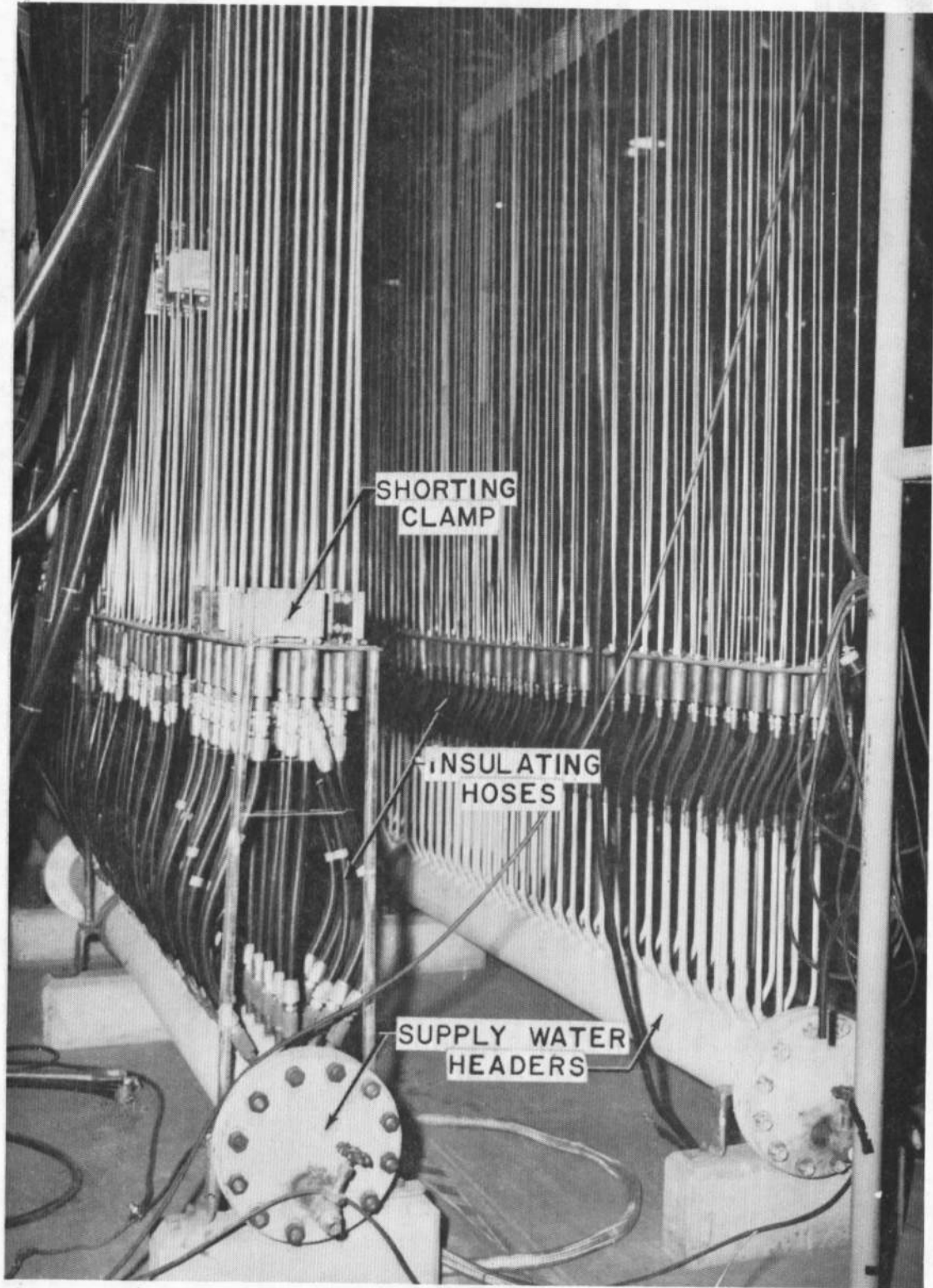
Fig. 7 Water-Cooled Resistor Bank
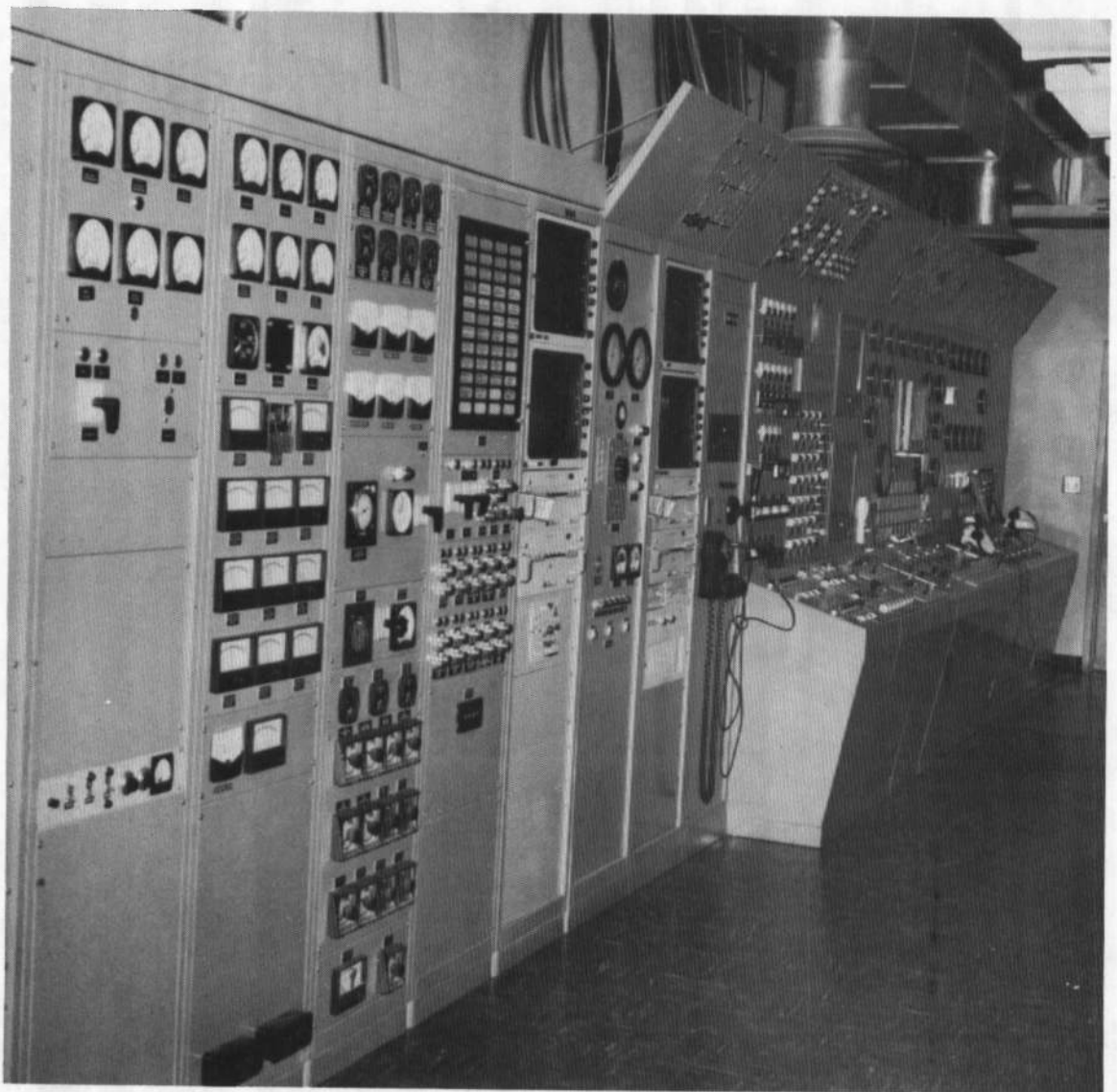
Fig. 8 Control Room, LORHO Facility
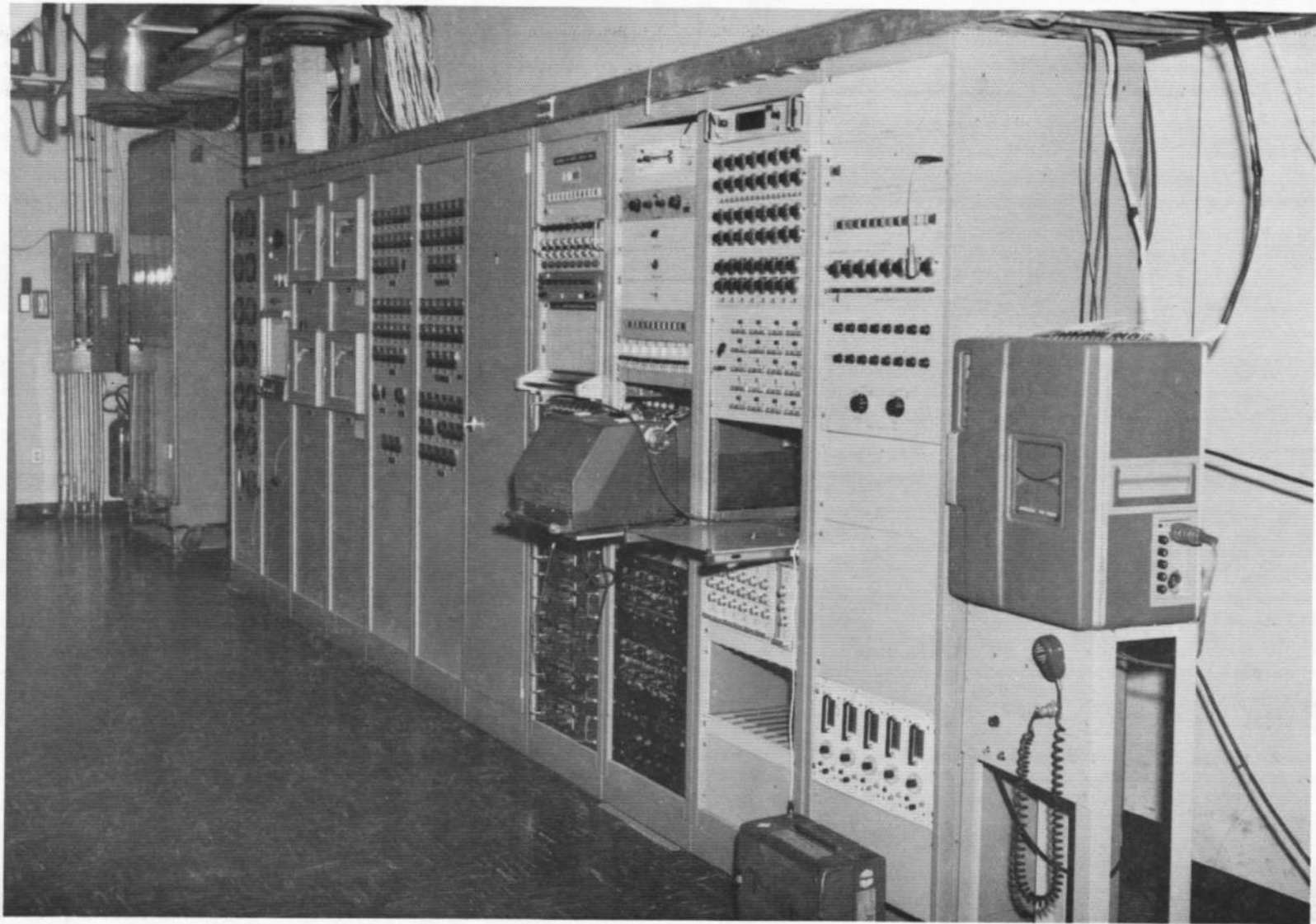
Fig. 9 Control Room, LORHO Facility

20 MW SYSTEM (EXISTING)

161 KV

PES TRANS # 4
WINDING # 2

13.8 KV

UG LINE

ACB 2EI

UG LINE

POLE TOP SWITCHES

REACTOR BANK
0-14 ohms

LOAD TAP CHANGING TRANSFORMER
1040 - 2080 VAC OUTPUT

CABLE DUCT

RECTIFIER SUBSTATION # 4
2500 VDC 8000 A

LOAD
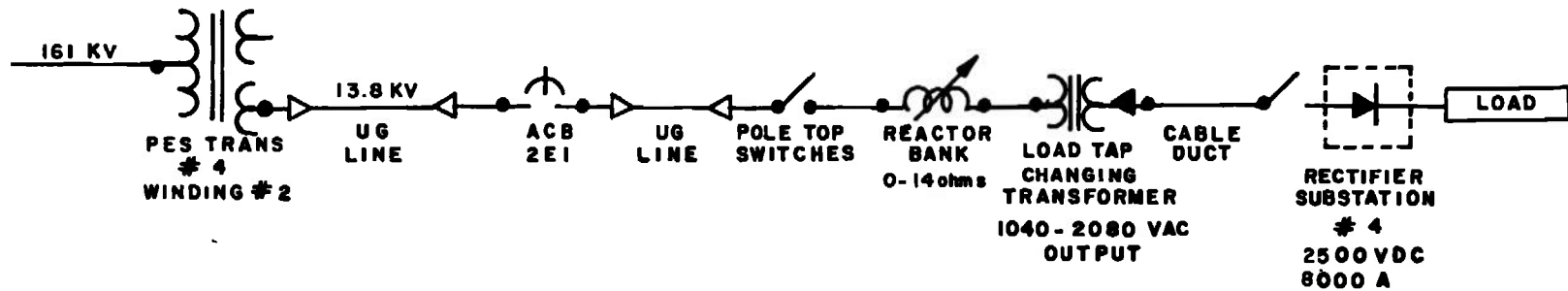
L.T.C. TRANSFORMER & RECTIFIER SUBSTATION SCHEMATIC

13.8 KV Pri.

1080 - 2040 VAC 3φ

CT

CT

TRANSDUCTOR (FOR DC CURRENT)

TO LOAD

20 MW RECTIFIER SUBSTATION (TYPICAL)
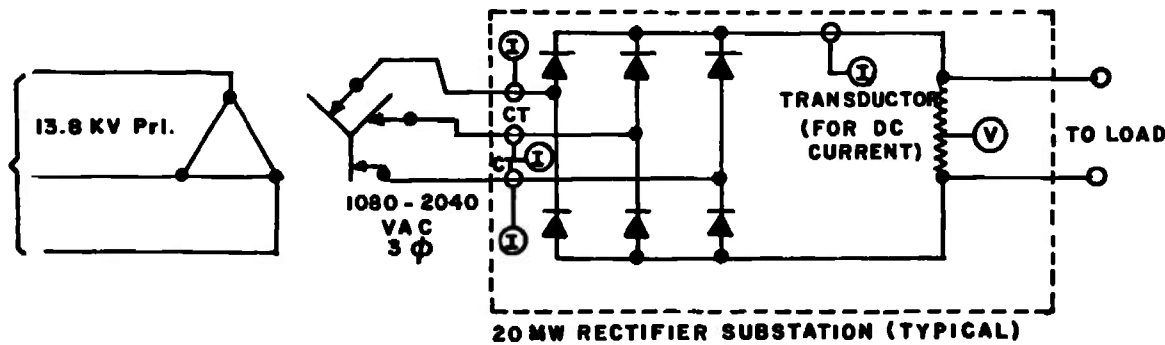
Fig. 10 Existing 20-MW Power Supply
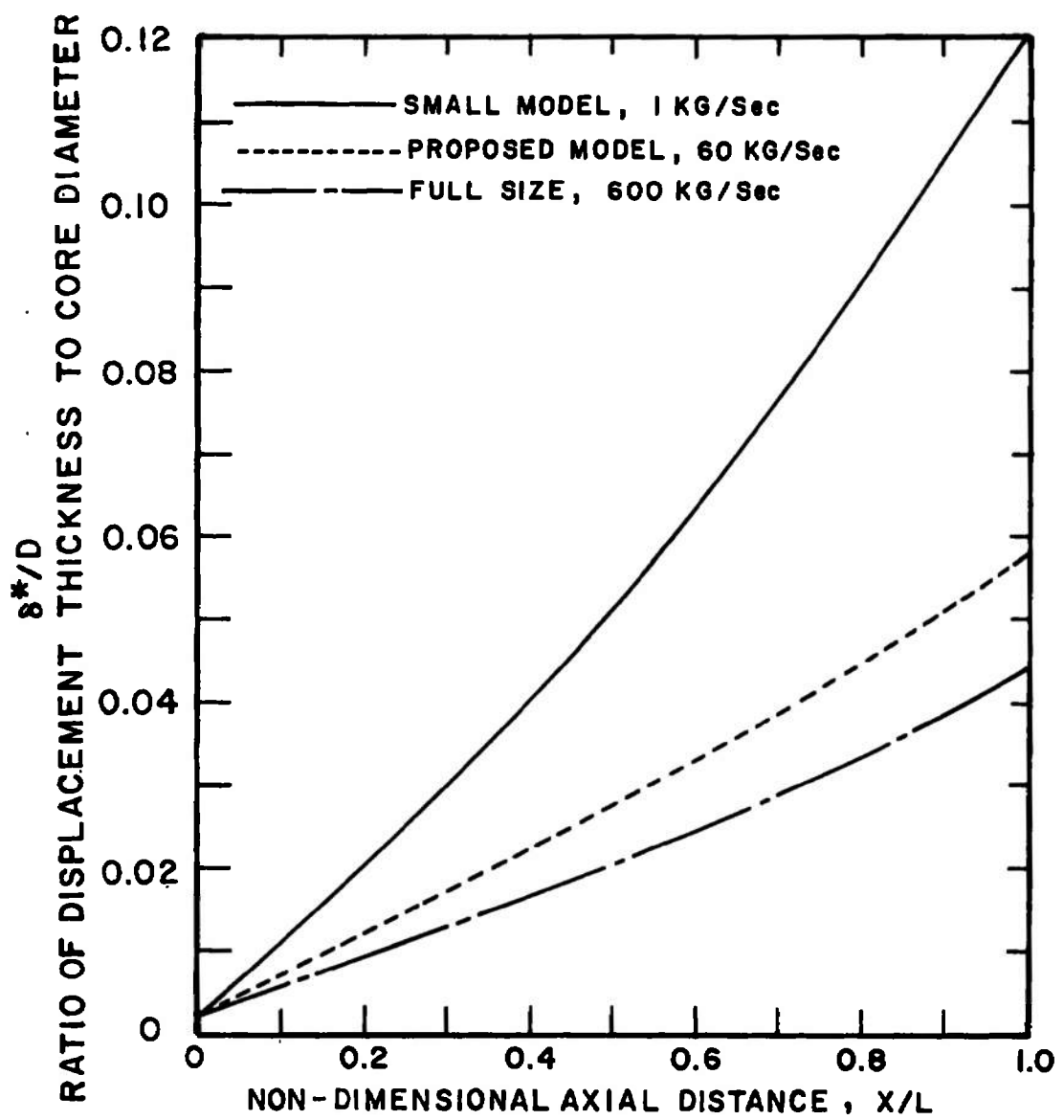
Fig. 11 Boundary-Layer Displacement Thickness for Similar Generators
of Different Mass Flow
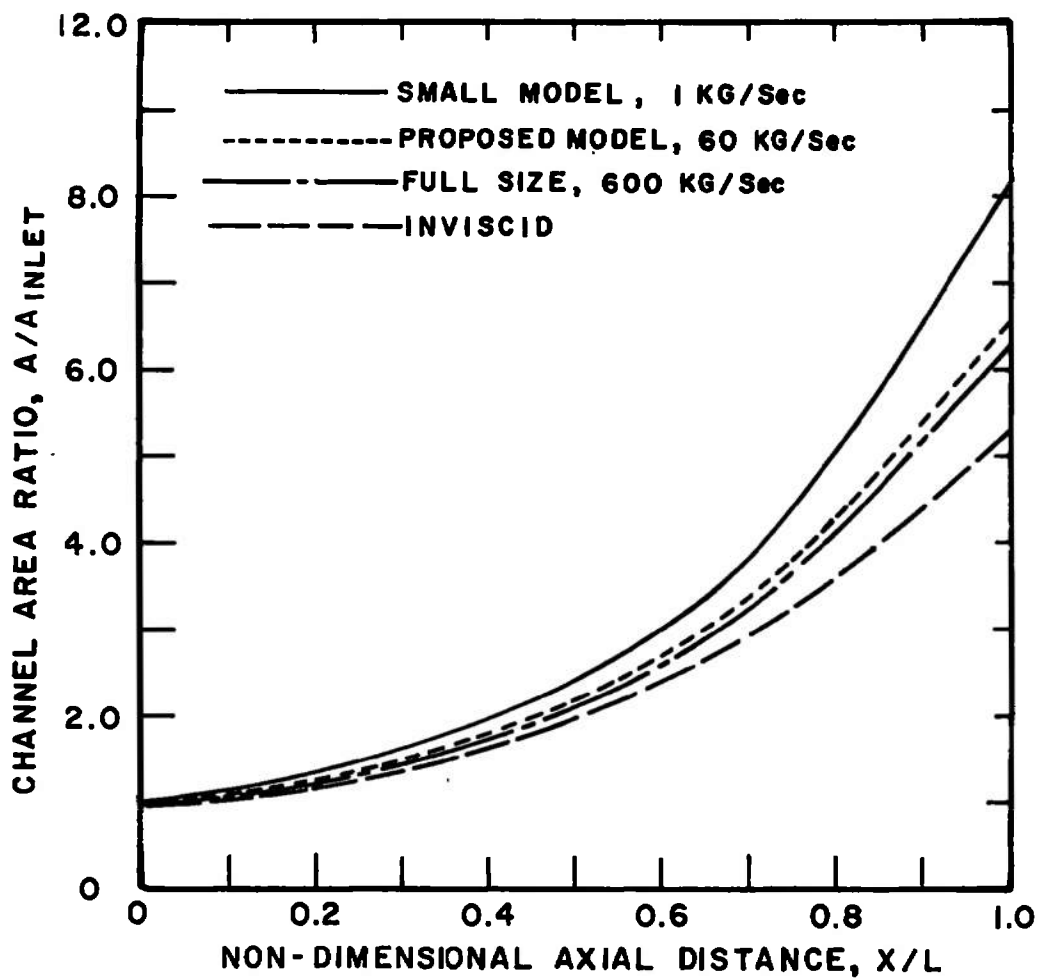
Fig. 12 Changes in Channel Loft for Similar Generators
of Different Mass Flow
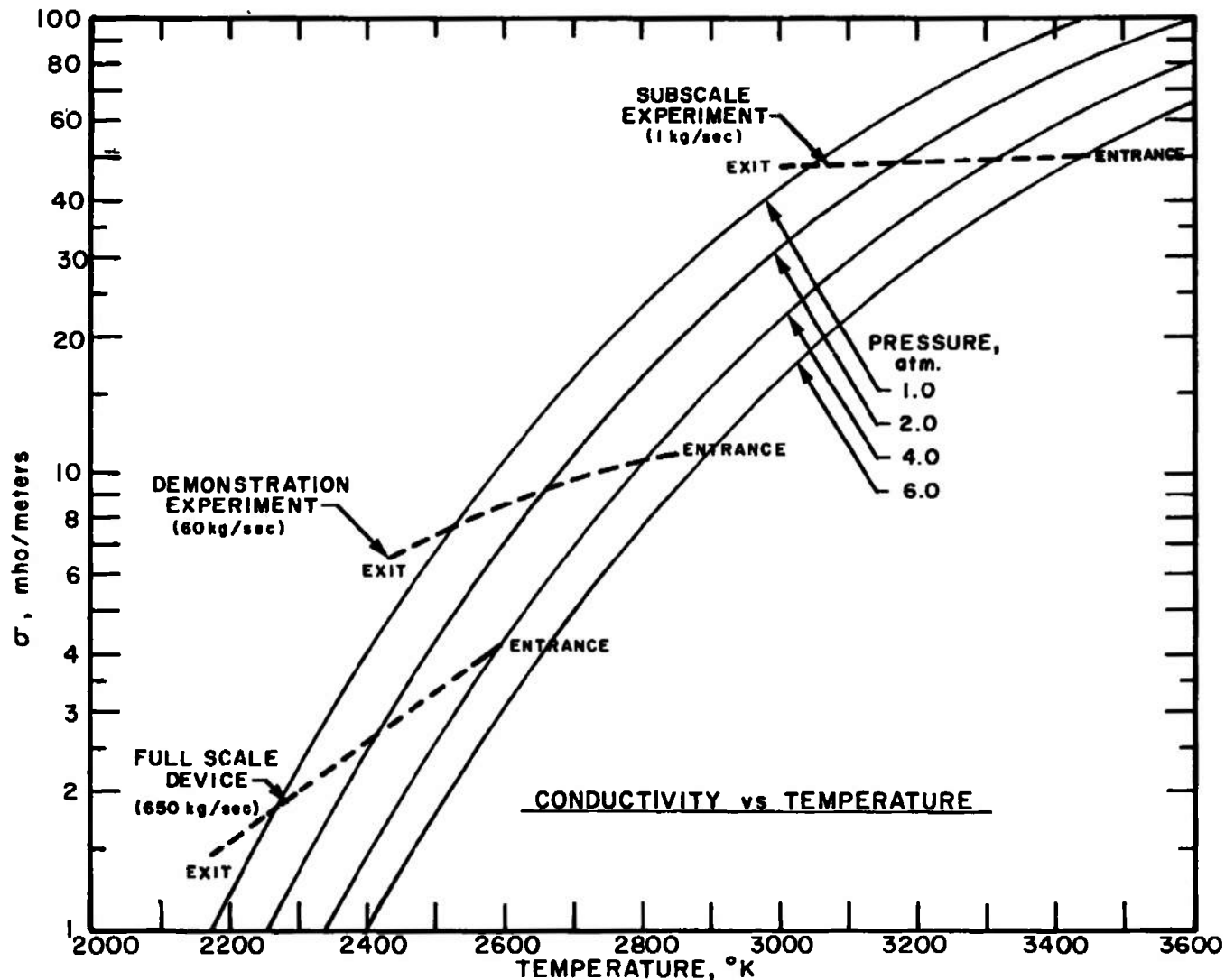
Fig. 13 Conductivity versus Temperature and Conductivity Variation Through Three Different Sized Generators
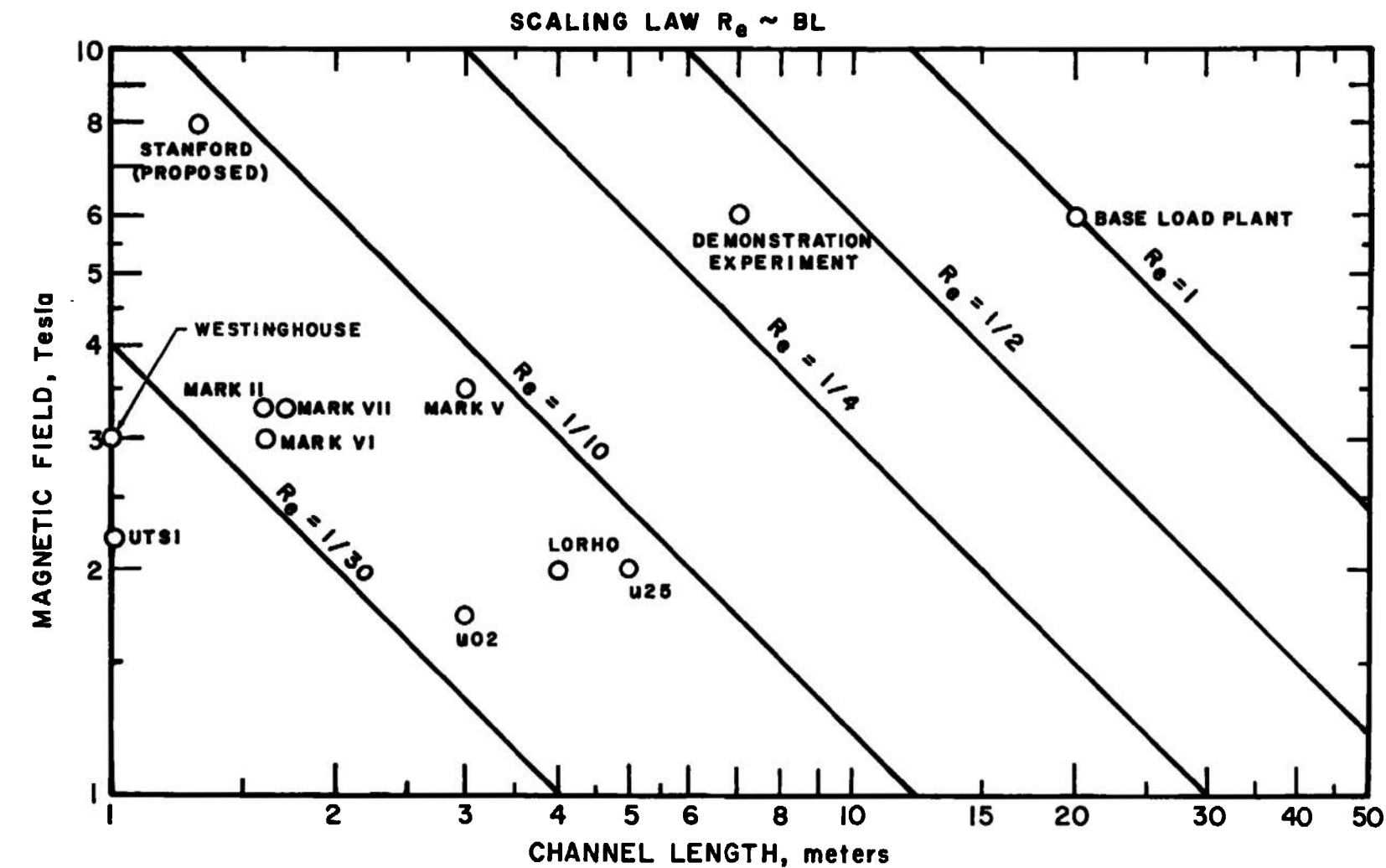
Fig. 14 Reynolds Number Scaling Characteristics and Relative Scale (B, L) of Several MHD Generators

GENERATOR CONFIGURATIONS

ELECTRODE SEGMENT

LOADS

SEGMENTED FARADAY

HALL GEOMETRY

LOAD

DIAGONAL CONNECTION

LOAD

TWO TERMINAL FARADAY
OR
CONTINUOUS ELECTRODE

LOAD
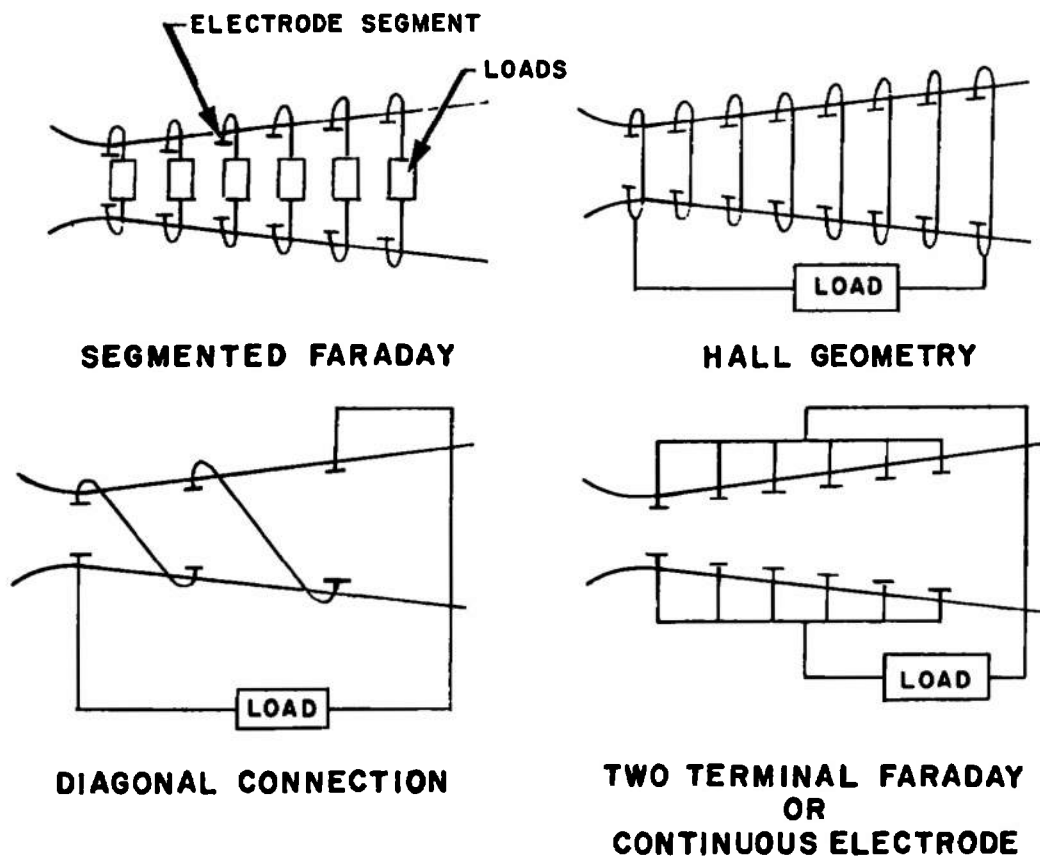
Fig. 15 Four Basic Configurations for a Segmented-Electrode MHD Generator
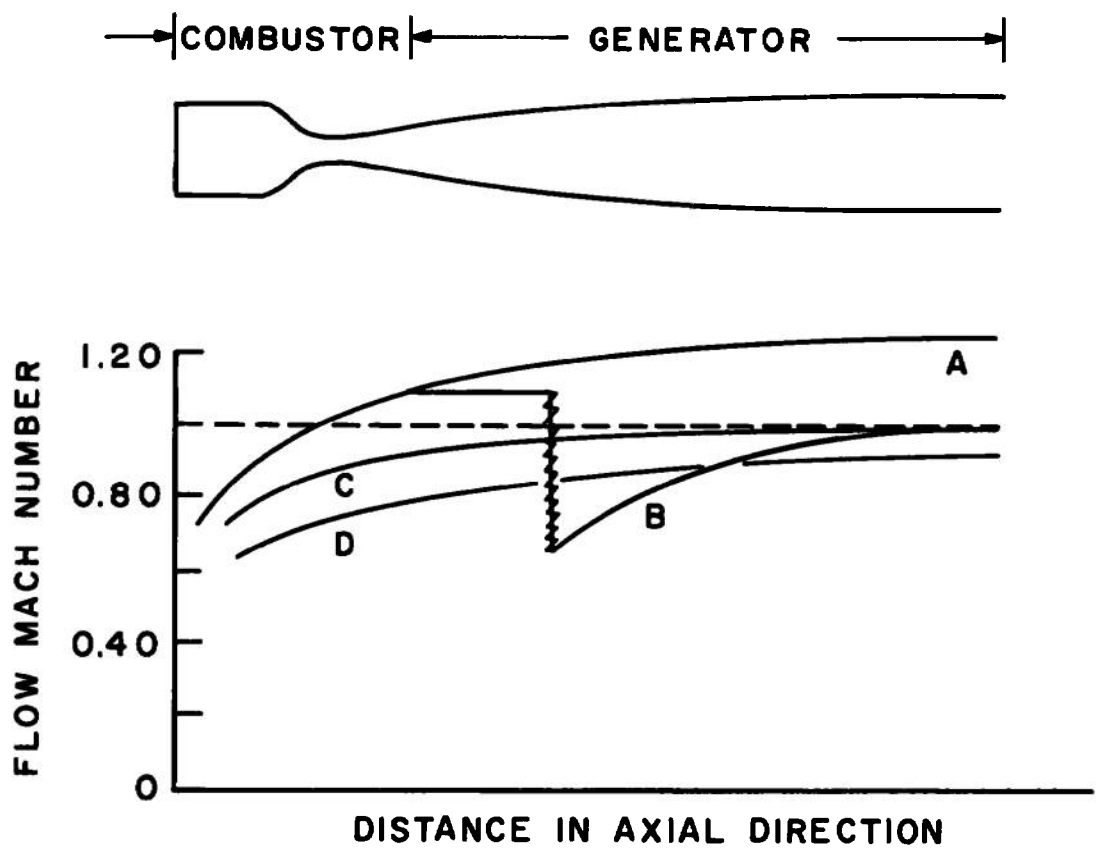
Fig. 16 Operation of an MHD Generator with a Sonic Exit
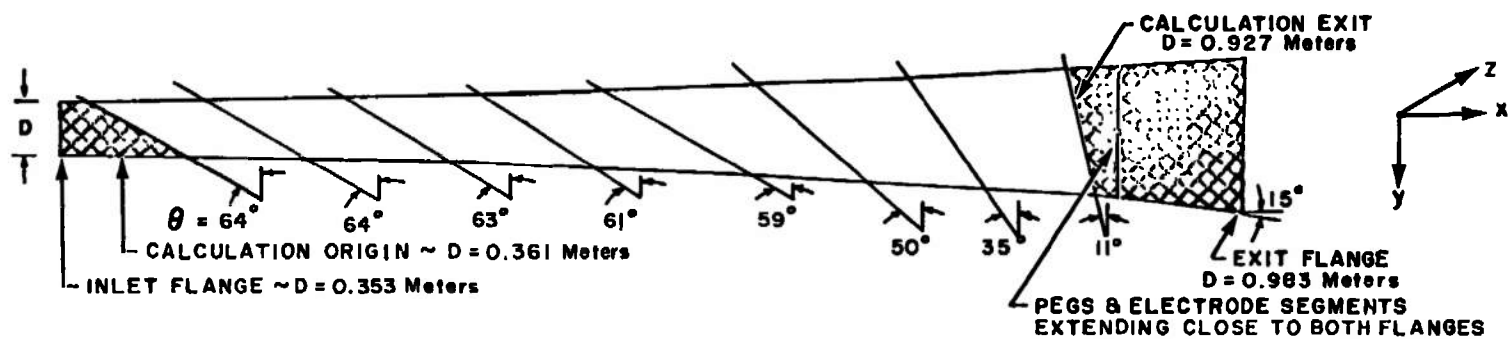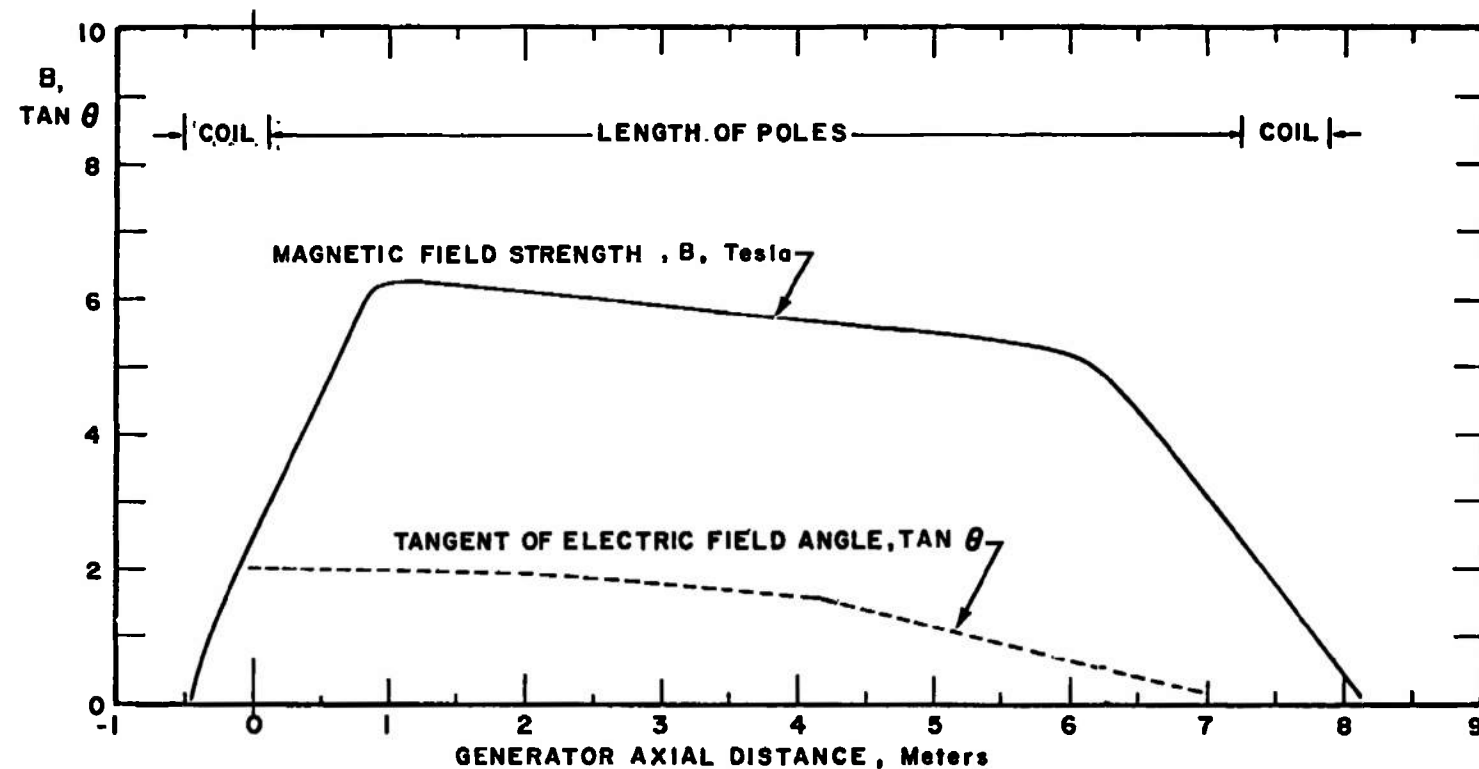
Fig. 17 Magnetic Field Distribution, Electric Field Angle, and Channel Layout
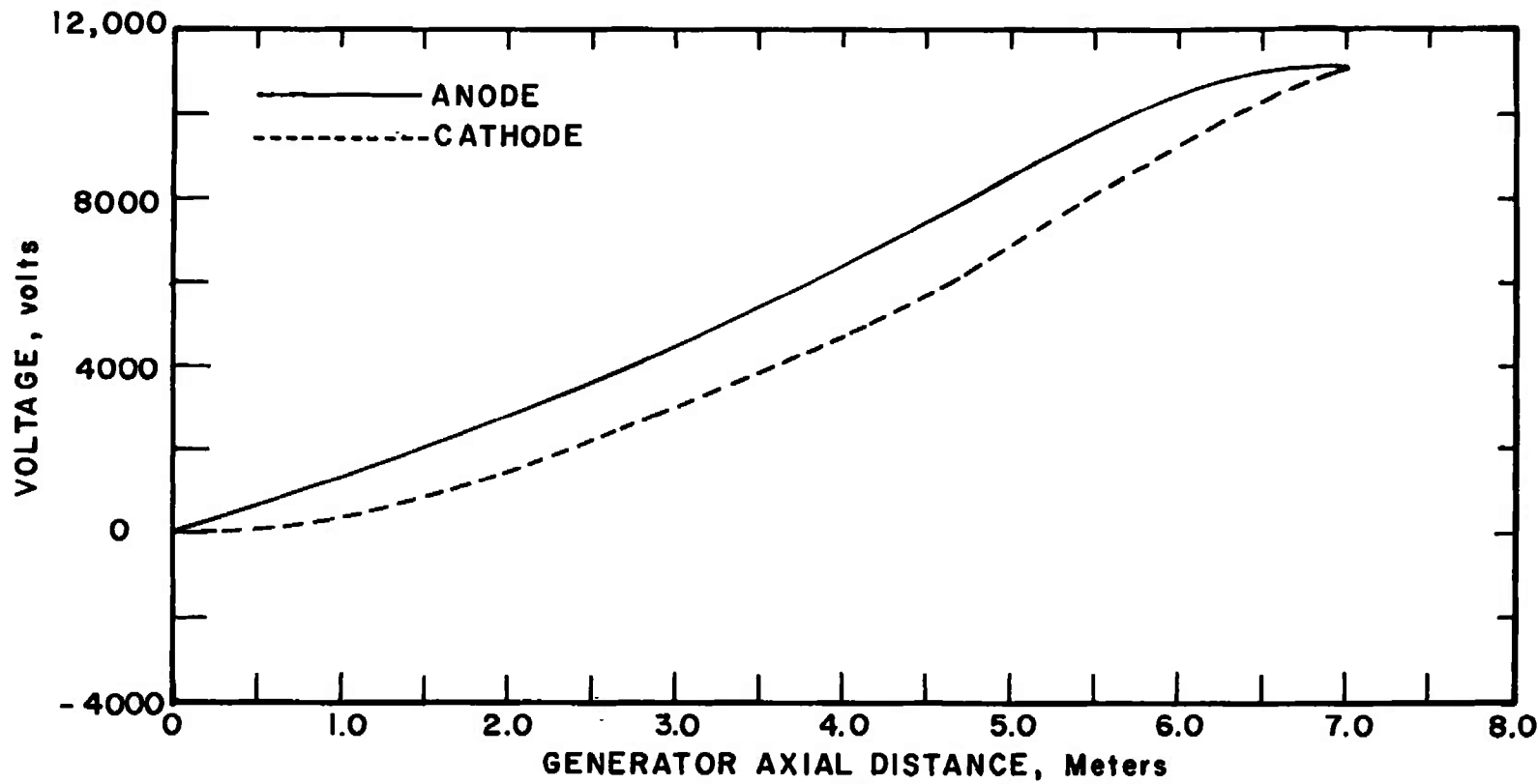
Fig. 18 Anode and Cathode Voltage Distribution for Design Channel in Diagonally Connected Configuration
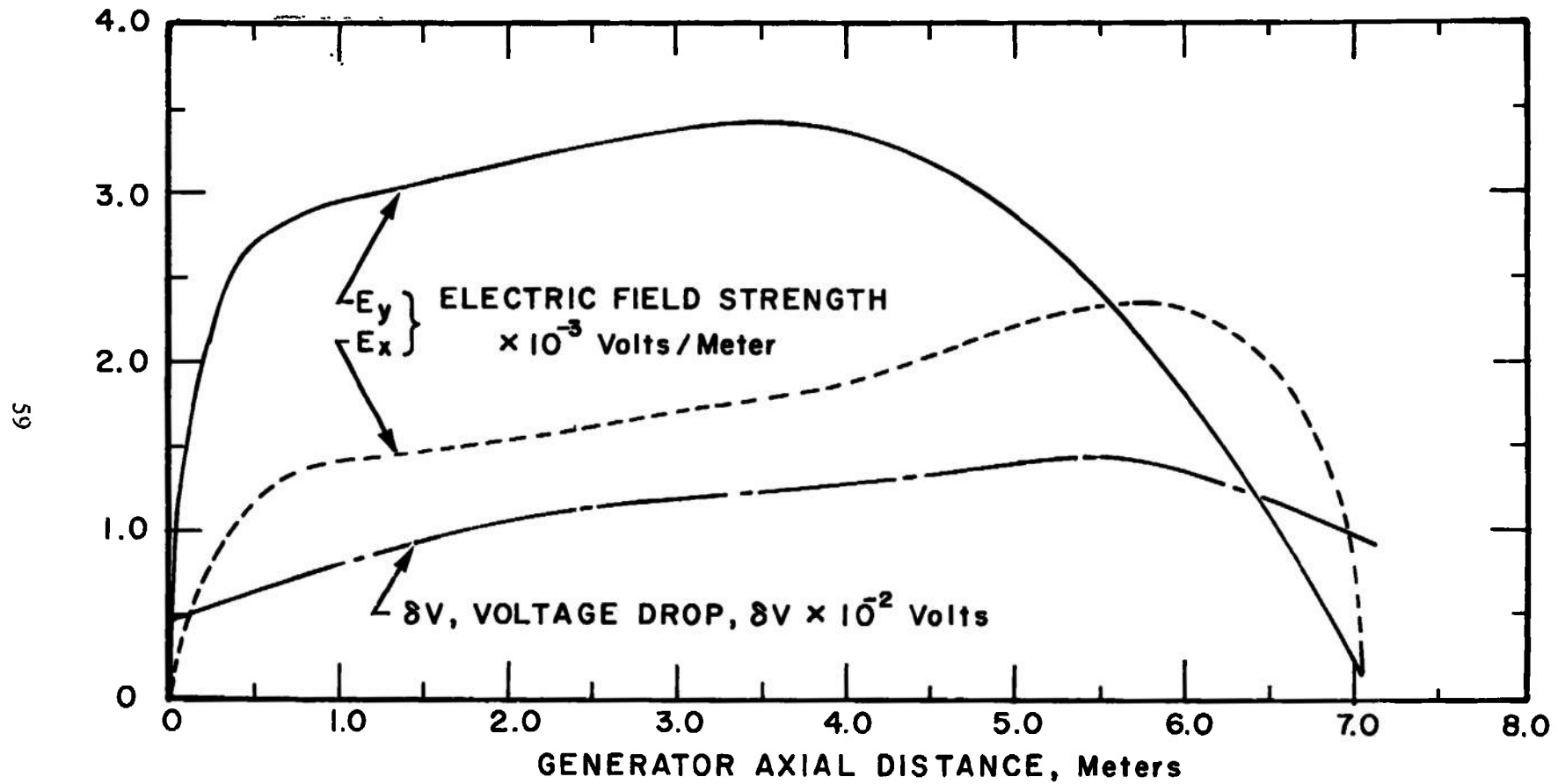
Fig. 19 Electric Field Strengths and Electrode Voltage Drop for Design Channel in Diagonally Connected Configuration
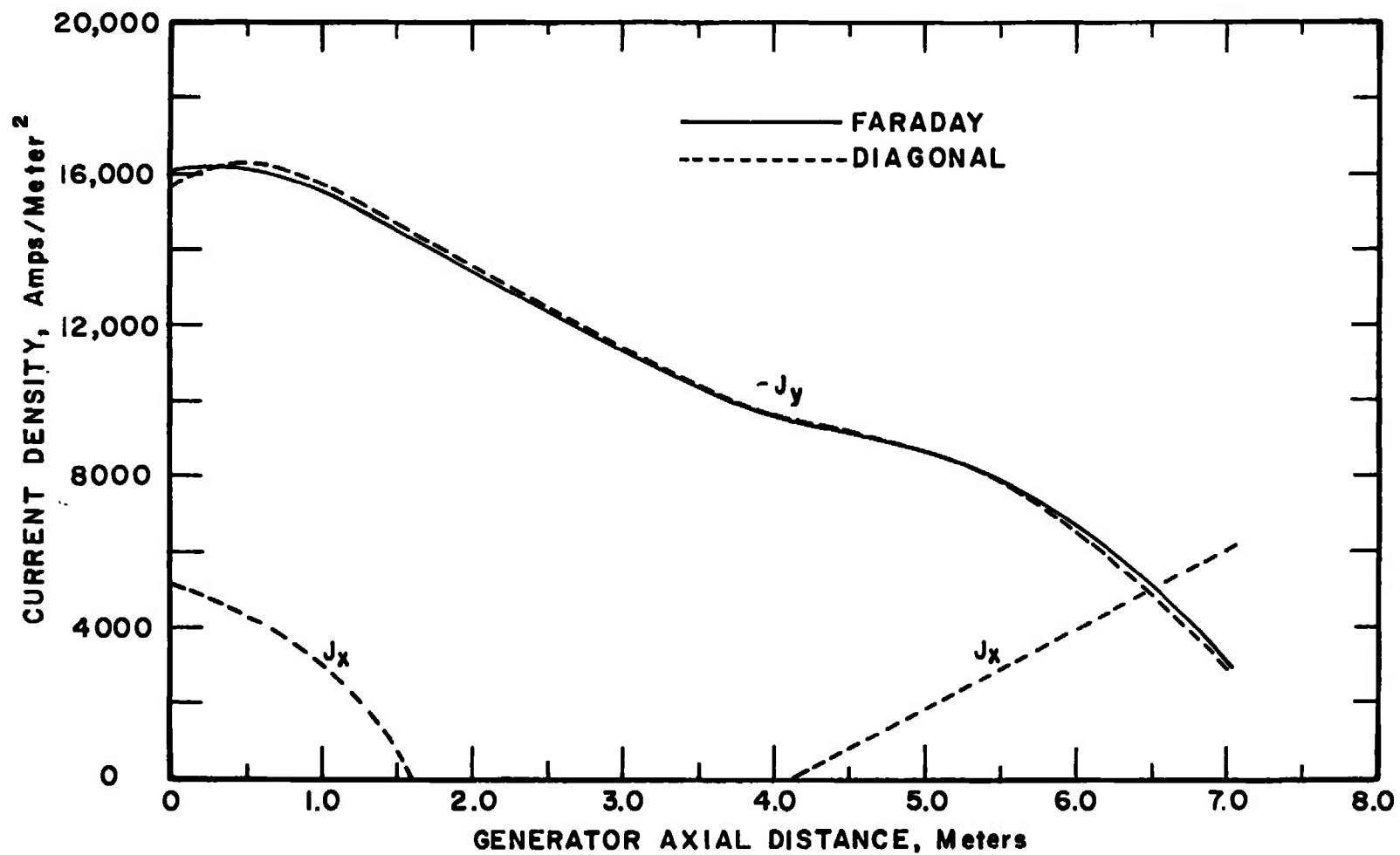
Fig. 20 Current Density Distribution for Design Channel in Faraday and Diagionally Connected Configuration
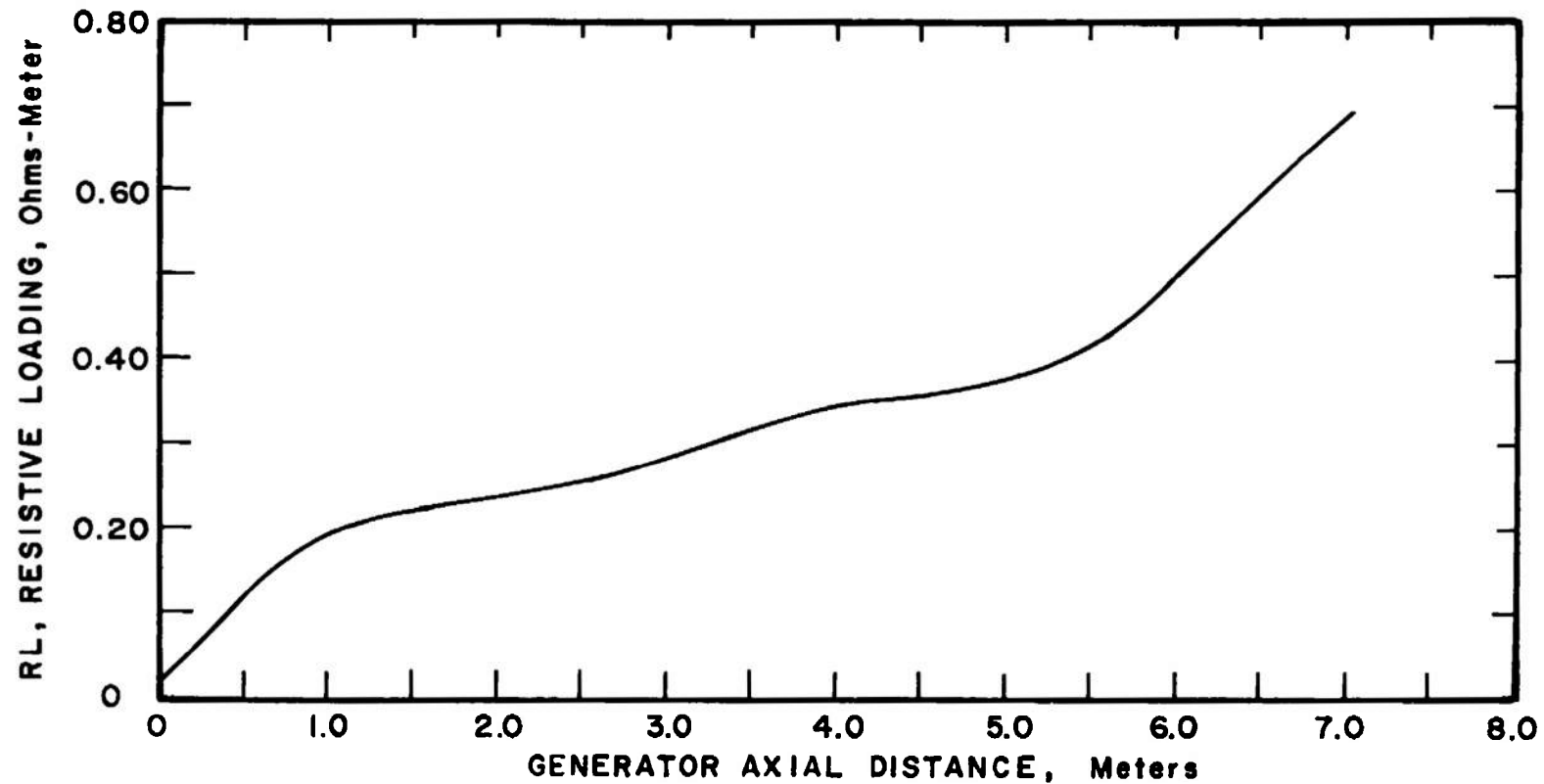
Fig. 21 Resistive Loading Schedule for Segmented Faraday Generator Configuration
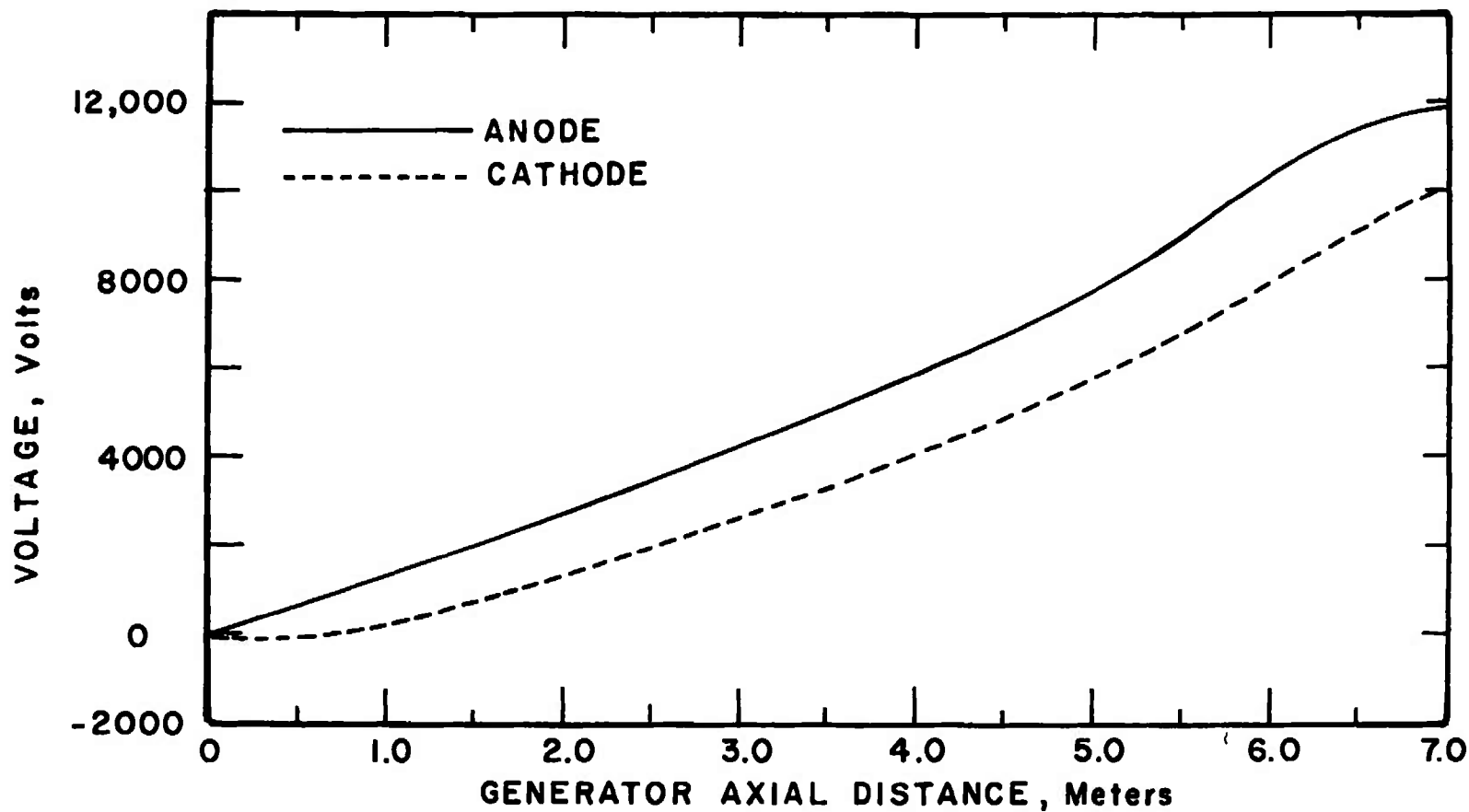
Fig. 22 Anode and Cathode Voltage Distributions for Design Channel in the Faraday Configuration
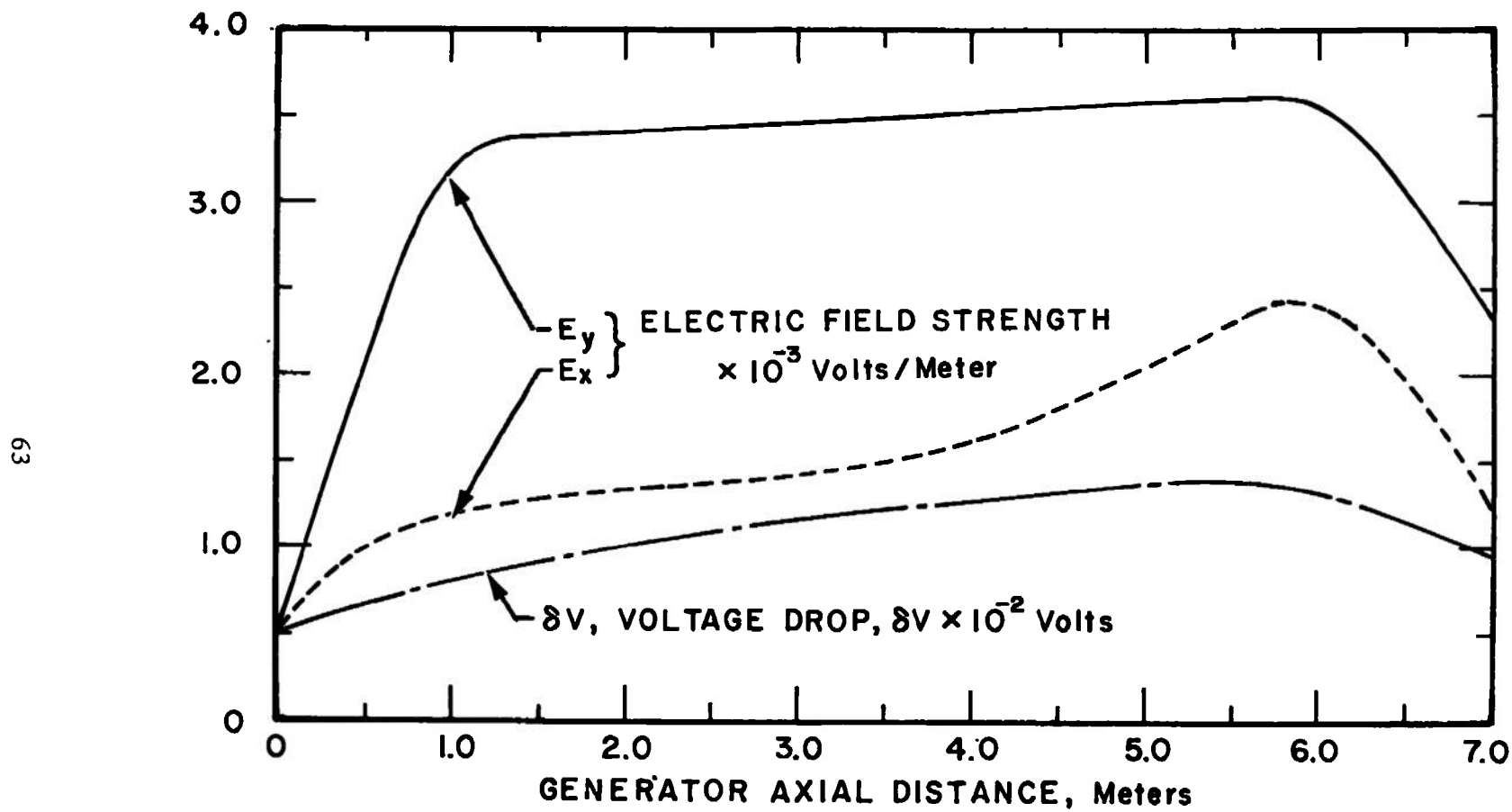
Fig. 23 Electric Field Strengths and Electrode Voltage Drop for Design Channel in the Faraday
Configuration
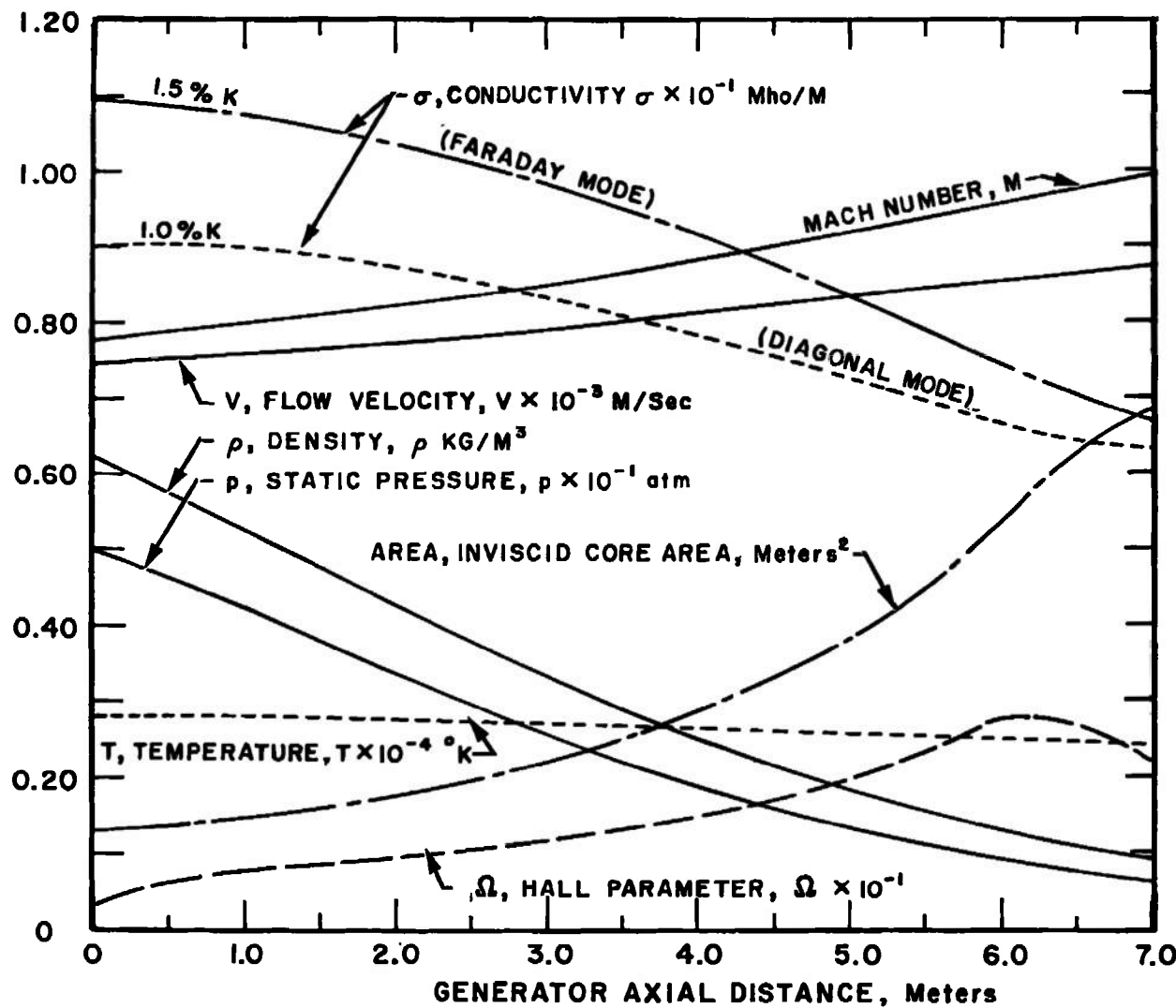
Fig. 24 Variation of Flow Properties within the Design Channel for a Nitrogen-Oxygen Ratio of 1.25
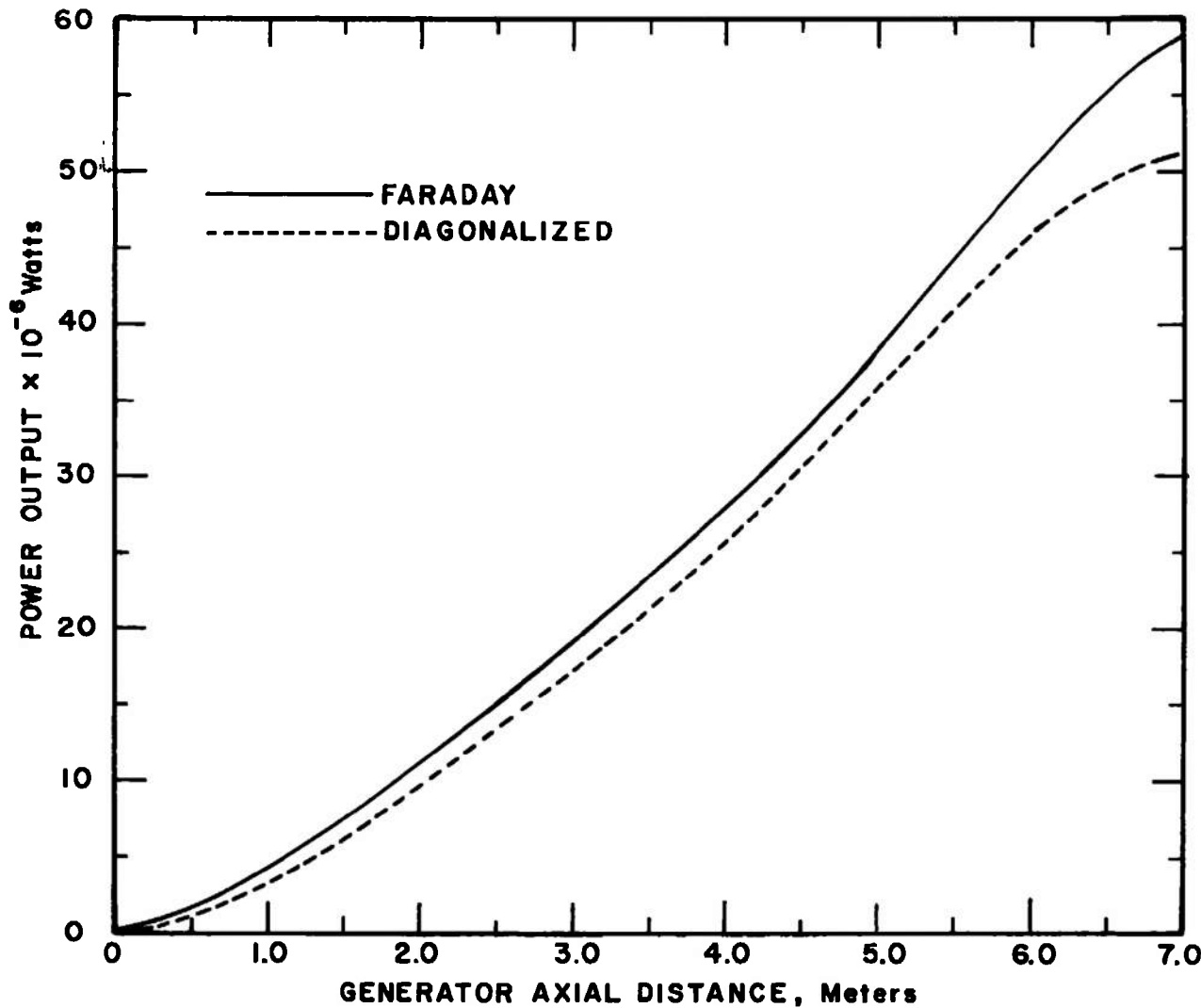
Fig. 25 Distribution of Power Output in Design Channel in Two Modes of Operation
(Electrode Losses Included)
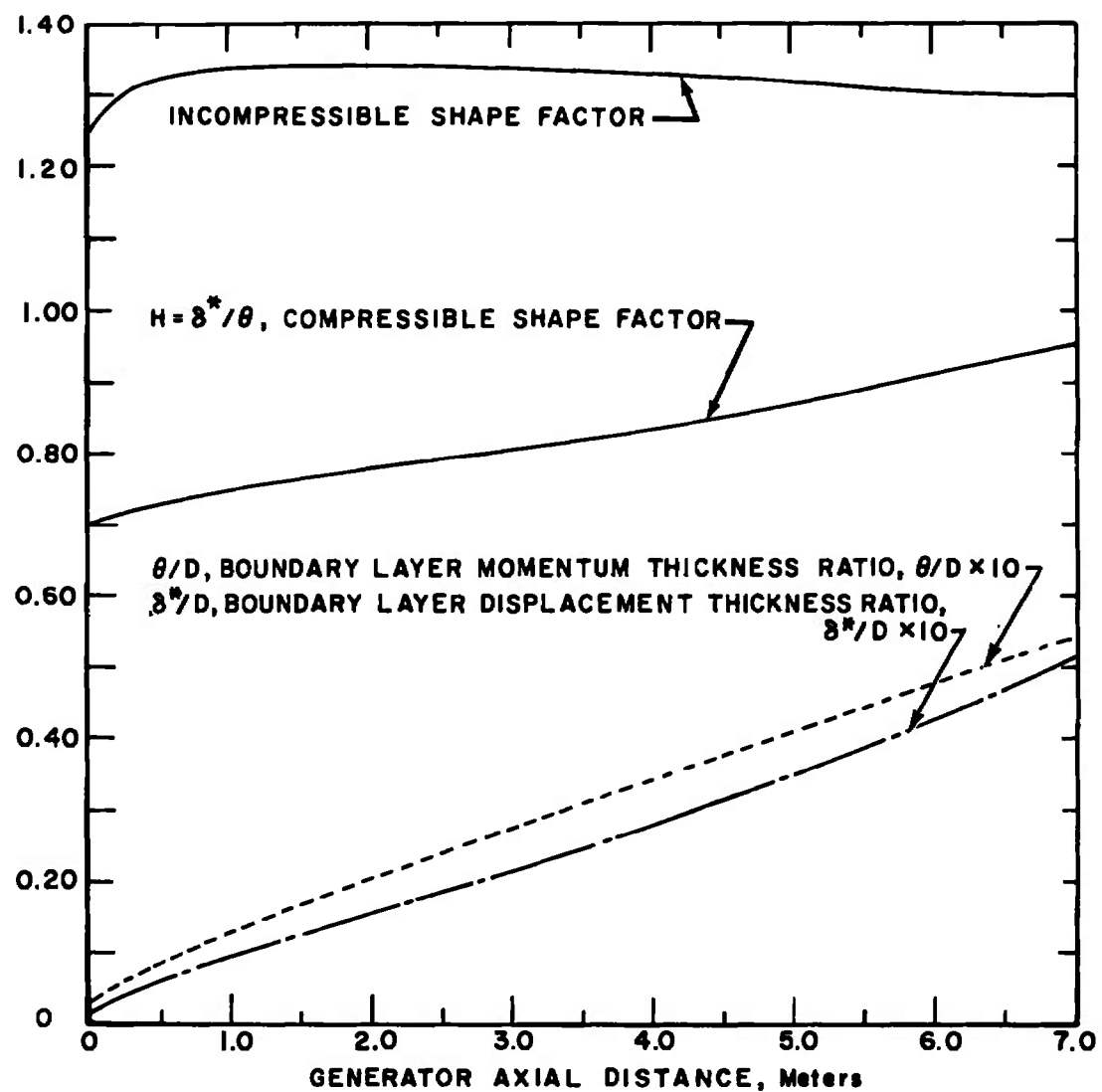
Fig. 26 Compressible Boundary Layer Characteristics for Design Channel in Either Faraday or Diagonally Connected Mode
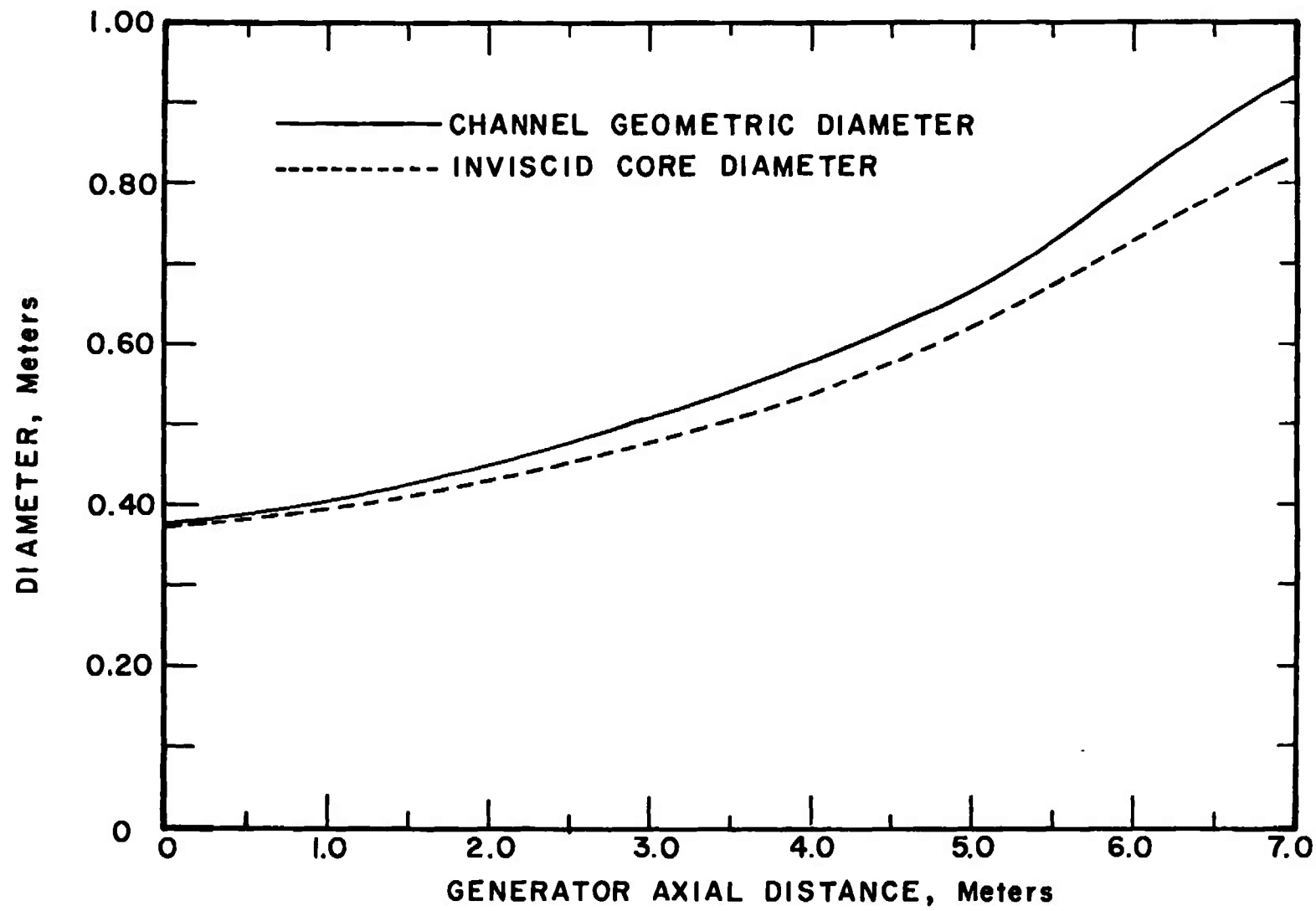
Fig. 27 Comparison of Inviscid Core Diameter with Channel Geometric Diameter
(Includes Wall Roughness Effects)

MAGNET POLE LENGTH = 7.1

$B=0$ $B=2.5T$ $B_{MAX}=6.2T$ $B=5.2T$ $B=3.1T$ $B=0$

8.65

0.5

0.35 0.36 **SEGMENTED ELECTRODE WALL** 0.93 0.98

1.5°

INLET
FLANGE

OUTLET
FLANGE

NOTE – ALL DIMENSIONS IN METERS
        VOLTAGES INDICATED FOR FARADAY (DIAGONAL) CONFIGURATIONS

0.5 **ACTIVE LENGTH = 7.0** 1.15

+49V (−27V)

0.35 0V 0.36 **INSULATED PEG WALL**

−49V (+27V)

+11860V
(+10992V)

+10970V
(+10986V)

0.93 0.98

1.5°

+10080V
(+10980V)

INLET
FLANGE

OUTLET
FLANGE

Fig. 28 Proposed Layout of Design Channel
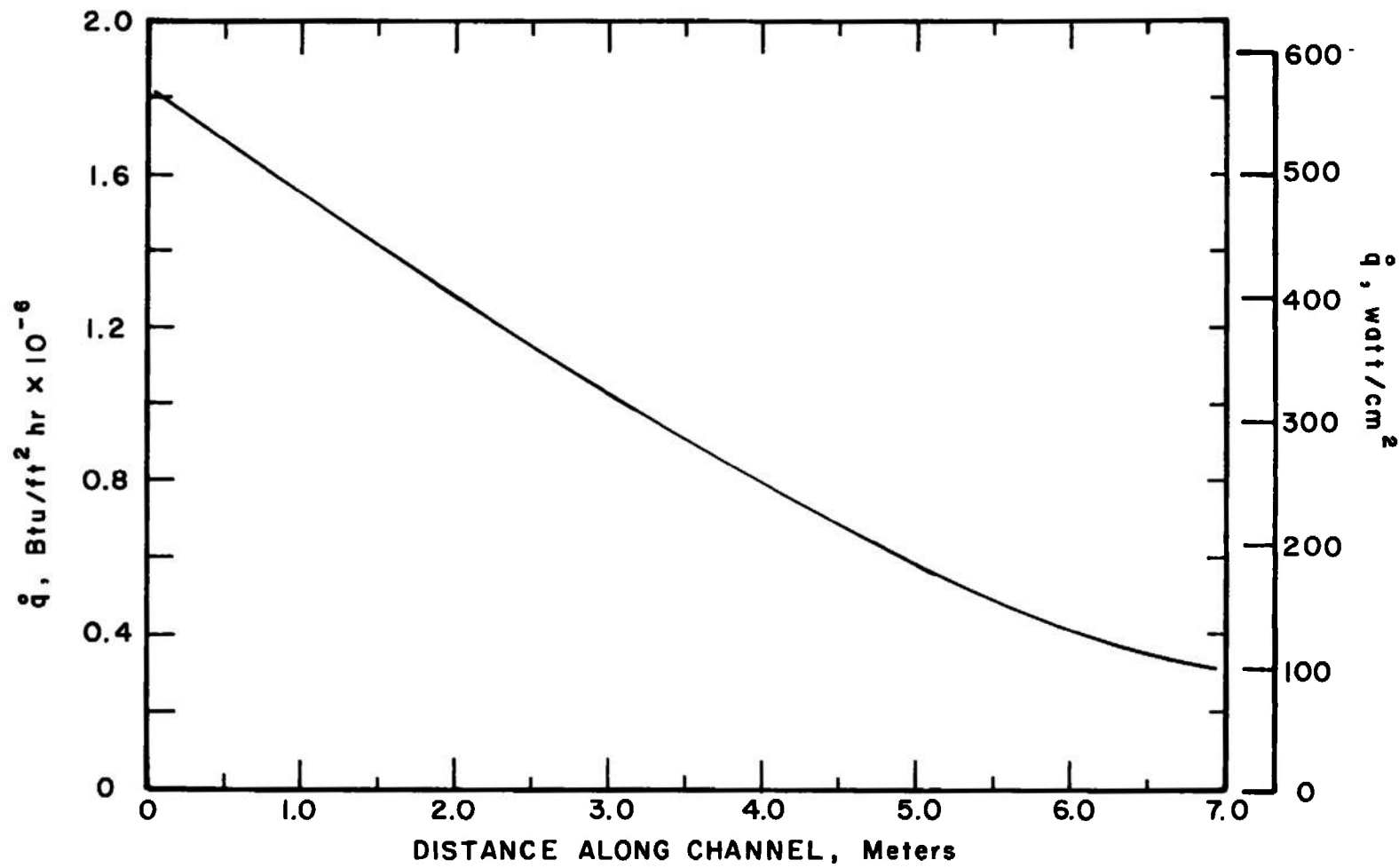
Fig. 29 Estimated Heat-Transfer Loading in Design Channel
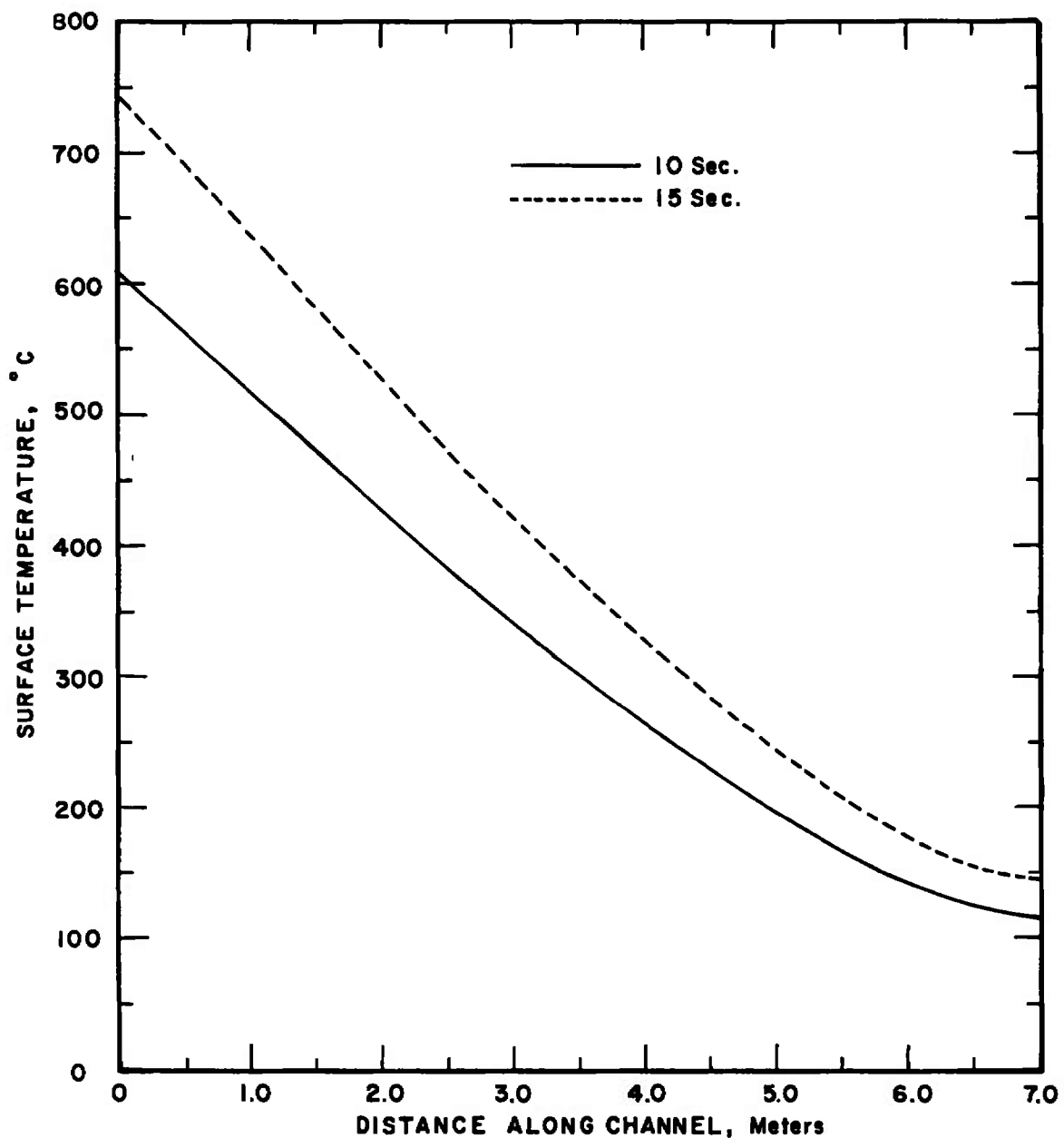
Fig. 30 Calculated Surface Temperature of Pegs versus Axial Distance
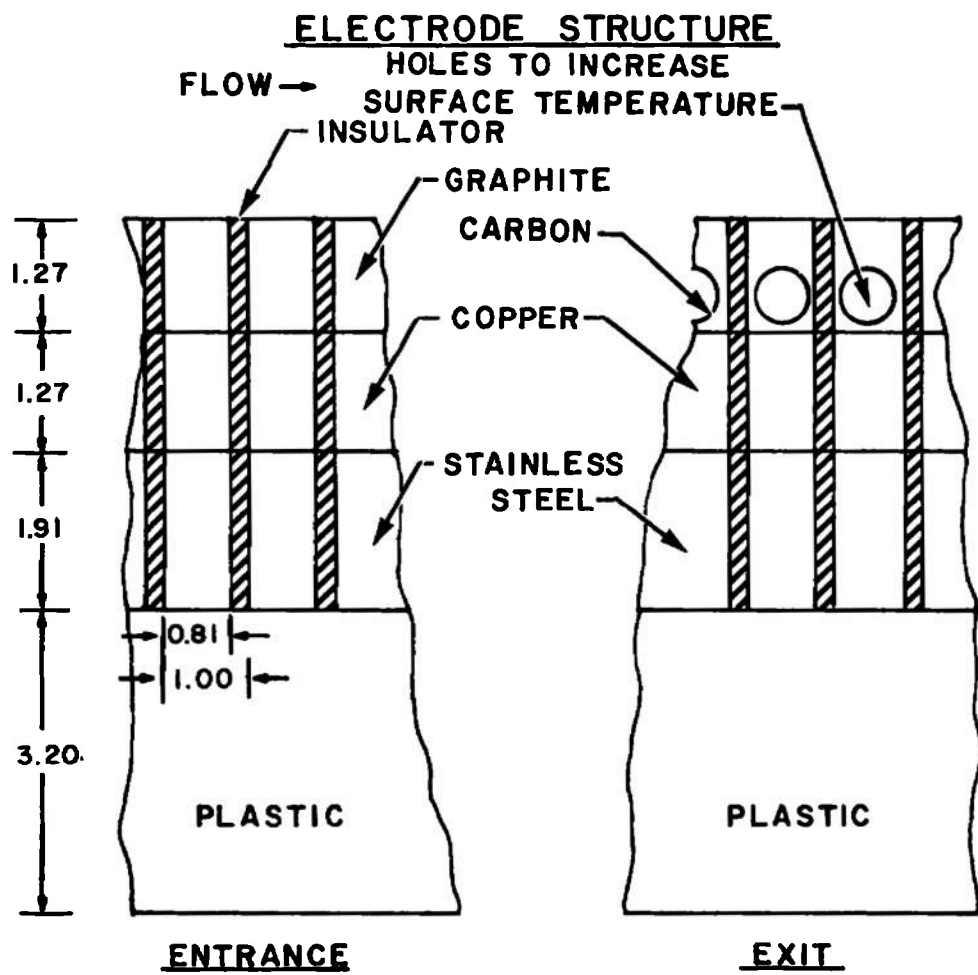
Fig. 31 Schematic Cross Section of Channel Wall
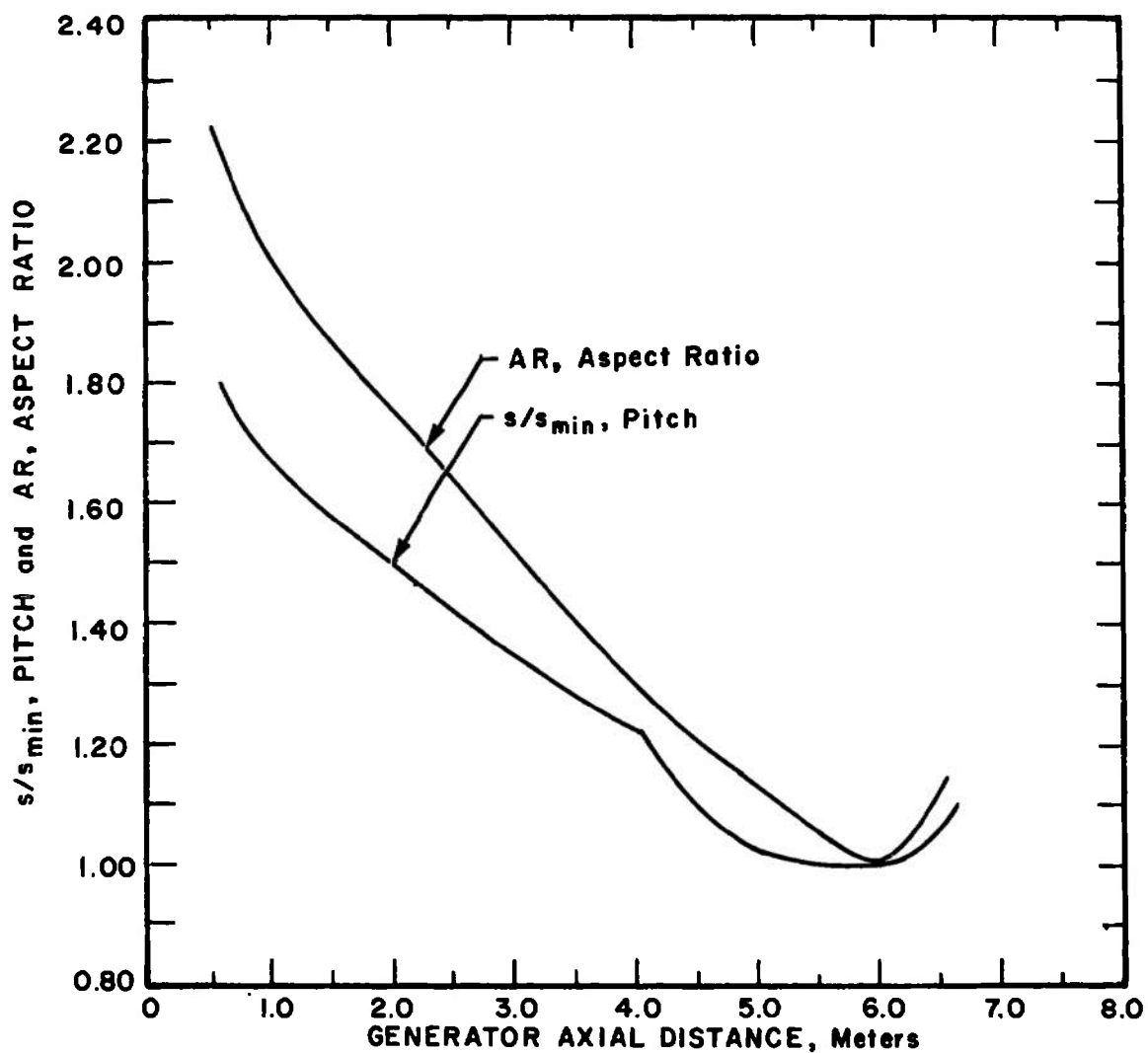
Fig. 32 Generator Aspect Ratio and Electrode Pitch versus Axial Location

Fig. 33 Schematic of the Proper, Transition, and Fringe Regions of a Diagonalized MHD Generator Channel
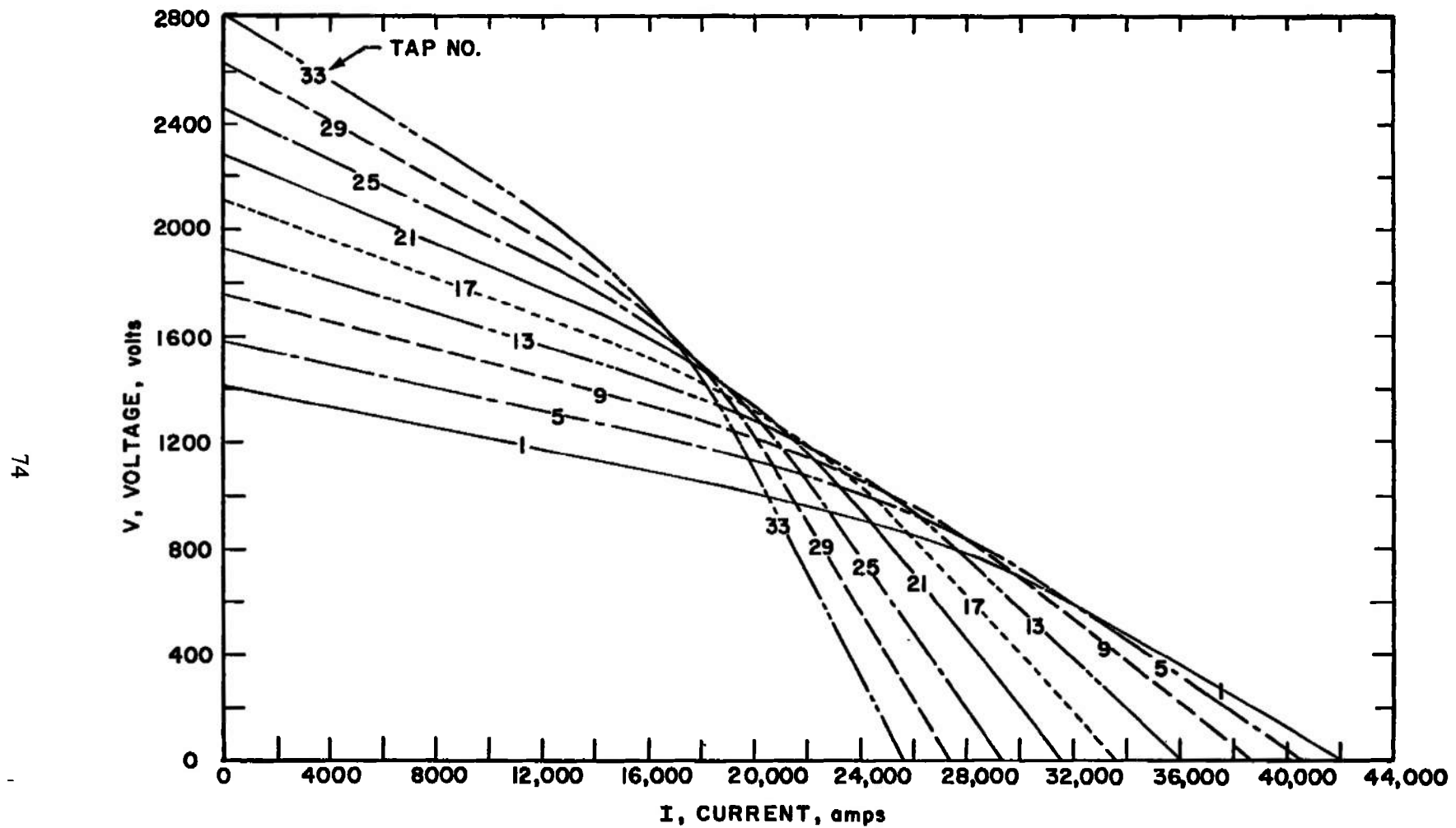
Fig. 34 Power Supply Characteristics for Different Transformer Tap Settings (Parallel Connections)

27 MW SYSTEM (REQUIRES NEW RECTIFIER SUBSTATION # 5)

RECTIFIER SUBSTATION # 4
2500 VDC
8000 A

161 KV

13.8 KV

PES TRANS # 4 WINDING #2

UG LINE

ACB 2 E1

UG LINE

POLE TOP SWITCHES

REACTOR BANK 0- 14 ohms

LOAD TAP CHANGING TRANSFORMER 1040 - 2080 VAC OUTPUT

CABLE DUCT

LOAD 16,000 A TOTAL

RECTIFIER SUBSTATION # 5
2500 VDC , 8000 A
(ADDED TO EXISTING POWER SUPPLY)
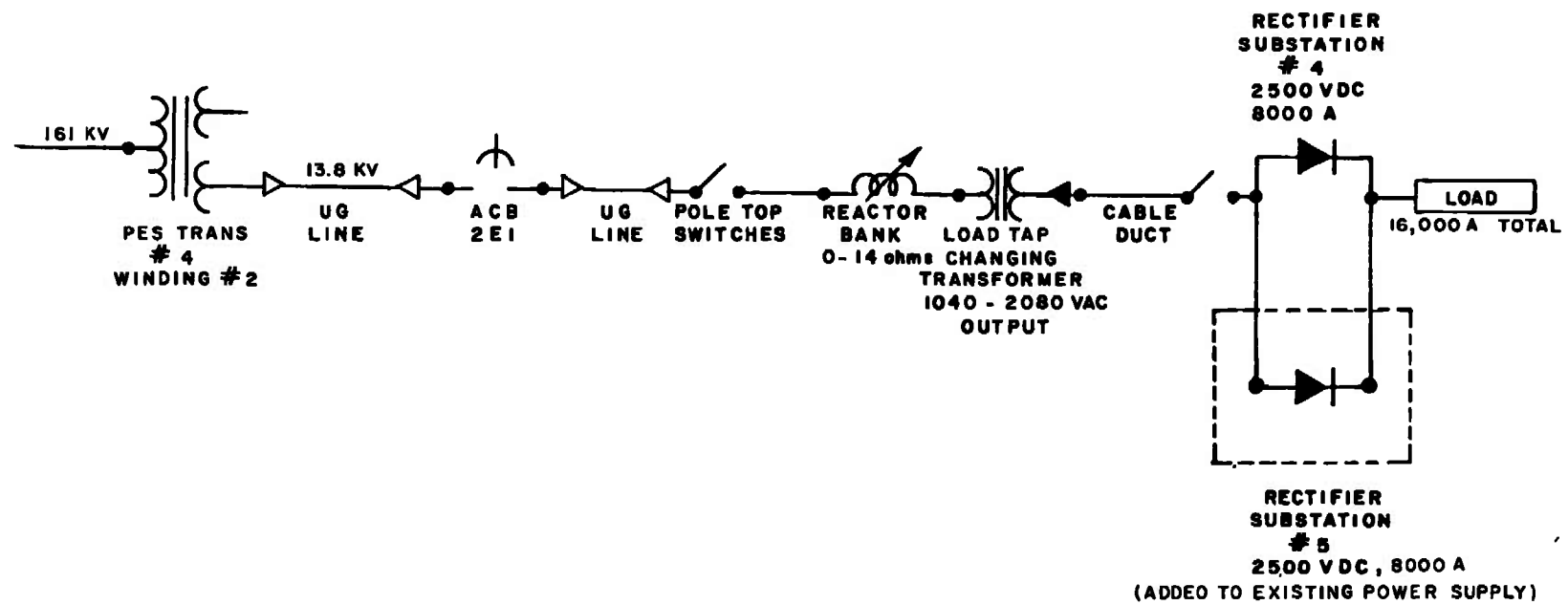
Fig. 35 Proposed 27-MW Power Supply

D.C. Output
Bus Bars
(Output Side)

Water Cooled Rectifier
Stack (3 of 6 Shown)

Transducer
(D.C. Current
Measurement)

3 Phase A.C. Bus Bars
(Input Side)

Surge Protection
Network

Bus Support
Insulator
(Typical of 3)

A.C. Current
Transformer
(Typical of 3)
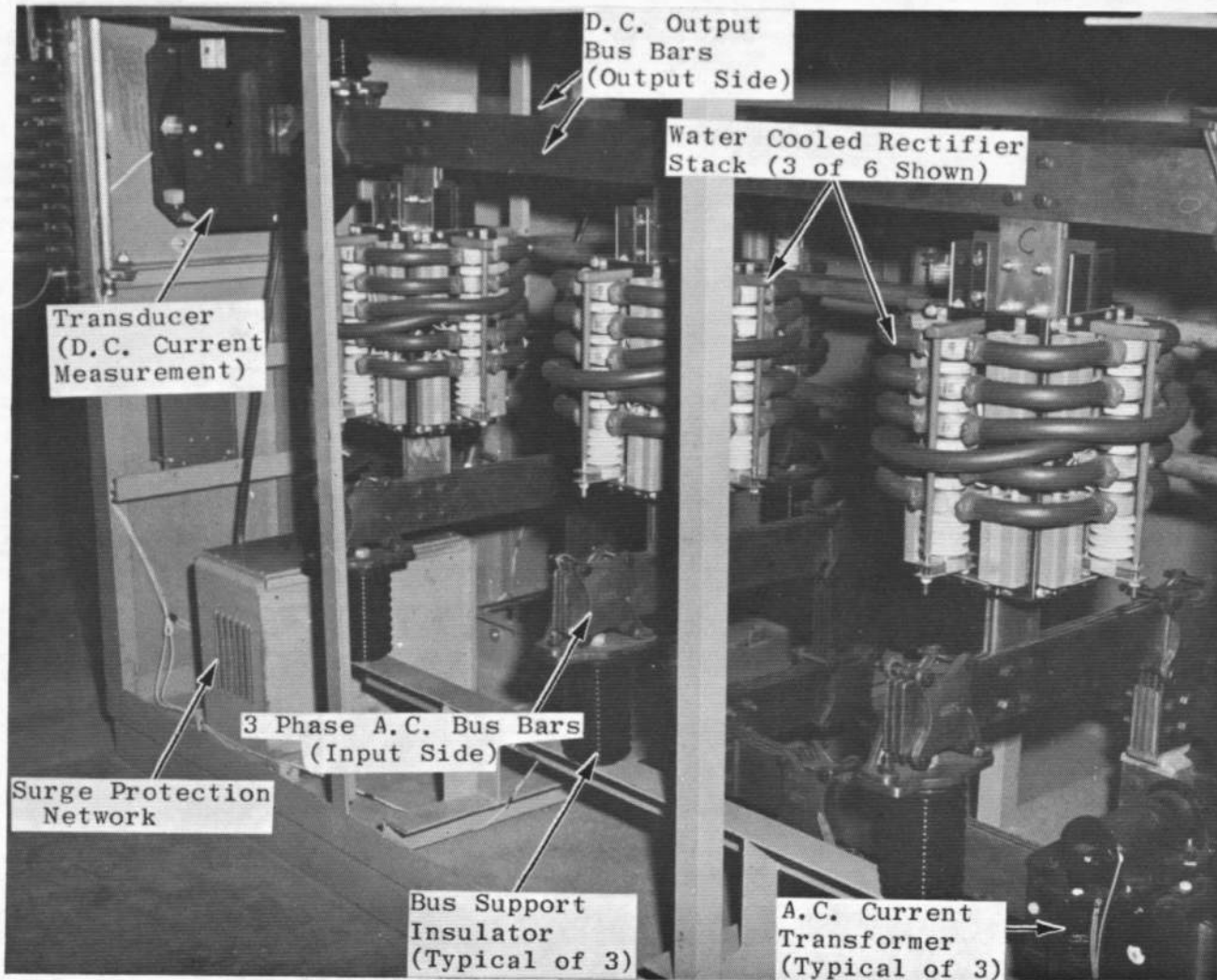
Fig. 36 Photograph of Rectifier Substation No. 4 (20 MW)

Fig. 37 As-Built Drawing of Rectifier Substation No. 4 (20 MW)

a. Inlet, $x = -\ell_p/2$

b. Center, $x = 0$

$$w_0 = \frac{w_{outlet} + w_{inlet}}{2}$$
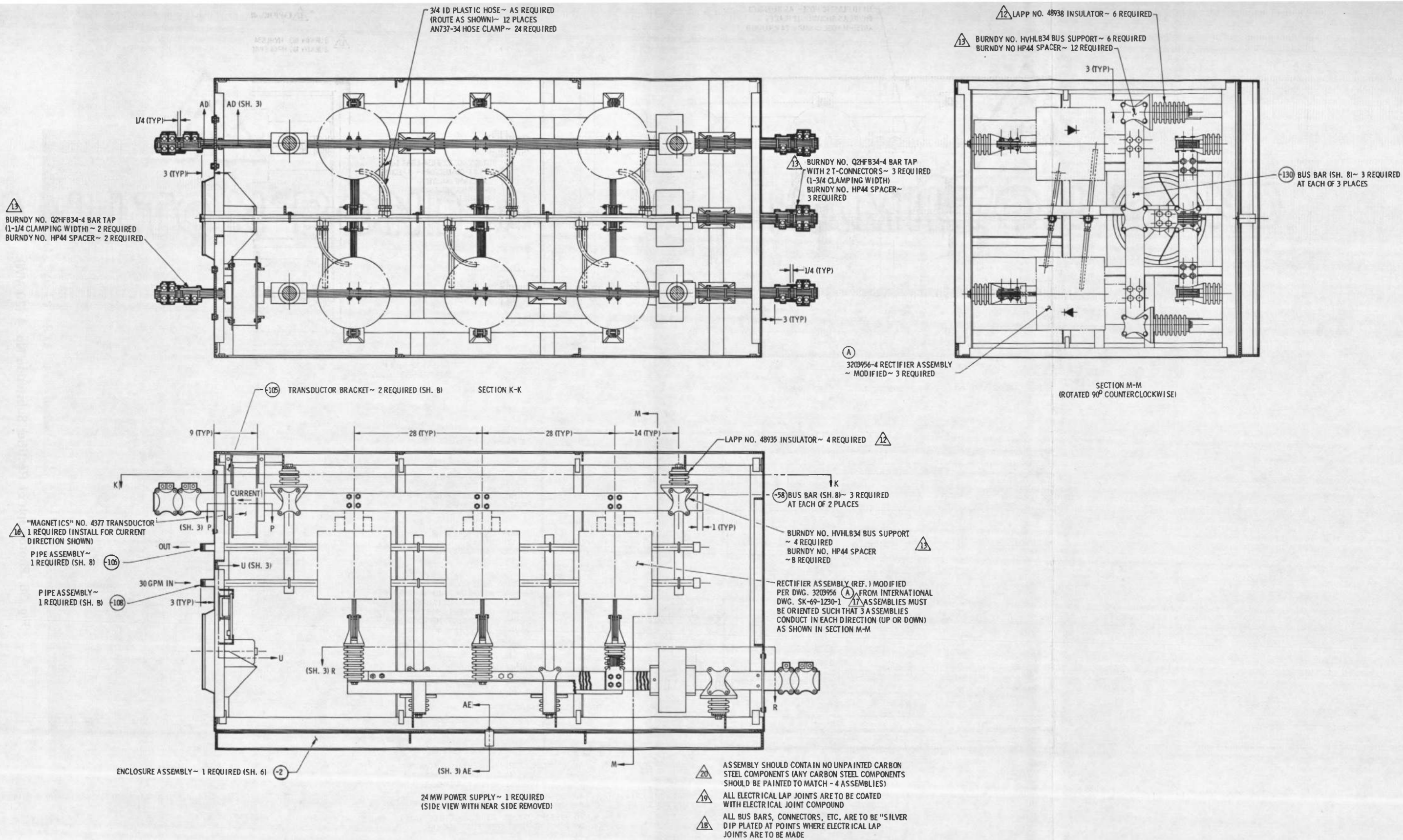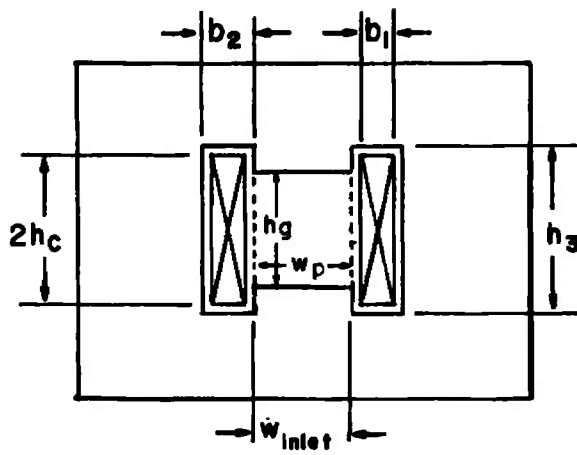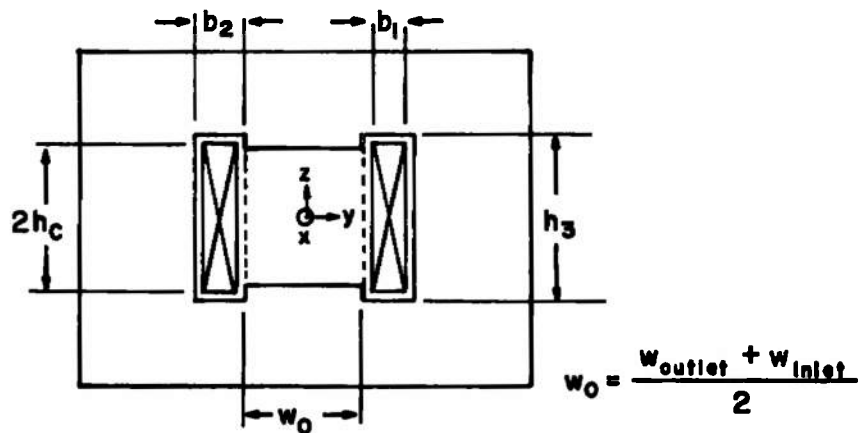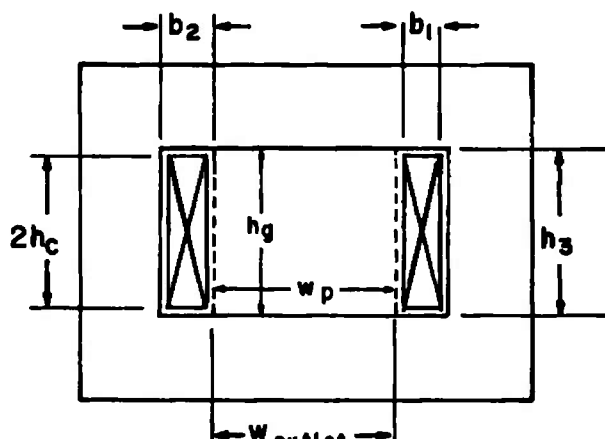
c. Outlet, $x = +\ell_p/2$

Fig. 38 Schematic of the Magnet Cross Section at Three Axial Stations

79
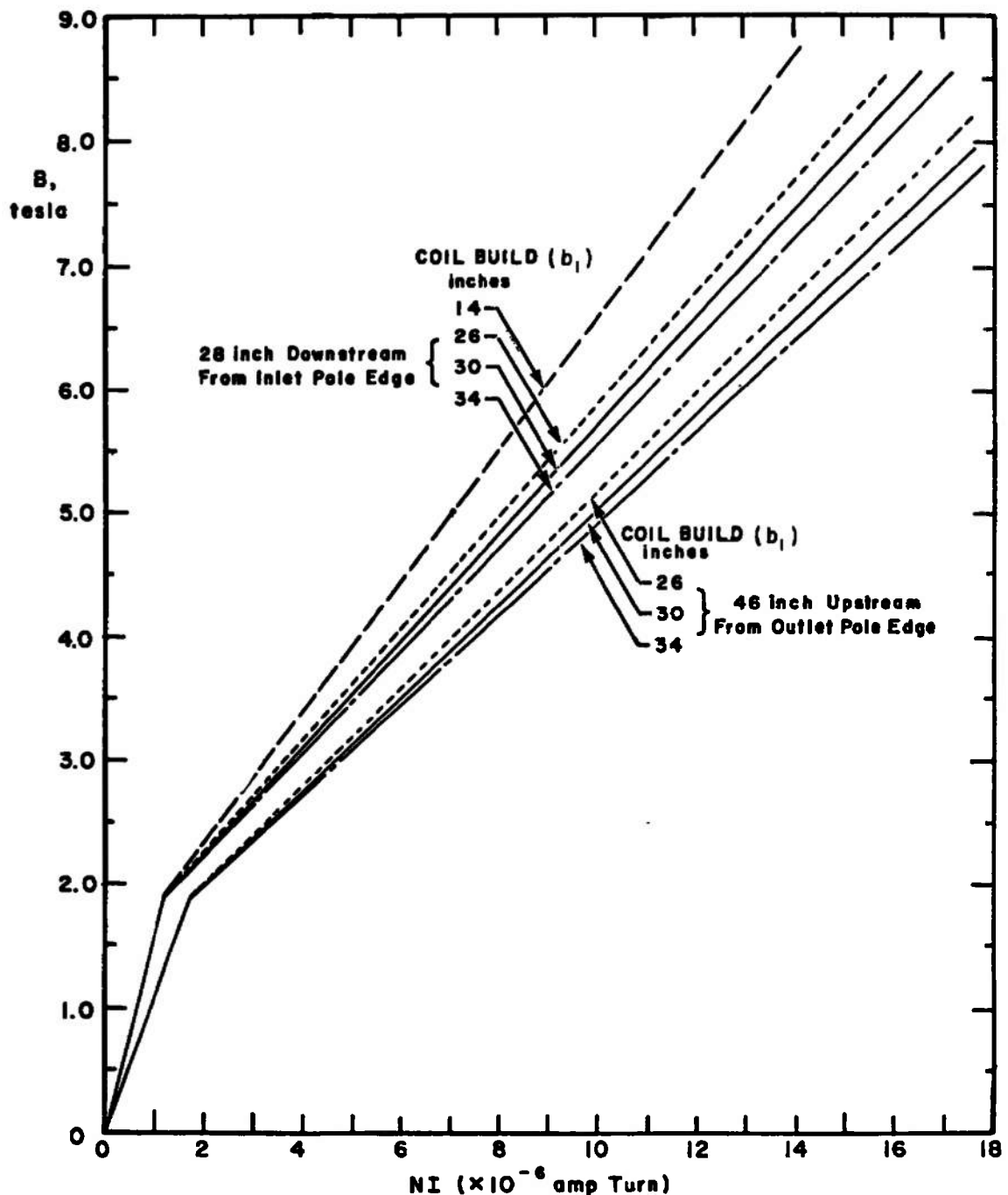
Fig. 39 Magnetization of Curves for Magnet Having Bore 0.71 x 71 m at Inlet and 1.17 x 1.17 m at Exit
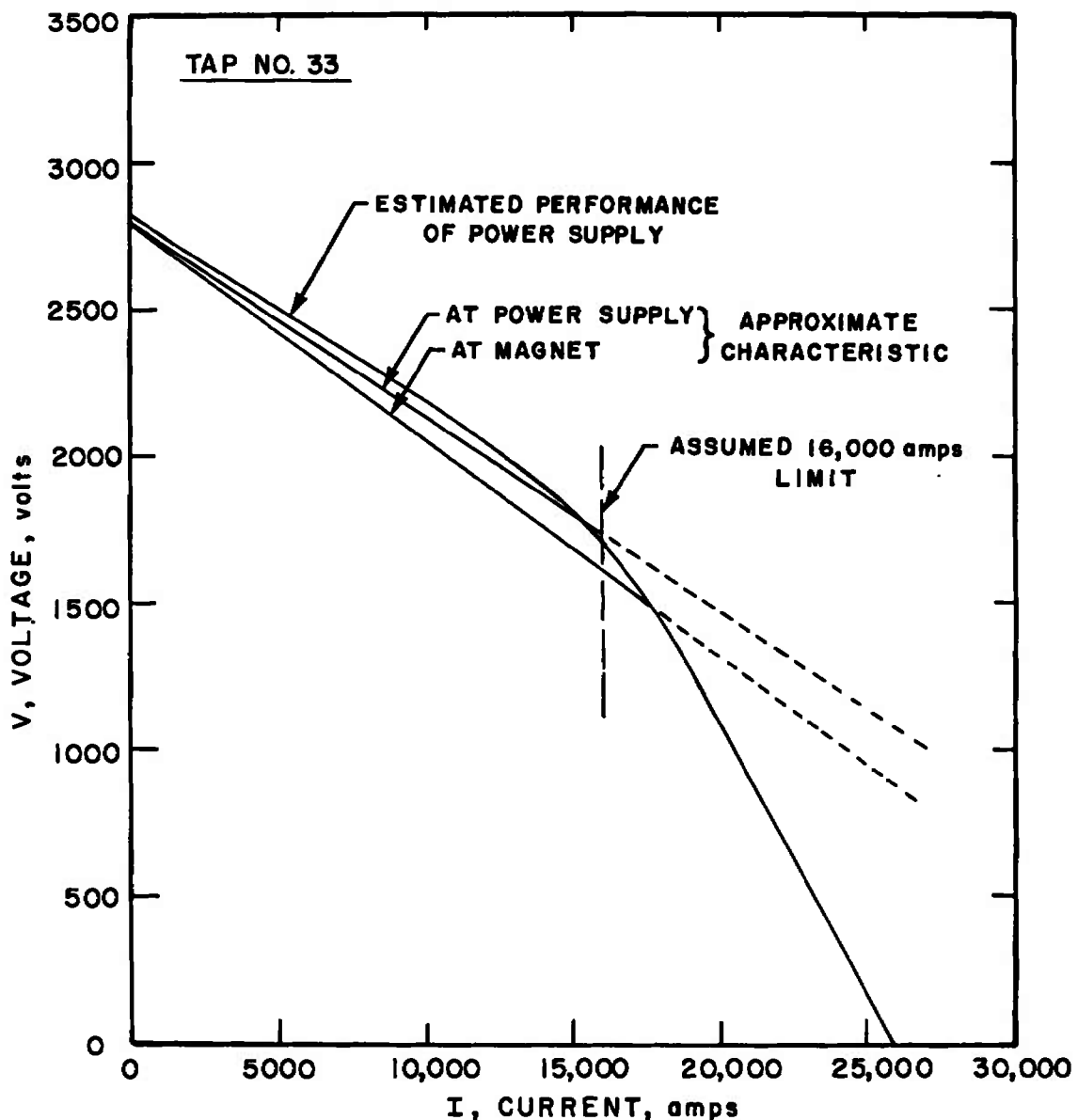
Fig. 40 Approximation to the Volt-Ampere Characteristics of the
27-MW Power Supply
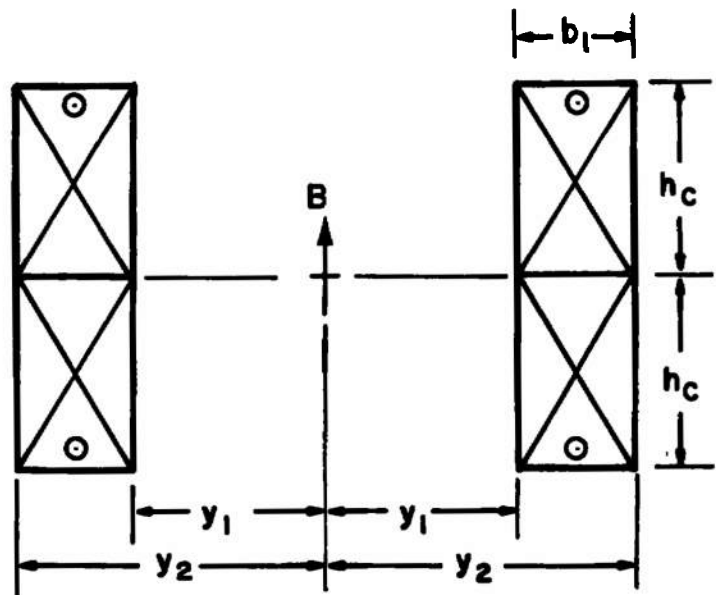
$$y_1 = w_0/2 + 2.54 \text{ cm}$$

$$y_2 = y_1 + b_1$$

Fig. 41 Coil Cross Section at Center of Magnet

82
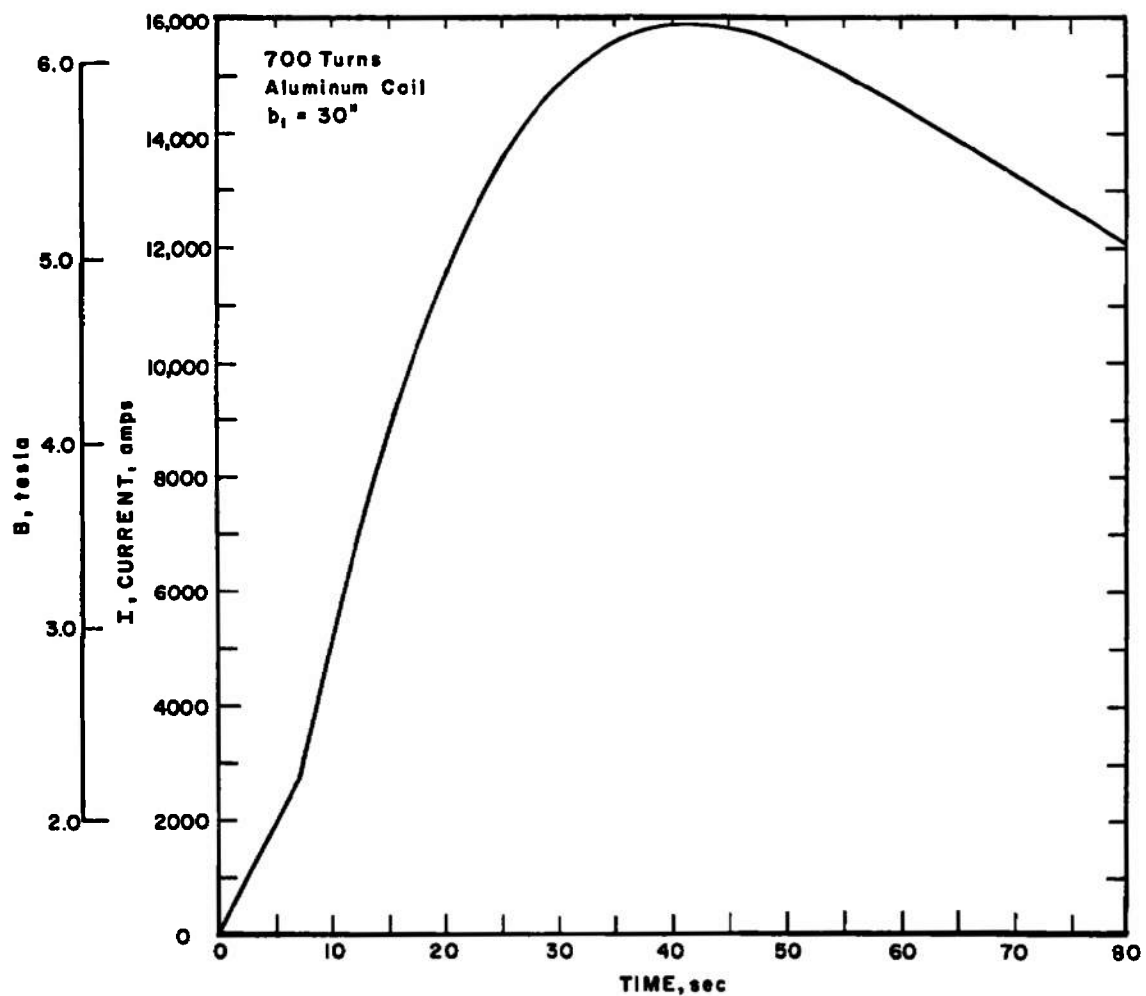
Fig. 42　Current and Magnetic Field versus Time for an Aluminum
Coil (700 Turns, 0.85 Space Factor, B_1 = 30 in.)
Operated on the Tap 33 Power Supply Characteristic
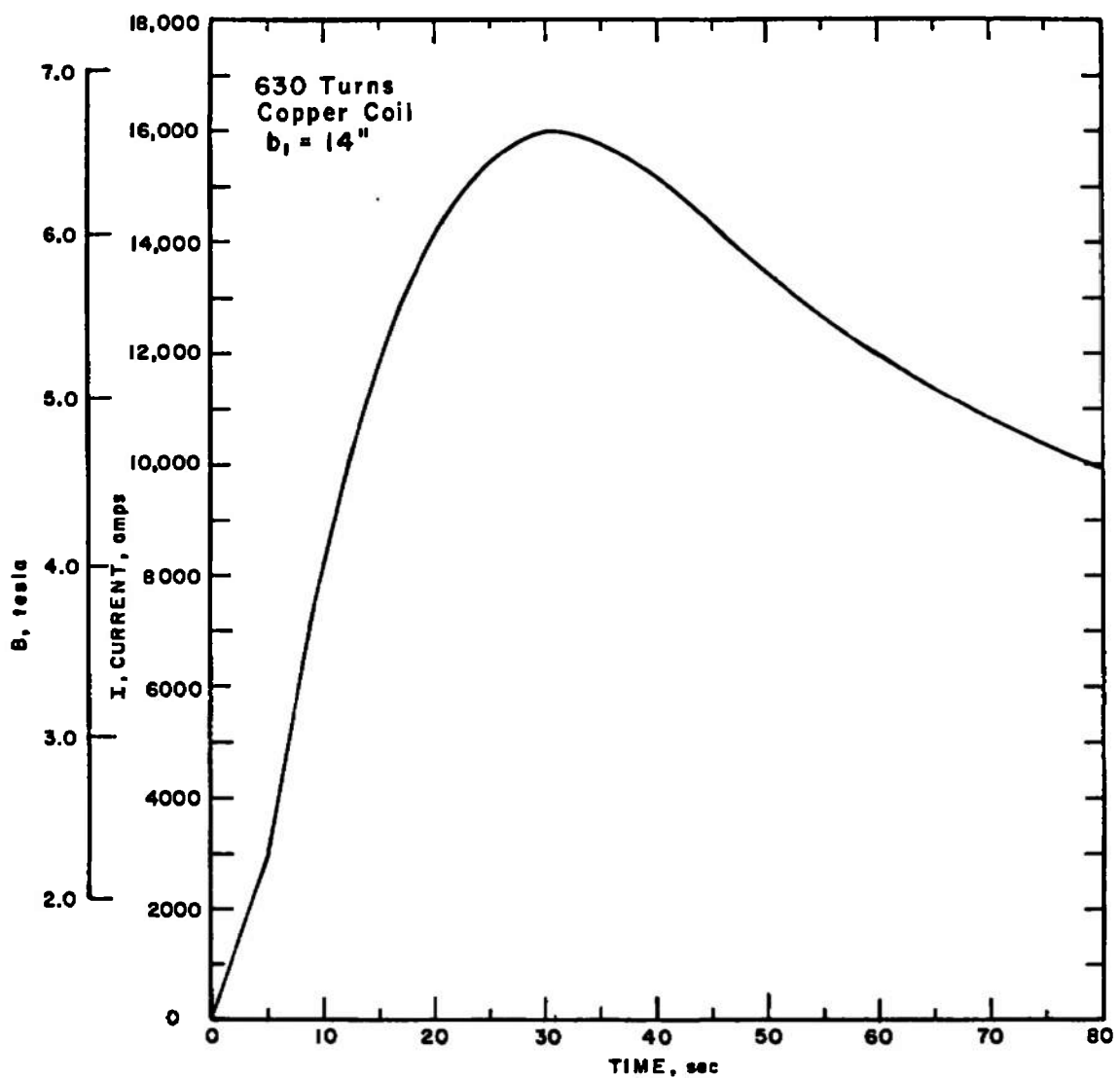
Fig. 43 Current and Magnetic Field versus Time for a Copper Coil
(630 Turns, 0.85 Space Factor, b_1 = 14 in.) Operated
on Tap 33 Power Supple Characteristics
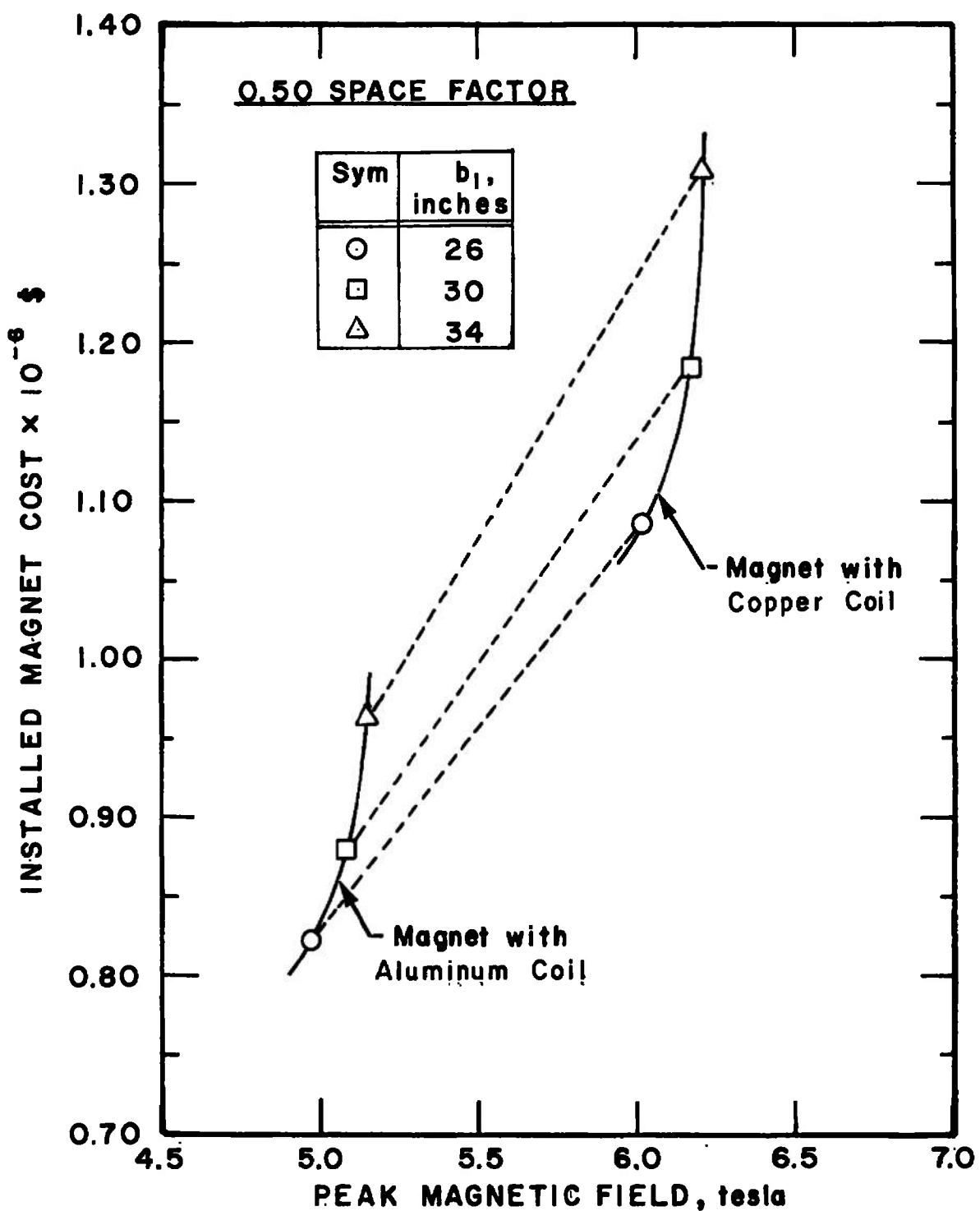
Fig. 44 Cost versus Magnetic Field for Different Sized Coils
in Aluminum and Copper at a 0.50 Space Factor
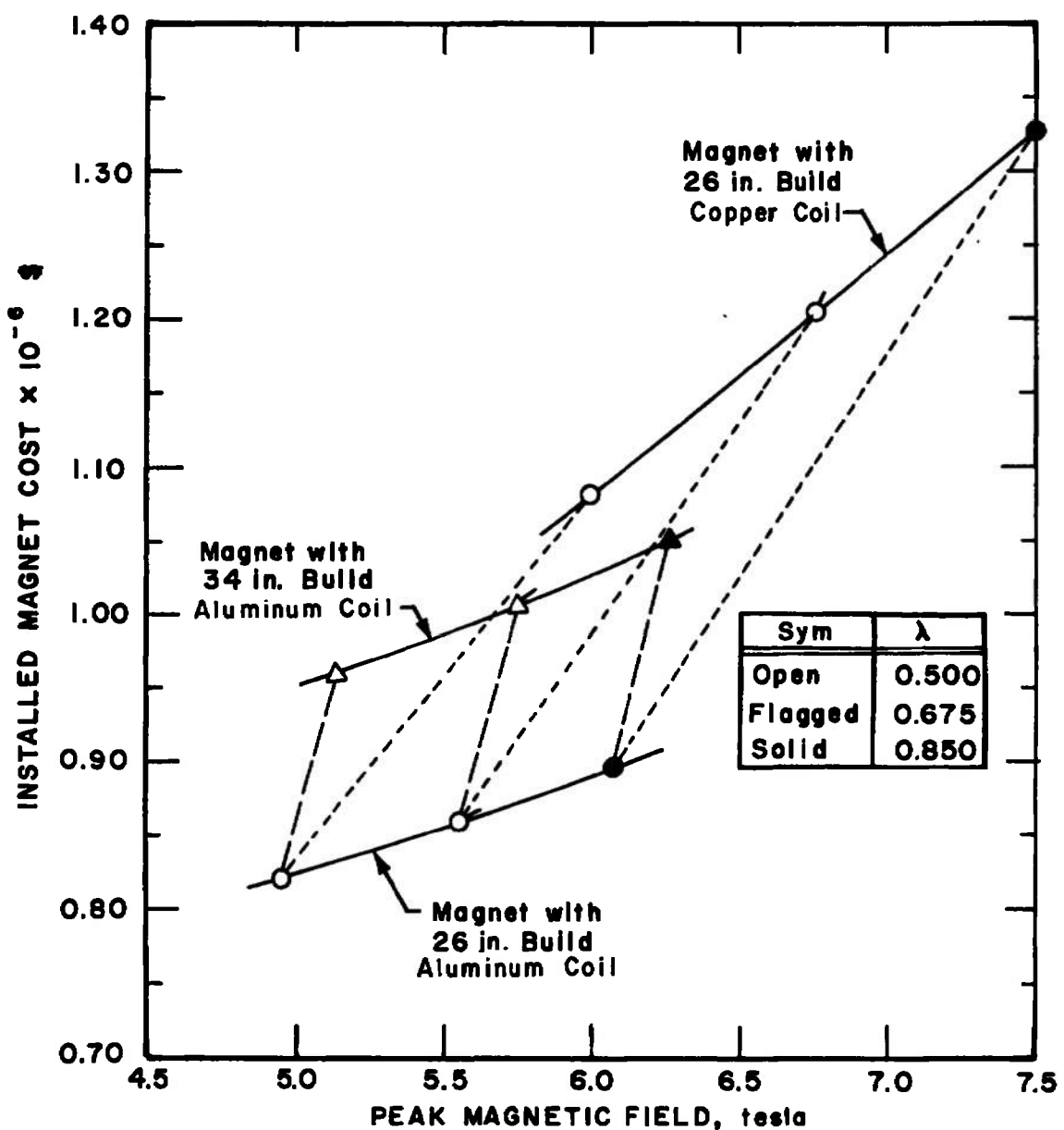
Fig. 45 Cost versus Magnetic Field for Different Sized Coils
and Different Space Factors and in Aluminum and Copper
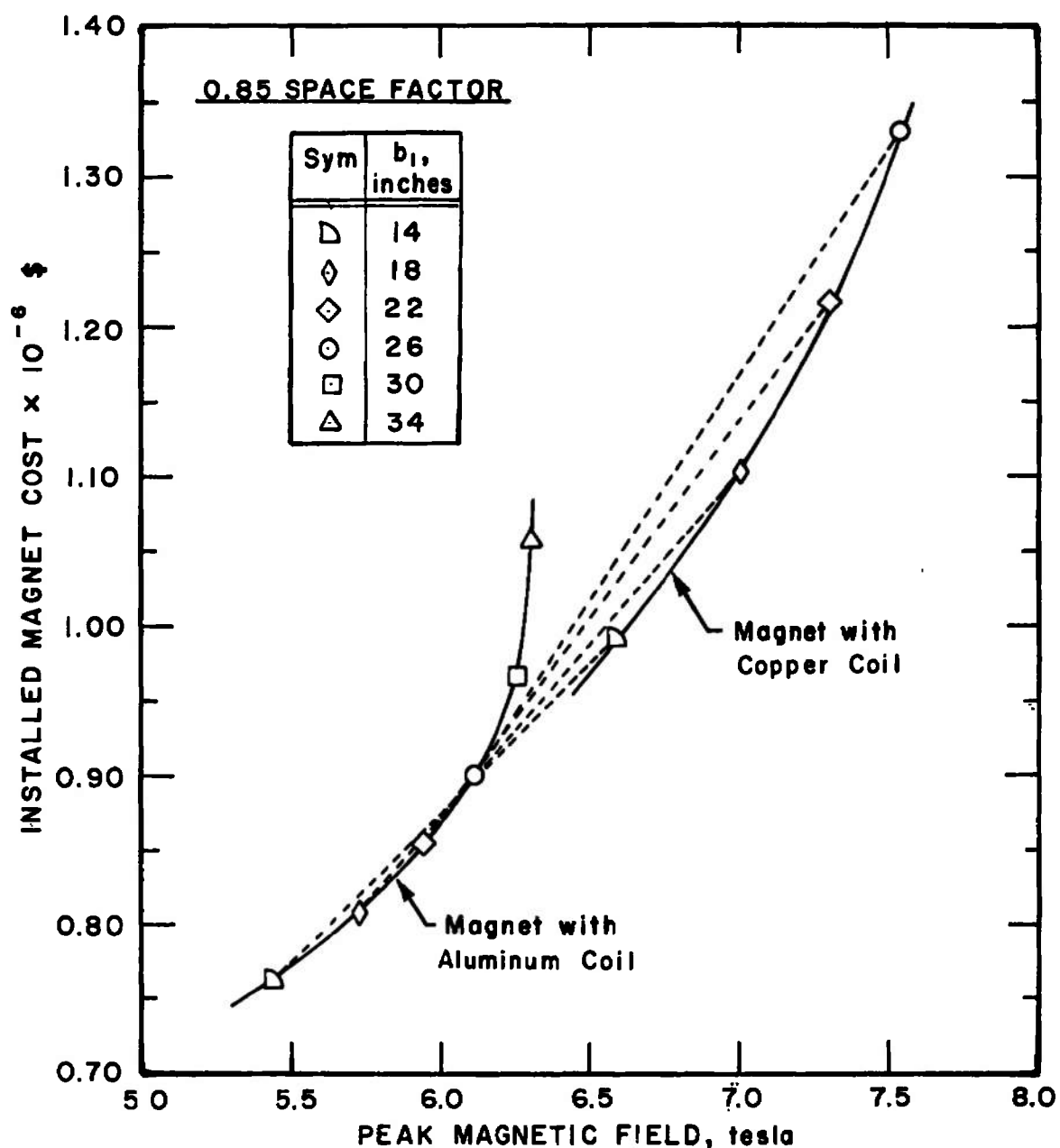
Fig. 46 Cost versus Magnetic Field for Different Sized Coils
in Aluminum and Copper at a 0.85 Space Factor

87
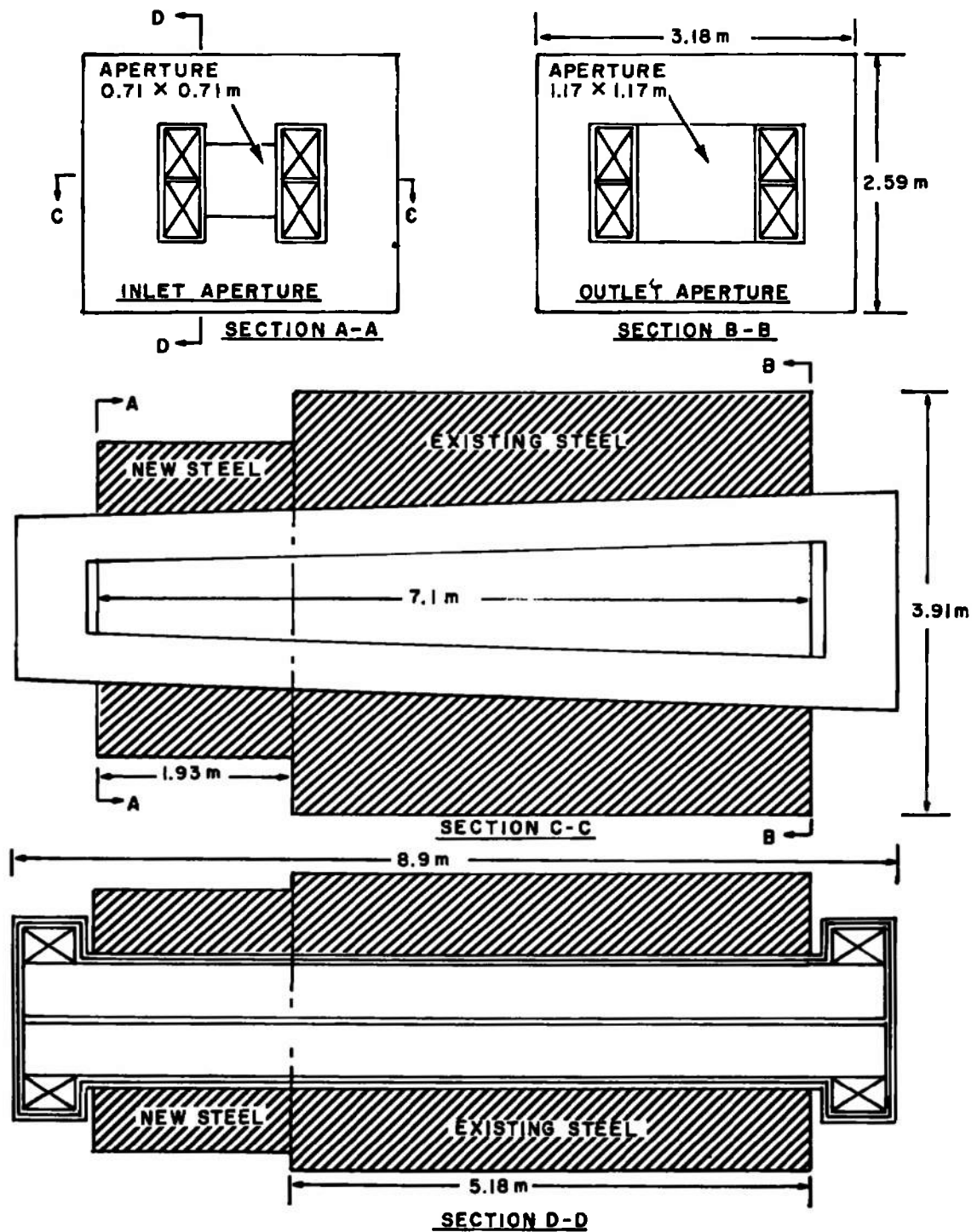
Fig. 47 Schematic of Magnet Coil and Steel

NITROGEN VENT

COIL SUPPORTS
INNER VACUUM WALL
COIL

OUTER VACUUM WALL

NITROGEN FILL
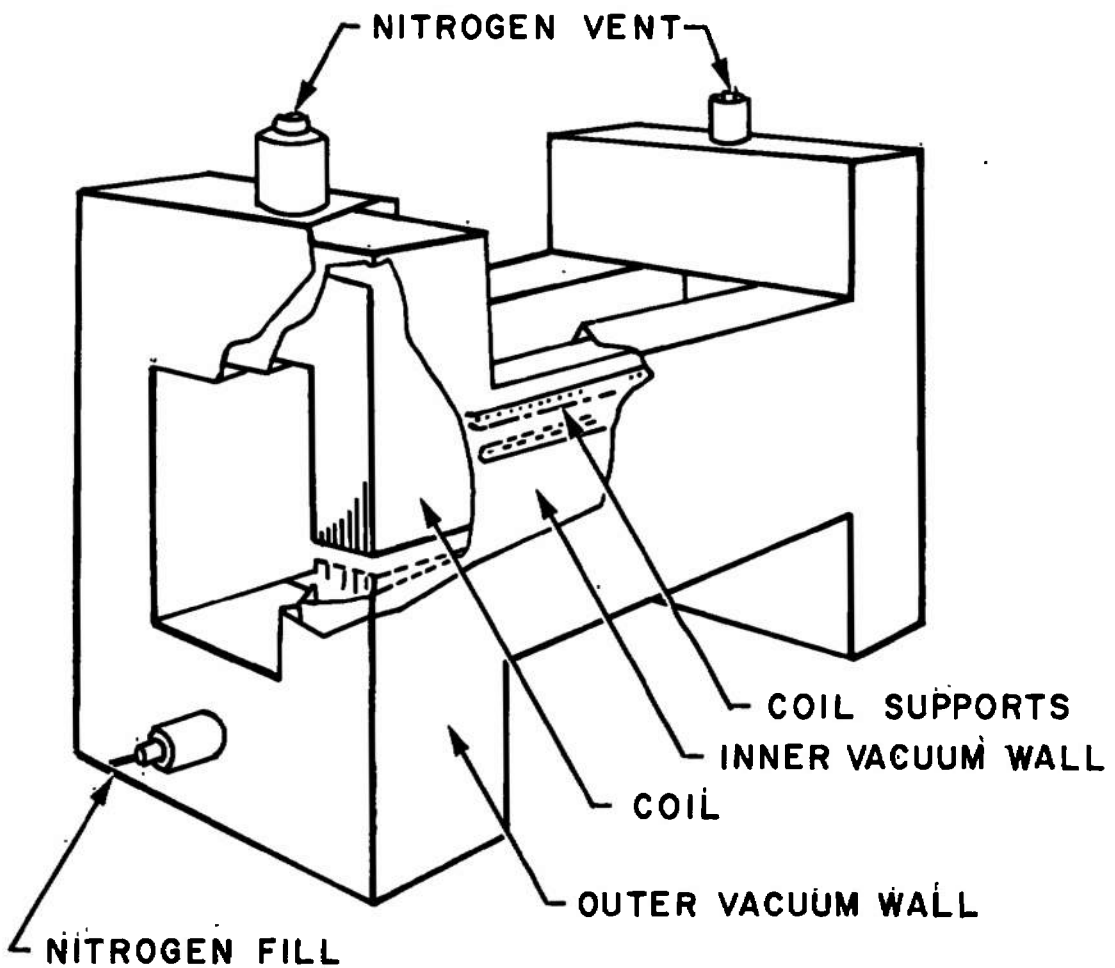
Fig. 48 Schematic of Double Wall Cryostat and Coil

N$_2$/O$_2$ (Burner) 3 Places

Fuel In (Burner)

H$_2$O In (Burner) 2 Places

H$_2$O Out (Backplate) 8 Places

H$_2$O Out (Pilot Throat)

Pressure Tap (Sparkplug)

H$_2$O Out (Sparkplug)

Fuel In (Sparkplug)

Igniter

O$_2$ In (Sparkplug)

H$_2$O In (Sparkplug)

Pilot Burner Chamber

N$_2$/O$_2$ In (Pilot Burner)

N$_2$/O$_2$ In (Backplate) 12 Places

Pressure Tap Bolt

H$_2$O In (Pilot Throat)

Pressure Tap (Burner)

H$_2$O In (Backplate) 10 Places

Fuel Tap Injector Assembly

H$_2$O Out (Burner) 2 Places

90

Fig. 49 Burner Backplate

LORHO BUILDING*

€ SPRAY BANKS*

DIFFUSER
SECTION

GENERATOR CHANNEL
NOZZLE
BURNER EXTENSION
BURNER ASSEMBLY*

8.9m
712m
1.17m

C C

BREACH*

EXHAUST
STACK*

4.6m
8.98m

SUPPORT PAD*
NEW MAGNET COILS

20MW RECTIFIER*

EXISTING STEEL

NEW STEEL

N

RAW WATER PUMP*

LOAD BANK*

0.71m

LAYOUT - PLAN VIEW

SECTION A-A
SHOWING TYPICAL
DIFFUSER CROSSECTION

0 35m
SQUARE

0 61m
Dia
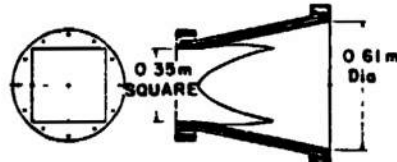
SECTION B-B
NOZZLE SECTION
1/8 SIZE
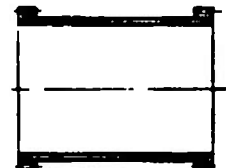
SECTION C-C
BURNER EXTENSION
1/8 SIZE

*REFERS TO EXISTING EQUIPMENT

Fig. 50 Layout of the High Efficiency Demonstration Equipment

TABLE I
LORHO PILOT FACILITY: VALUE OF EXISTING SUPPORT EQUIPMENT

Building	$ 642,000
Cooling Water System, 6,000 gpm continuous at 400 psi.	304,000
High Pressure Demineralized Water System 1,000 gpm at 3750 psi.	243,000
Fuel System (Toluene) 4,000 gal Storage and 200 hp Pump to provide 20 lbm/sec at 425 psi.	108,000
O_2/N_2 Storage System 4600 ft^3 at 2100 psi	270,000
O_2/N_2 Supply and Distribution System	202,000
Instrumentation and Control System	540,000
Transformers, Breakers, and Switchgear	275,000
Rectifiers	345,000
Cables	135,000
Substation Transformers and Switchgear	800,000
Generator Magnet	472,000
Diffuser and Exhaust Duct	88,000
Burner and Nozzle	162,000
EXISTING INVESTMENT	$4,586,000

TABLE II
COMPARISON OF "STANDARD" BASE–LOAD DESIGNS

	REFERENCE 2	REFERENCE 3	REFERENCE 4	REFERENCE 5
Mass Flow	582 kg/sec	650 kg/sec	732 kg/sec	750 kg/sec
Fuel	Coal (Moist)	Oil	Coal	Heavy Oil
Oxidizer	Air (1238°K)	Air (1400°K)	Air (1370°K)	Air (1770°K)
$(F/O)/(F/O)_{Stoichiometric}$	0.95	1.0	1.0	1.0
Configuration	Faraday	Faraday	Diagonal Wall	Faraday
Seed	0.5% Cs by wt (1%K)	1%K	1%K by wt	1% KOH by wt
Combustion Pressure (Outlet)	4.5 atm	4.0 atm	5.5 atm	7.2 atm
Combustion Temperature	2645°K	2669°K	2670°K	2887°K
Inlet Velocity	750 m/sec	800 m/sec	Subsonic	1031 m/sec
Exit Velocity	568 m/sec	800 m/sec	Not Stated	931 m/sec
Degree of Impulse	0.13	0	Not Stated	≈ 0.1
Inlet Temperature	2520°K	2533°K	Not Stated	2627°K
Inlet Pressure	3.1 atm	2.60 atm	Not Stated	3.7 atm
Field Strength	6 tesla	6 tesla	6 (to 3.6) tesla	5 tesla
Generator Length	17.5 m	16.0 m	18 m	16.6 m
Mean L/D	8.8	8.0	8.6	8.0
Exit Dimension	2.64 m	2.82 m	2.70 m	2.58 m
Inlet Dimension	1.33 m	1.61 m	1.30 m	1.22 m
Inlet Conductivity	4.2 mho/m	5.3 mho/m	Not Stated	9.1 mho/m
Outlet Conductivity	1.3	0.6 (2040°K)	Not Stated	1.9
Max Hall Parameter	5	5	4	5
Hall Voltage	64 kv	60 kv	50 kv	38 kv
Loading Coefficient	0.78	0.75	Not Stated	0.80
MHD Output	398 MW	461 MW	570 MW	700 MW
Turbine Efficiency	75%	68%	68%	65%
Energy Extraction	0.18	0.17	0.21	0.22
Plant Efficiency	50.4%	48.2%	48.9%	52.1%

TABLE III
COMPOSITE BASE-LOAD DESIGNS

	Composite Having 70% Turbine Efficiency	Composite Having 60% Turbine Efficiency
Mass Flow	650 kg/sec	650 kg/sec
Fuel	Coal (surface dried)	Coal (surface dried)
Oxidizer	Air (1370°-2000°F)	Air (1370°K)
F/O/(F/O) Stoichiometric	1.0	1.0
Configuration	Diagonal Wall	Diagonal Wall
Seed	1%K by wt	1%K by wt
Combustion Pressure(Outlet)	5.0 atm	6.7 atm
Combustion Temperature	2665°K	2680°K
Inlet Velocity	750-850 m/sec	750-850 m/sec
Degree of Impulse	0.00-0.15	0.00-0.15
Inlet Temperature	2550-2510°K	2565-2515°K
Inlet Pressure	3.4-3.0 atm	4.5-4.0 atm
Field Strength	6 (to 3.6) tesla	6 (to 3.6) tesla
Generator Length	18 m (est.)	21 m (est.)
Inlet Conductivity	4.5-4.0 mho/m	3.7-3.2 mho/m
Mean L/D	8.6	11
Exit Dimension	2.65 m	2.30 m
Inlet Dimension	1.33 m	1.15 m
Max Hall Parameter	4	4
Hall Voltage	50-55 kv	50-55 kv
Electric Field	3.0 kv/m	3.3 kv/m
Loading Coefficient	0.70	0.60
MHD Output	498 MW	498 MW
Turbine Efficiency	70%	60%
Energy Extraction	0.20	0.20

TABLE IV
EFFICIENCY DEMONSTRATION CHANNEL OPERATING CHARACTERISTICS

	Single Circuit Diagonal	Segmented Faraday
Net Power Output	51.3MW	58.5 MW
Conductivity, inlet/exit	9.0/6.4mho/m	11.0/6.7 mho/m
Max. Transverse Electric Field	3350 v/m	3600 v/m
Max. Axial Electric Field	2266 v/m	2617 v/m
Peak Current Density	1.6 amp/cm^3	1.6 amp/cm^3
Overall Turbine Efficiency	61%	69%
Energy Extraction Ratio	0.16	0.18
Magnetic Field, inlet/peak/exit	2.5/6.2/3.2 Tesla	
Flow Velocity, inlet/exit	740/870 m/sec	
Channel area, inlet/exit	.1315/.859m^3	
Channel length, for power extraction	7.0 m	
Hall parameter, inlet/exit	0.80/2.8	
Current	4675 amps	
Axial voltage	10,990 volts	
Mass Flow	60 kg/sec	
Combustion Pressure	6.75 atm.	

TABLE V
SIMPLIFIED MAGNETIC INDUCTION EXPRESSIONS

For

$$0 < NI < NI_1$$

Where

$$NI_1 = w_{inlet}\, B_s/\mu_o \quad \text{(Saturation at the inlet)}$$

Use

$$L_1/N^2 \cong \mu_o \ell_p \left(1 + \frac{b_2}{h_3}\right)$$

For

$$NI_1 < NI < NI_2$$

Where

$$NI_2 = w_{outlet}\, B_s/\mu_o \quad \text{(Saturation at the outlet)}$$

Use

$$L_2/N^2 \cong \mu_o \ell_p \left[\frac{1}{2} + \frac{1}{2}\frac{w_o}{\mu_o}c + \frac{b_2}{h_3}\right]$$

$$w_o = \frac{w_{inlet} + w_{outlet}}{2} \quad \text{(i.e. average pole width)}$$

and

$$c = \frac{\Delta B_{coil}}{NI} = \frac{\mu_o}{-b_1}\left[\frac{\tan^{-1}(h_c/y_2)}{h_c/y_2} - \frac{\tan^{-1}(h_c/y_1)}{h_c/y_1} + \ell n \sqrt{\frac{h_c^2 + y_2^2}{h_c^2 + y_1^2}}\right]$$

For

$$NI > NI_2$$

Use $\quad L_3/N^2 \cong cw_3\ell_p \quad$ and $\quad w_3 = w_o + b_2$

96

TABLE VI
COMPARISON OF BASE-LOAD AND DEMONSTRATION EXPERIMENT PERFORMANCE

	Base Load	Demonstration	
		Segmented Electrode	Single Circuit Diagonal
Magnetic Field	6T	6T	6T
MHD Output	500 MW	58.5 MW	51.3 MW
Turbine Eff.	70%	69%	61%
Specific Energy Extraction	0.77 MJ/kg	0.98 MJ/kg	0.86 MJ/kg
Energy Extraction Ratio	0.20	0.182	0.160
Mass Flow	650 kg/sec	60 kg/sec	
Fuel	Coal	Toluene (C_7H_8)	
Oxidizer	Air (2000°F)	(N_2/O_2) = 1.25	
Flow Energy/Mass	3.8 MJ/kg	5.4 MJ/kg	
Combustion Press.	5.0 atm	6.75 atm	
Mach Number	Subsonic	Subsonic	
Length	20 m	7 m	

APPENDIX II
CHANNEL DESIGN EQUATIONS AND COMPUTER CODES

The channel design (area distribution) is determined using the usual quasi-one-dimensional gas-dynamic equations including MHD effects for the inviscid core and a momentum integral formulation for the rough wall turbulent boundary layer. The design is determined by specifying the degree of impulse r as

$$r = \frac{\rho u \, du/dx}{\rho u \, du/dx + dp/dx} \qquad \text{(II-1)}$$

With the degree of impulse specified, the gas-dynamic equations can be written as

$$dp/dx = j_y \, B(1 - r) \qquad \text{(II-2)}$$

$$du/dx = \frac{1}{\rho u} \frac{r}{1 - r} \frac{dp}{dx} \qquad \text{(II-3)}$$

$$\frac{dh}{dx} = \frac{\vec{j} \cdot \vec{E}}{\rho u} - u \frac{du}{dx} \qquad \text{(II-4)}$$

The slant-wall design outlined in this report used a value of -0.075 for the degree of impulse.

The electrical parameters are determined from Ohm's law in the form

$$j_x = \frac{\sigma}{1 + \Omega^2} \{E_x - \Omega(E_y' + V_e/D_y - uB)\} \qquad \text{(II-5)}$$

$$j_y = \frac{\sigma}{1 + \Omega^2} \{\Omega E_x + E_y' + V_e/D_y - uB\} \qquad \text{(II-6)}$$

where $E_y' D_y$ is the emf available to an external circuit defined by

$$E_y' \, D_y = E_y D_y - V_e \qquad \text{(II-7)}$$

where E_y is the electric field produced in the core flow and V_e is the electrode voltage drop. The voltage drop, based on data taken in peg-wall channels (Refs. 7 and 8), is expressed as

$$V_e = a + xb j_y \qquad \text{(II-8)}$$

where a = 50 and b = -0.002.

The slant-wall generator calculations also use a constant current, 1, specified as

$$1 = A(j_x + \phi j_y)$$ (II-9)

where

$$\phi = E_y' / E_x$$ (II-10)

is the tangent of the slant-wall angle measured from the y-axis. When ϕ and I are specified the current and electric field can be written as (using Eqs. (II-5) through (II-10))

$$E_x = \frac{\frac{I}{A}\frac{1}{\sigma}\left[1 + \Omega^2 - x\frac{b\sigma}{D_y}\right] - \left[uB - \frac{a}{D_y}\right](\Omega - \phi)}{1 + \phi^2 - x\frac{b\sigma}{D_y}}$$ (II-11)

$$j_y = \frac{\frac{E_x\sigma}{1+\Omega^2}(\Omega - \phi) - \frac{\sigma(uB - a/D_y)}{1+\Omega^2}}{1 - \frac{xb\sigma/D_y}{1-\Omega^2}}$$ (II-12)

$$E_y' = \phi E_x$$ (II-13)

$$j_x = I/A - \phi j_y$$ (II-14)

When I is specified and with $j_x = 0$, the current and electric field for a slant-wall generator can be expressed as

$$E_y' = \frac{I}{A}\frac{\Omega}{\sigma}$$ (II-15)

$$F_x = \frac{\Omega\left[\frac{I}{A}\frac{\Omega}{\sigma} - uB + a/D_y\right]}{1 - \sigma xb/D_y}$$ (II-16)

$$j_y = \frac{\sigma E_x}{\Omega}$$ (II-17)

$$\phi = E_y'/E_x$$ (II-18)

$$E_y = E_y' + \frac{a}{D_y} + \frac{b}{D_y}xj_y$$ (II-19)

The real-gas thermodynamics are calculated using an existing AEDC program which gives the composition and properties of the products of combustion for any mixture consisting of the elements C, H, N, and O in any molecular combination. The electrical

conductivity is calculated using the STD algorithm described in Ref. 15. A momentum integral method (Ref. 16) is used to calculate the rough-wall turbulent boundary-layer characteristics in order to correct the channel area distribution.

APPENDIX III
TWO-DIMENSIONAL FLOW-FIELD CALCULATIONS*

The steady, compressible, inviscid, adiabatic flow of an ionized gas through a linear, segmented-electrode, MHD generator channel operated in a diagonal mode is computed in order to compare the differing results obtained by assuming one-dimensional flow vis-a-vis two-dimensional flow in the plane of the applied electric field. The calculations referred to in this Appendix as one-dimensional are actually performed as two-dimensional solutions in the plane of the applied magnetic field, but the profiles computed in the z-direction are so nearly uniform that for all practical purposes the results are equivalent to one-dimensional results. The purpose for using two-dimensional equations in the B-field plane is to permit the conclusion that the differing results alluded to above are not a consequence of the inclusion of streamline slope in the analysis.

The essentially one-dimensional analytic model requires the specification of the total current and effective slant angle distribution along the generator. The slant-wall mode of operation is simulated in the electric field plane by assigning current density boundary values which are related in an average sense to solutions for the axial current distribution obtained a priori in the one-dimensional solutions. Consequently, the analytical model used in the E-field plane is not, strictly speaking, a slant-wall channel but is an approximation in the following sense. The specification of a slant-wall channel operating in the two-terminal mode requires the specification of I and ϕ. Solution for the flow through such a channel results in a current density distribution along the channel boundaries. In this analysis a current distribution along the channel walls is specified so as to produce values of I and ϕ which approximate as closely as possible their design values. This approach in the E-field plane expedites the coding of the solution algorithm for the electric field and current density.

DESCRIBING EQUATIONS AND ASSUMPTIONS

The analytical model of the MHD flow field is obtained by introducing simplifying assumptions into the expressions for the conservation of mass, momentum, and energy of an ionized gas flowing through crossed electric and magnetic fields. Since the channel walls are diverged in both planes, a source flow is assumed in order to analyze such a three-dimensional configuration within the framework of two-dimensional equations. The definition of source flow as used in the present analysis is presented in Appendix II of Ref. 17 and results in the expression for conservation of mass

$$\nabla \cdot D\rho\vec{V} = 0$$

In each plane the numerical integration of the gas-dynamic equations is performed using a streamtube method. The numerical solutions of the electrical relationships are performed in disparate manners with the exception that the same form of Ohm's law (where tensor conductivity is assumed) is used in both planes. The specification of the

---

*This analysis was performed by Mr. P. W. Johnson, PWT, ARO, Inc.

constraints I and ϕ (x) is sufficient to close the set of equations in the one-dimensional calculations. When the calculations are performed in the E-field plane, it is required that the partial differential equations for conservation of current and Faraday's law be satisfied. The fact that the insulator walls are nonparallel required that continuity of current include the assumption of source flow, i.e.,

$$\nabla \cdot D\vec{j} = 0$$

RESULTS

Comparisons of results of one- and two-dimensional solutions are presented in Figs. III-1 and III-4. Axial Mach number distributions as a function of the parametric variation of the total current are shown in Fig. III-1. Whereas a one-dimensional analysis would be adequate to demonstrate that Mach number is a sensitive function of I, perhaps the most significant conclusion of the entire study described in this Appendix is that a generator designed to achieve choked flow at the exit based upon one-dimensional calculations is predicted by two-dimensional, E-plane, solutions to choke at a location significantly far upstream of the exit. Figure III-2 shows the pressure and (inviscid) velocity profiles at the generator entrance and exit for a case of accelerated flow (based upon calculations in the E-field plane). Figure III-3 presents a comparison of current density and electric field solutions obtained from the one- and two-dimensional analyses. The similar results imply that the E-plane of the diagonal mode is a meaningful approximation. Finally, the distribution of axial voltage and power generated are shown in Fig. III-4, and it is found that at the exit the differences are about four percent.
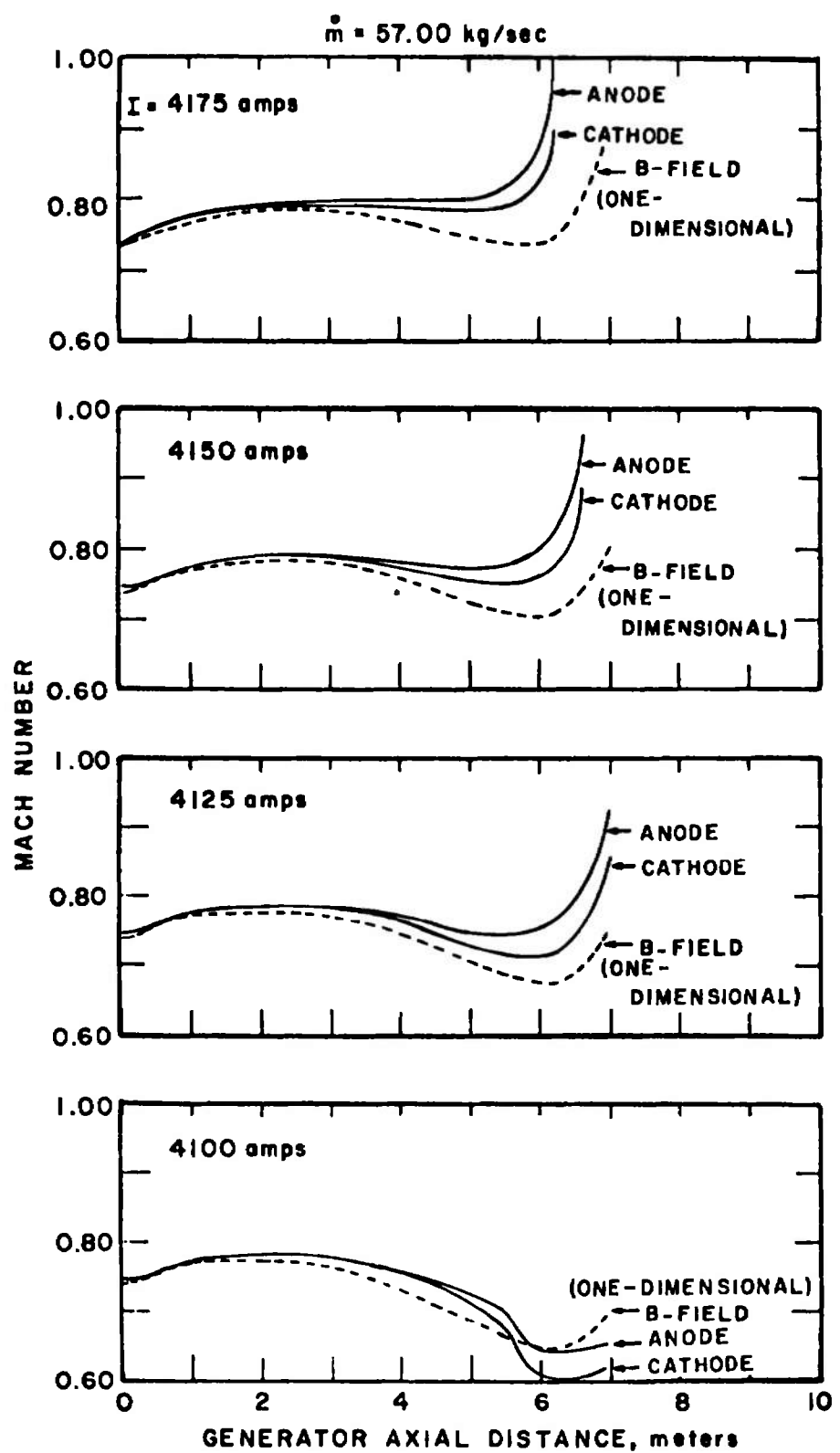
Fig. III-1 Mach Number versus Total Current; One and Two Dimensional
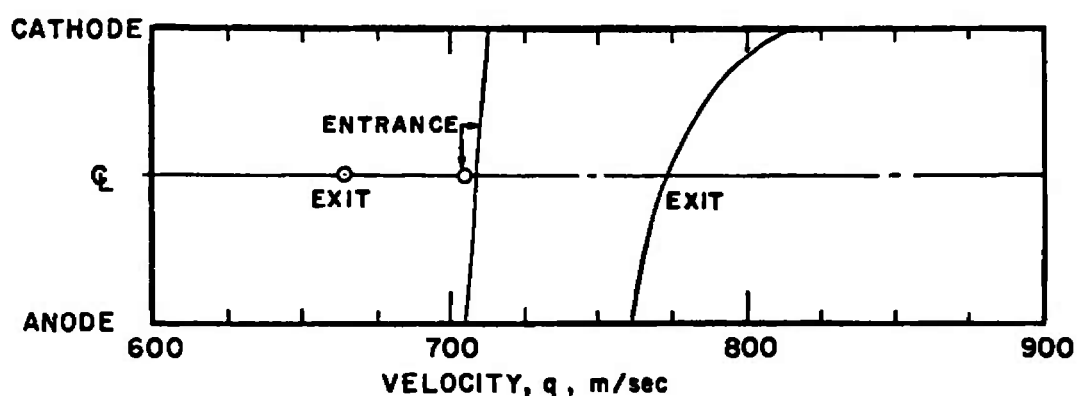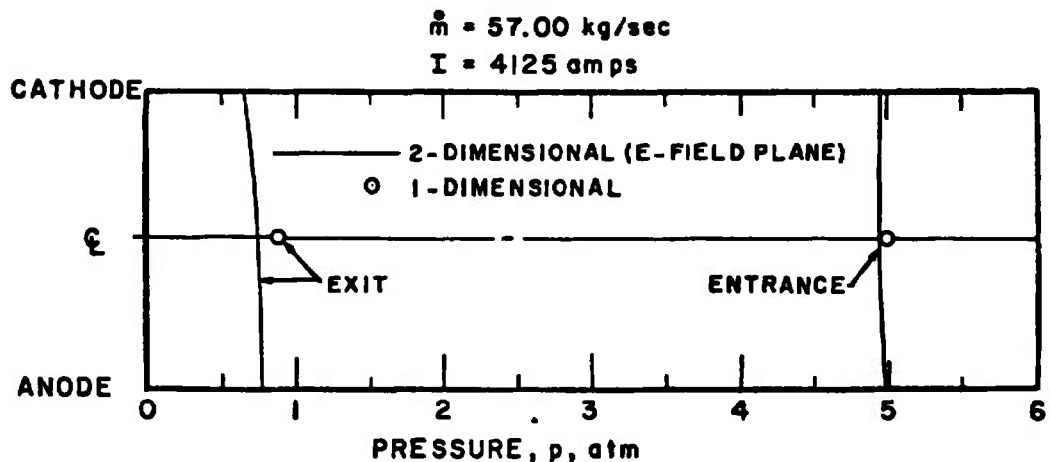
Fig. III-2 Pressure and Velocity; One and Two Dimensional
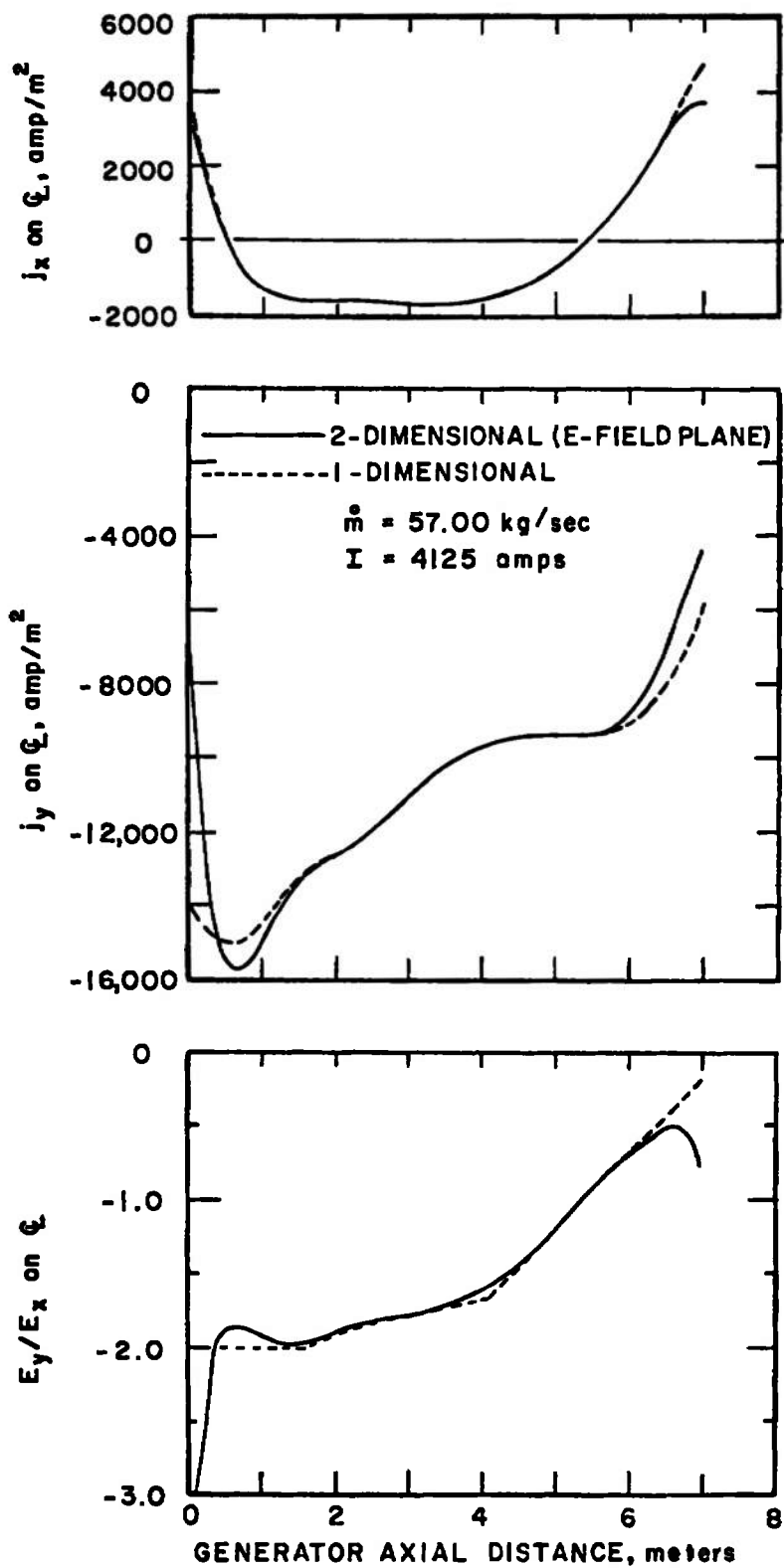
Fig. III-3 Current Density and Electric Field; One
and Two Dimensional
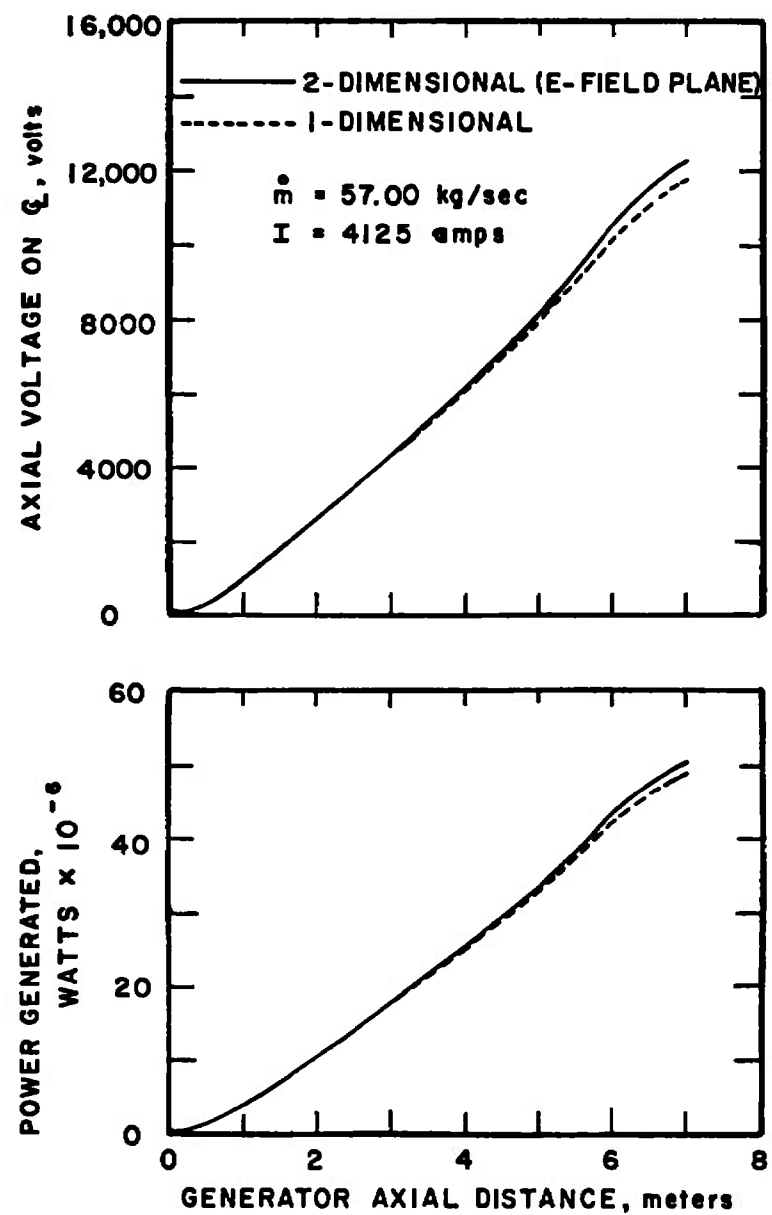
Fig. III-4 Axial Voltage and Power Generated;
One and Two Dimensional

DOCUMENT CONTROL DATA · R & D

(Security classification of title, body of abstract and indexing annotation must be entered when the overall report is classified)

1 ORIGINATING ACTIVITY (Corporate author)	2a. REPORT SECURITY CLASSIFICATION
Arnold Engineering Development Center Arnold Air Force Station, Tennessee 37389	UNCLASSIFIED
	2b GROUP N/A

3 REPORT TITLE

DEVELOPMENT OF DESIGN CRITERIA, COST ESTIMATES, AND SCHEDULES FOR AN MHD HIGH PERFORMANCE DEMONSTRATION EXPERIMENT

4 DESCRIPTIVE NOTES (Type of report and inclusive dates)
Final Report – April 1972 to April 1973

5 AUTHOR(S) (First name, middle initial, last name)

G. W. Garrison, ARO, Inc.; T. R. Brogan and H. J. Schmidt, MEPPSCO, Inc.; and J. J. Nolan, MEA, Inc.

5 REPORT DATE	7a. TOTAL NO OF PAGES	7b. NO OF REFS
August 1973	116	17

8a CONTRACT OR GRANT NO	9a. ORIGINATOR'S REPORT NUMBER(S)
b. PROJECT NO	
	AEDC-TR-73-115
c. Program Element 65802F	9b. OTHER REPORT NO(S) (Any other numbers that may be assigned this report)
d	ARO-PWT-TR-73-75

10 DISTRIBUTION STATEMENT

Approved for public release; distribution unlimited.

11 SUPPLEMENTARY NOTES	12 SPONSORING MILITARY ACTIVITY
Available in DDC	Office of Coal Research Department of Interior Washington, D.C.

13 ABSTRACT The successful application of magnetohydrodynamics (MHD) for commercial, coal-fired, base-load power generation requires that the generator have an energy extraction ratio of approximately 0.20 with a turbine efficiency of 70 percent. There is a significant gap between this required performance and the generator performance which has been achieved to date. The commercial MHD concept is critically dependent upon the generator achieving this required performance, and it is therefore essential that a demonstration of this generator performance have the highest priority. Of equal importance, the generator channel configuration and operating conditions which are necessary in order to achieve the required performance will be determined while accomplishing the performance demonstration. Thus other Office of Coal Research (OCR) sponsored MHD research efforts can be directed toward the real problems and configurations as determined by solid experiments. Several possible options for carrying out an experiment meeting the objectives of the performance demonstration recommended by OCR Report No. 71 were considered. It is concluded that a definitive and favorable demonstration is feasible using the existing LORHO MHD facility at AEDC with a modified magnet and a new high performance generator channel. The experiment will not only demonstrate performance but also will be of a size which will allow scaling of the experimental results to the full-scale generator with reasonable confidence.

DD FORM 1473
1 NOV 65

14. KEY WORDS	LINK A		LINK B		LINK C	
	ROLE	WT	ROLE	WT	ROLE	WT
magnetohydrodynamics						
magnetohydrodynamic generators						
electric power generation						
test equipment						
test facilities						
cost estimates						
Hall effect						
scale effect						

AFSC
Arnold AFS Tenn